Spring 2014

State Variable Model for Unsteady Two Dimensional Axial Vortex Flow with Pressure Relaxation

Mazin Mohammed Elbakri Abuharaz
Old Dominion University

STATE VARIABLE MODEL FOR UNSTEADY TWO DIMENSIONAL AXIAL VORTEX FLOW WITH PRESSURE RELAXATION

by

Mazin Mohammed Elbakri Abuharaz
B.S. May 2001, University of Khartoum, Sudan
M.S. January 2009, University of Khartoum, Sudan

A Dissertation Submitted to the Faculty of
Engineering and Technology Old Dominion University in Partial Fulfillment of the Requirements for the Degree of

DOCTOR OF PHILOSOPHY

AEROSPACE ENGINEERING

OLD DOMINION UNIVERSITY
February 2014

Approved by:

Robert L. Ash (Director)

Miltiadis Kotinis (Member)

Li-Shi Luo (Member)

Shizhi Qian (Member)

ABSTRACT

STATE VARIABLE MODEL FOR UNSTEADY TWO DIMENSIONAL AXIAL VORTEX FLOW WITH PRESSURE RELAXATION

Mazin Mohammed Elbakri Abuharaz
Old Dominion University, 2014
Director: Robert L. Ash

This research has utilized a state variable model for unsteady two dimensional axial vortex flows experiencing non-equilibrium pressure gradient forces. The model was developed successfully using perturbed radial and azimuthal momentum equations and a pressure Poisson's equations. Three main regions of the axial vortex flow were highlighted in this study including: a laminar core region, a non-equilibrium pressure envelope, and an outer potential vortex.

Linear stability theory was utilized to formulate the model and the perturbation functions were assumed to be of the Fourier type. The flow parameters considered were the Reynolds numbers, ranging between 6,000 and 14,000, and a new non-equilibrium swirl parameter, *Np* determining the area of significant non-equilibrium pressure forces. Two other state variable parameters were imposed-complex frequency and associated azimuthal mode number. Perturbation outputs included primary Reynolds stress, radial and azimuthal velocity amplitudes, and radial pressure gradient amplitudes.

Maximum perturbation growth occurred inside the non-equilibrium pressure zone between one and five core radii from the rotational axis, while the inner core remained laminar. The maximum amplitudes and critical radii depended on the four physical and state variable parameters. Increases in *Np* resulted in lower perturbation pressure gradient amplitudes, moving the critical radius closer to the vortex core, and expanding

the non-equilibrium pressure zone. Increasing the frequency resulted in steady increases in the perturbation amplitudes until a particular dimensionless frequency was reached. Beyond that frequency, additional perturbation growth was insignificant or the amplitude decayed because of a high damping factor. Two types of azimuthal modes were unstable, the $\pm$ ½ modes inside the non-equilibrium pressure zone, causing the pressure gradient amplitudes to peak even though the azimuthal velocity profile remained stable, and $\pm$ 1 helical modes associated with growing pressure gradient amplitudes in the outer potential region. The symmetrical azimuthal modes were globally stable.

The state variable model was stable numerically inside the non-equilibrium pressure zone, even though the perturbation amplitudes exhibited instability. Inside that region, unstable pressure eigenmodes were detected in the form of relaxation Reynolds stresses in response to perturbations in the flow. The width of the non-equilibrium pressure zone was again determined using eigenmode plots for different *Np*. The positive real parts of the unstable modes were slightly larger in the outer potential region causing slow growth profiles.

The current vortex state variable model can be utilized to explore the development of small perturbations in the non-equilibrium zone as the flow becomes turbulent, via a bifurcation cycle study where coherent structures can be identified. Experimental verification using hot-wire probes is needed to validate the theory and adjust the state variable model parameters. A side effect of the non-equilibrium pressure model for this vortical flow is the likely sound propagation causing small density perturbations that are balanced by the contracted pressure gradient-velocity tensor terms in the pressure relaxation equations. This non-equilibrium balance process appears to vanish in the outer potential vortex region.

All praises are due to Allah the creator of the universe for his guidance and blessings to complete this journey, all the successful attempts were from his grace and the mistakes were from me. Prayers and peace be upon the Prophets Muhammad, Jesus, Moses, Abraham and all the messengers between them who guided the human beings to the oneness of Allah.

This research is dedicated to my teacher in life Sayed Baba Hasan peacefully in his shrine, to my parents Leila (my mother) and Muhammad (my father) who sacrificed a lot so that I reached this level of education, and continued their encouragement and prayers.

The dedication is also to my beloved wife Arwa and our two children Baba Hasan and Fatima Alzahraa for being such a wonderful family and really made this period of four years enjoyable regardless of the hardships and stressful work involved in the PhD research. Thank you to my friend Ahmed Mekky and his wife who were always close to our family.

Old Dominion University has been an amazing experience with the student activities, administration support, excellent services and setup of high technology assets and recreational rooms.

May Allah bring success to all students seeking the knowledge and making our world a better place, and all the success comes from Allah the Almighty and the Sustainer of this life. Amen

Mazin Abuharaz

Norfolk, Virginia, USA

ACKNOWLEDGMENTS

I would like to express thanks for Prof Ash for the ultimate help throughout these four years, since I first approached him after finishing the Turbulence class and he accepted to advise my PhD research that was in the spring semester of 2010.

My thanks to PhD committee Dr. Li-Shi Lu, Dr. Miltiadis Kotinis, and Dr Shizi Qian, for their help and advice with different stages of qualification in the study. I appreciate support from the Mechanical and Aerospace Department administration, with special thanks to Mrs. Miriam, Sheila, Diane, and Jayne for making the work environment feel like home by their kind attention to our concerns with technical and administrative issues through all these years.

Thank you my friends in the society of graduate students at the Mechanical and Aerospace Engineering, Modeling and Simulation, and Computer Sciences departments.

NOMENCLATURE

P	pressure	Pa
r,θ, z	cylindrical coordinates	m
r_c	Core radius	M
Re	Reynolds number	1
R_h	Relative humidity	%
v_r'	Radial perturbation velocity component	m/s
v_θ'	Azimuthal perturbation velocity component	m/s
v_z'	Axial perturbation velocity component	m/s
V_θ	Mean azimuthal velocity	m/s

Greek Symbols

ω	Frequency	rad/s
η_P	Pressure relaxation coefficient	s
ρ	Density	Kg/m^3
ν	Kinematic viscosity	m^2/s
μ	Dynamic viscosity	Pa.s
$\tau_{r\theta}$	Primary Reynolds stress	Pa
Γ	Circulation	m^2/s

TABLE OF CONTENTS

Page

Page

LIST OF TABLES

LIST OF FIGURES

Figure Page

Figure Page

CHAPTER 1

INTRODUCTION

Vortex flow stability has been the topic of research for many decades due to its importance in aeronautics, combustion and in turbulence modeling. Axial, trailing-line vortices extending from airplanes are a major factor considered in the safety of air traffic and swirl flows inside combustion chambers which requires additional study in order to enhance the performance of internal combustion engine.

Axial vortices present unusual modeling challenges because they incorporate typically: (1) a laminar flow region encompassing the rotational axis, (2) an unsteady, fluctuating region near the radius of maximum azimuthal velocity that is considered here to be a non-equilibrium pressure inner region and (3) an outer, potential-vortex region. The outer radius of the laminar region involves significant viscous shear forces, with an almost rigid central rotational zone. Moving outwards from the vortex centerline, the mean flow structure transitions smoothly from a radially-increasing velocity to a radially-decreasing potential flow vortex profile outside the core region. Because of large pressure gradients in the core region, non-equilibrium pressure forces must be considered. These forces enveloping the core region enable the smooth change from rigid rotation to an outer potential vortex flow. Therefore, without the inclusion of non-equilibrium pressure, the conventional form of the Navier-Stokes equations is incapable of modeling this type of axial vortex velocity profile continuously.

1.1 Definition of equilibrium and non-equilibrium pressures of fluid

In incompressible flows, the mechanical pressure of the fluid is applied to keep the conservation of mass flow, in that sense the pressure is said to be an *equilibrium pressure.* Ash, Zardadkhan, and Zuckerwar (2006) showed that fluid can deviate from the state of equilibrium through relaxation processes. The *non-equilibrium pressure* is the mechanism that helps the fluid return to equilibrium. The stress exerted in the flow because of non-equilibrium pressure is dependent on the material derivative of the pressure gradient. When this quantity is diminished the flow is said to return to equilibrium.

1.2 Steady axial vortex flow

Modeling axial vortex flows has progressed through many stages, from the very simple potential vortex of Rankine (1882) to multi-parameter models by Vatistas (1991) and Wood and White (2011). Exact solutions have been developed by Burgers (1948) and Rott (1958) and recently Ash, Zardadkhan, and Zuckerwar (2011) incorporated non-equilibrium pressure gradient forces in a modified version of the Navier-Stokes equations.

The Rankine (1882) vortex model, neglected viscous effects altogether and spliced a potential vortex velocity profile for the outer region with a rigidly rotating central core region. The resulting velocity profile was continuous but the radial velocity gradient was not, resulting in an erroneous shear stress, where the azimuthal velocity was a maximum.

More than 50 years later, Burgers (1948) and Rott (1958) developed a one-parameter model that was an exact, three-dimensional solution for an axial vortex, given by:

$$V_{\theta,BR}(r) = \frac{1 - e^{-Kr^2}}{r} \tag{1.1}$$

where (K) is a constant. The circulation distribution represented by that velocity profile is not consistent with experimentally-measured circulation variations (Saffman and Govindaraju, 1971).

Vatistas (1991) developed another one-parameter model that fit experimentally-measured velocity profiles. The dimensionless general form was:

$$V_{\theta,Vat}(r) = \frac{r}{\left(1 + r^{2q}\right)^{1/q}}, \tag{1.2}$$

where q could be used to vary the shape of the profile. That equation can model a Rankine vortex when $q \to \infty$ and approximates a Burgers-Rott vortex by employing $q = 2$.

Wood and White (2010) suggested that a more useful empirical dimensionless vortex model was:

$$V_{\theta,WW}(r) = \frac{r^{\alpha}}{\left[1 + \alpha \cdot m^{-1}\left(r^{m/\lambda} - 1\right)\right]^{\lambda}}, \tag{1.3}$$

where α, m and λ were three adjustable coefficients with constraints $0 < k < n, \lambda > 0$. Their model was also capable of reproducing the previous vortex velocity profiles. Focusing on large-scale geophysical applications like tornadoes and water spouts, they showed that their model could be adjusted to more-accurately approximate experimental observations than could the previous one-parameter models.

Ash, Zardadkhan and Zuckerwar (2011) utilized a non-equilibrium pressure Navier-Stokes model for an axial vortex, to develop an exact, steady state solution for the tangential velocity and pressure deficit, represented in normalized form as

$$V_{\theta,AZ}(r) = \frac{2r}{1 + r^2} \tag{1.4}$$

The new solution illuminated all three regions of the vortex and could be validated experimentally for tornadoes and dust devil velocity profiles.

The normalized tangential velocity profiles using the different models outlined in this section are displayed in Figure 1.1. In the Rankine (1882) model, as mentioned previously, the radial azimuthal velocity gradient is not continuous at the core radius, but it is considered a useful approximation. The Burger-Rott model (denoted Burgers in Figure 1.1) was based on the assumption of isotropic turbulence, employing velocity correlation and turbulence scaling parameters to produce an exact three-dimensional solution. However, the model fails to represent the axial vortex flow outside the core region. The Vatistas (1991) model (denoted Vat in Figure 1.1) has a maximum core velocity that is less than the other models. Recently, The Wood-White (2010) model (denoted by WW in Figure 1.1) was developed to correlate large-scale vortex flows using three parameters which makes the numerical estimation of the model parameters a complicated process.

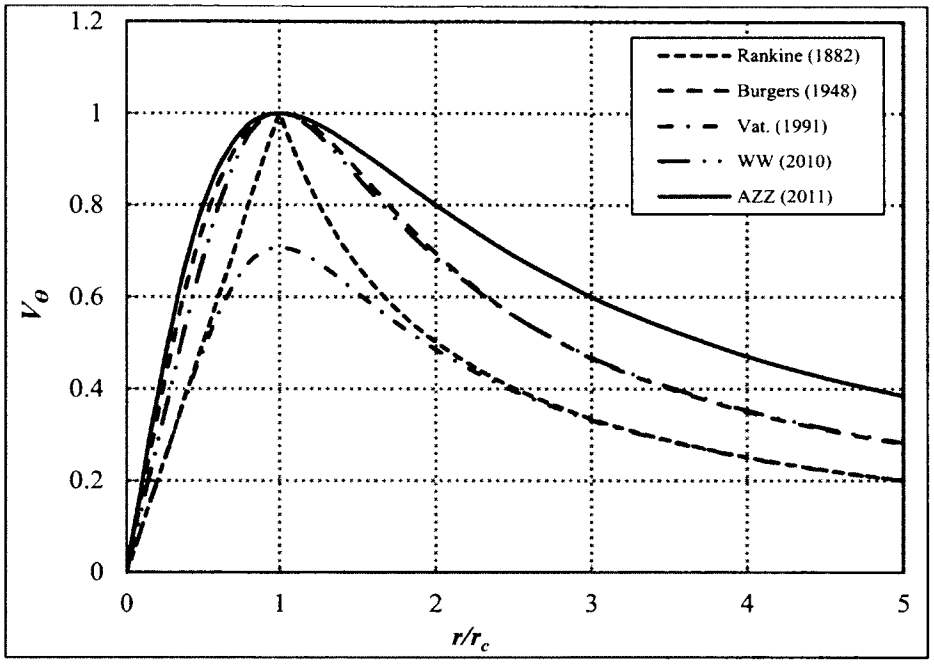

Figure 1.1 Normalized axial vortex profiles for different models

Finally, the Ash, Zardadkhan and Zuckerwar (2011) velocity profile is an exact solution to a one component azimuthal velocity axial vortex when pressure relaxation forces are incorporated. Inside the core, the three models (AZZ, WW and BR) are quite similar with the observation that the AZZ model envelops the other two models. In the outer region the AZZ profile is also above the other two models and it approaches the potential boundary conditions (zero velocity) at a somewhat slower rate than either the WW or the BR models.

1.3 Non-equilibrium pressure relaxation

Pressure relaxation was introduced in the Navier-Stokes equations to account for the non-equilibrium pressure effects; Zuckerwar and Ash (2006, 2009) derived the governing equations for simple incompressible fluids with pressure relaxation. Starting

from Hamilton's Principle outlined by Serrin (1959) and Witham (1968); a variational approach was developed to incorporate non-equilibrium thermodynamic effects in the equations of motion for a simple fluid.

The variational approach for deriving the non-equilibrium pressure equation first defines the variation in the total energy of the fluid filament as the change in the mechanical energy (kinematic and potential) and the change in the internal energy as functions of three independent variables of temperature, pressure, and a non-equilibrium progress variable. A non-equilibrium fluid state is thus incorporated by assuming the conservation of equilibrium and non-equilibrium species based on molecular degrees of freedom, along with the conservation of mass and entropy minimization. Then the Hamiltonian principle of least action is applied by utilizing Lagrange multipliers for each of the conservation constraints, i.e. mass, entropy, and chemical reaction (Zardadkhan, 2012).

The variation of total energy with respect to the independent variables of space, time, density, velocity, entropy, and progress variables, was formed and then a volumetric integration of the resulting variational functions followed.

The variational approach resulted in two extra terms that could be incorporated in the conservation of momentum equations, one of which is the relaxation stress in terms of the gradient of the material derivative of the thermodynamic pressure, scaled with a relaxation time constant called the pressure relaxation coefficient η_P characterizing the time dimension of the relaxation process. The other term is the dilatational stresses of the fluid resulting from small density fluctuations; the term is expressed in terms of the deviation of the second viscosity coefficient from the Stokes hypothesis, assuming that the second

coefficient of viscosity was equal to $-\frac{2}{3}\mu$. This deviation is the volume viscosity coefficient, η_v. Both of these non-equilibrium stresses could be added to the original average normal stresses of the flow, hence the vector form of the conservation of linear momentum is,

$$\rho\frac{Dv}{Dt} = -\nabla P - \left[\left(\eta_v - \frac{1}{3}\mu\right)\nabla\nabla\cdot v - \eta_P\nabla\frac{DP}{Dt}\right] - \mu\nabla^2 v \tag{1.5}$$

Acoustically-based values of the pressure relaxation coefficient η_P (in seconds)in air at different humidity levels are plotted in Figure 1.2.

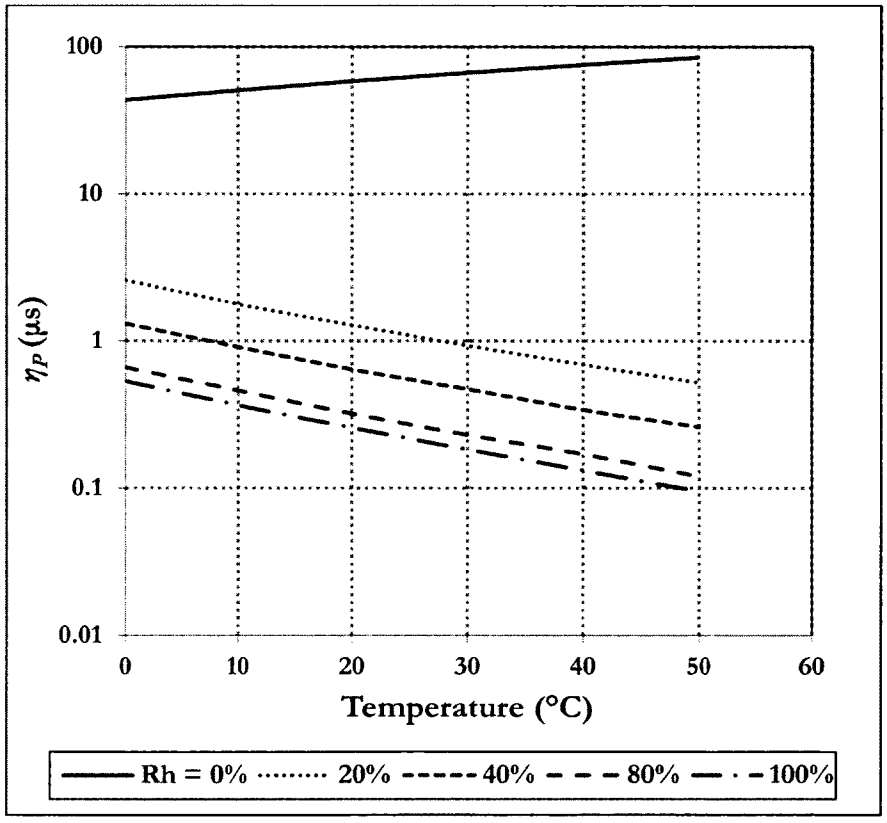

Figure 1.2 Influence of temperature and relative humidity on predicted non-equilibrium pressure coefficients in air (Ash and Zuckerwar, 2006)

Figure 1.2 shows that η_P varies significantly with the humidity level in air. On the basis of these large variations, it is logical to assert that the non-equilibrium behavior of the core regions of trailing line axial vortices, generated by aircraft in terminal flight will vary significantly depending on local weather conditions. This study should therefore be an important contribution to safe commercial aircraft operations.

The newly-identified quasi-reversible *relaxation process* can be considered as a mechanism to store mechanical energy while responding to non-equilibrium pressure in otherwise incompressible fluids. As the material rates of change of the thermodynamic variables become small, the non-equilibrium fluid mechanical processes can revert to equilibrium processes which return the fluid to an equilibrium state. Chemical affinity is the non-equilibrium driving force, drawing the fluid molecules back toward equilibrium. Between the excitation of fluid particles by non-equilibrium pressure for constant-density fluids and the response to those disturbances, the non-equilibrium pressure gradient forces can balance the viscous shear forces responsible for the dissipation part of overall fluid behavior. Thus the relaxation normal stresses can be an essential element in the Navier-Stokes equations required to balance the viscous forces acting on the fluid particles.

The Zuckerwar and Ash (2006) theory has been simplified for unsteady, constant-property, Newtonian fluid flows by first recognizing that non-equilibrium acoustic fluctuations can only be accommodated through the variable density form of the conservation of mass equation:

$$\frac{D\rho}{Dt} + \rho\bar{\nabla}\cdot\mathbf{v}=0 \tag{1.6}$$

In the absence of significant local temperature variations, the transport properties for a fluid can be treated as constants. The incompressible form of the conservation of

linear momentum Equation (1.5) is desired in the context that otherwise incompressible fluid flows are accompanied by near-negligible acoustic density and associated non-equilibrium acoustic pressure fluctuations if sound is being produced. Utilizing index notation, along with conservation of mass as in Equation (1.6), Equation (1.5) can be written:

$$\rho\frac{Dv_i}{Dt} = -\frac{\partial P}{\partial x_i} - \eta_p \frac{D}{Dt}\left(\frac{\partial P}{\partial x_i}\right) - \eta_p\left[\frac{\partial v_k}{\partial x_i}\frac{\partial P}{\partial x_k} - \frac{\eta_V - \frac{1}{3}\mu}{\eta_P}\frac{\partial}{\partial x_i}\left(\frac{1}{\rho}\frac{D\rho}{Dt}\right)\right] + \mu\frac{\partial^2 v_i}{\partial x_k^2}\ , \quad (1.7)$$

with two terms isolated in square brackets; the first term within the bracket is the contraction of the velocity gradient tensor with the pressure gradient, resulting from writing the pressure relaxation term as the material derivative of the pressure gradient instead of the gradient of the material derivative of pressure. The second term derives from small dilatational disturbances in fluid density due to the non-equilibrium pressure. Assuming that these two terms cancel each other, or become negligibly small, leaves the following form for the modified conservation of momentum equation for incompressible flows incorporating non-equilibrium pressure gradient forces:

$$\rho\frac{D\mathbf{v}}{Dt} = -\vec{\nabla}P - \eta_P \frac{D}{Dt}\vec{\nabla}P + \mu\nabla^2\mathbf{v} \quad (1.8)$$

The resulting N-S equations in three-dimensional (cylindrical) curvilinear coordinates are developed in Appendix A. The resulting cylindrical coordinate expressions for the three components of the conservation of momentum equation and continuity are:

Conservation of radial momentum equation (A.30):

$$\rho\left(\frac{\partial v_r}{\partial t}+v_r\frac{\partial v_r}{\partial r}+\frac{v_\theta}{r}\frac{\partial v_r}{\partial \theta}-\frac{v_\theta^2}{r}+v_z\frac{\partial v_r}{\partial z}\right)=\mu\left\{\frac{\partial}{\partial r}\left[\frac{1}{r}\frac{\partial}{\partial r}\left(rv_r\right)\right]+\frac{1}{r^2}\frac{\partial^2 v_r}{\partial \theta^2}-\frac{\partial^2 v_r}{\partial z^2}-\frac{2}{r^2}\frac{\partial v_\theta}{\partial \theta}\right\}-$$

$$-\eta_P\left[v_r\frac{\partial^2 P}{\partial r^2}+\frac{v_\theta}{r}\frac{\partial^2 P}{\partial \theta \partial r}+v_z\frac{\partial^2 P}{\partial z\partial r}-\frac{v_\theta}{r^2}\left(\frac{\partial P}{\partial \theta}\right)\right]-\frac{\partial P}{\partial r}$$

Conservation of azimuthal momentum equation (A.31):

$$\rho\left(\frac{\partial v_\theta}{\partial t}+v_r\frac{\partial v_\theta}{\partial r}+\frac{v_\theta}{r}\frac{\partial v_\theta}{\partial \theta}+\frac{v_r v_\theta}{r}+v_z\frac{\partial v_\theta}{\partial z}\right)=\mu\left\{\frac{\partial}{\partial r}\left[\frac{1}{r}\frac{\partial}{\partial r}\left(rv_\theta\right)\right]+\frac{1}{r^2}\frac{\partial^2 v_\theta}{\partial \theta^2}+\frac{\partial^2 v_\theta}{\partial z^2}+\frac{2}{r^2}\frac{\partial v_r}{\partial \theta}\right\}-$$

$$-\eta_P\left[\frac{v_r}{r}\frac{\partial^2 P}{\partial r\partial \theta}+\frac{v_\theta}{r^2}\frac{\partial^2 P}{\partial \theta^2}+\frac{v_z}{r}\frac{\partial^2 P}{\partial z\partial \theta}+\frac{v_\theta}{r}\left(\frac{\partial P}{\partial r}\right)+\frac{v_r}{r^2}\left(\frac{\partial P}{\partial \theta}\right)\right]+\frac{1}{r}\frac{\partial P}{\partial \theta}$$

Conservation of axial momentum equation (A.32):

$$\rho\left(\frac{\partial v_z}{\partial t}+v_r\frac{\partial v_z}{\partial r}+\frac{v_\theta}{r}\frac{\partial v_z}{\partial \theta}+v_z\frac{\partial v_z}{\partial z}\right)=\mu\left\{\frac{\partial}{\partial r}\left[\frac{1}{r}\frac{\partial}{\partial r}\left(rv_z\right)\right]+\frac{1}{r^2}\frac{\partial^2 v_z}{\partial \theta^2}+\frac{\partial^2 v_z}{\partial z^2}\right\}+\frac{\partial P}{\partial z}+$$

$$+\eta_P\left[v_r\frac{\partial^2 P}{\partial r\partial z}+\frac{v_\theta}{r}\frac{\partial^2 P}{\partial \theta \partial z}+v_z\frac{\partial^2 P}{\partial z^2}\right]$$

Conservation of mass (continuity) equation (A.33)

$$\frac{1}{r}\frac{\partial}{\partial r}\left(rv_r\right)+\frac{1}{r}\frac{\partial v_\theta}{\partial \theta}+\frac{\partial v_z}{\partial z}=0$$

The current research has examined the stability of a steady, axial vortex represented by Equation. 1·4, incorporating these non-equilibrium pressure gradient effects. The growth (or decay) of these instabilities is important both in terms of identifying complimentary steady vortex flows, and in understanding the evolution of the localized turbulent regions that are observed around the axial vortex core. In addition, development of possible strategies to either stabilize or destabilize these axial vortices will be sought.

1.4 Instability of axial vortex flow

The factors leading to turbulence in vortical flows include firstly the axial injection of perturbations from the surrounding flow; an example of the point of injection is the wing tip of an airplane. Secondly, the vortex itself is susceptible to instabilities resulting from naturally-occurring ambient fluctuations. Thirdly, small-scale streak-like structures are accommodated naturally by the non-linear features of the governing equations. To model unsteady and turbulent evolution numerically, Marshall (2000) has described three different regions for the vortex flow: a viscous core region with large centrifugal forces, an overlap region, and an outer mixing region.

Ash and Khorrami (1995) and Drazin and Reid (2004) outlined two ways to numerically model the inviscid vortical flows due to the kinetic features of perturbations in vortex flows. One method is to start with an initial guess for the growth rate and then iterate until the numerical scheme converges. This method requires special treatment for the integration over the centerline and core region of the vortex. The other numerical method is *global*, where the governing equations are written in matrix form, and the resulting eigenvalue problem is formulated; for every step the numerical scheme computes multiple eigenvalues according to the number of dependent variables and uses that solution as an initial guess for the next step and so on. The global method doesn't require an initial guess. In order to model viscous vortex flows, the equations must be linearized and then the matrix form of the resulting equations, after substituting the assumed perturbations, are integrated assuming an asymptotic solution at the limiting "infinite" radius.

Lacaze, Ryan, and Dizes (2007) studied different combinations of azimuthal modes for a pair of batchelor vortices, when applying constant strain, and generated stability

envelopes for different cases. The helical modes were the most unstable modes. Combinations of the n, and n+2 modes, where n= -2 and -3 become unstable when the axial flow is increased while the helical (odd) modes were damped. That study utilized Direct Numerical Simulation (DNS) to represent the instantaneous flow and the results were compared to theory with good agreement.

Hussain, Pradeep and Stout (2011) studied the transient growth of small perturbation amplitudes inside vortex flows, also using DNS for axial vortex flows up to a circulation-based Reynolds number of 10,000. The velocity field was assumed to have a rotational component due to vorticity and a potential flow component, in addition to the steady state velocity field. An initial vorticity field was prescribed and then the equation for vorticity was forward-integrated until the solution converged. The perturbations were injected inside the flow at a critical radius outside of the core radius where the waves experienced the largest growth. Average perturbation amplitudes, on the order of 5%, could alter the core, and secondary structures (finer scales) called coherent structures were generated accordingly. At that perturbation level, the non-linear effects carried the secondary structures radially outward and part of the perturbation energy was transferred from the critical radius region outward. Concurrently, the flow became turbulent, completing a cycle of bifurcation inside the basic vortex flow. The first azimuthal mode of instability grew faster than the axisymmetric mode and observed at smaller radii. As the Reynolds number increased, the turbulence tended to persist in the flow for longer durations. The turbulence at a Reynolds number of 10^6 distorted the vortex column. Hussain, Pradeep and Stout (2011) concluded that this effect of turbulence growth inside the vortex column was the cause of an airplane crash under the influence of another large

leading airplane, therefore air traffic bottle necks are imposed at major airports to avoid such incidents.

1.5 Experimental representation of vortex behavior

To understand the unsteady behavior of actual vortices, wind tunnel experiments can be conducted using vortex generators (Roy ,2011) and (Beninati and Marshall, 2000, 2005). Vortex generators are devices used to create laboratory-scale vortices, avoiding the tilting of the axial rotational centerline due to lift-induced downwash forces. Usually vortex generators are pairs of wings (one or more pairs) with equal, but opposite angles-of-attack. The axial vortex that evolves extends downstream behind the generator without experiencing the downwash effect.

Bandyopadhyay, Stead and Ash (1991) studied the turbulent nature of a trailing line vortex extending behind a bi-wing mounted in a low speed wind tunnel. The Reynolds number ranged between 15,000 and 25,000 based on maximum swirl velocity and core radius. The mean flow was characterized using a seven-hole vortex probe and a hotwire anemometer was employed to measure turbulence intensities. The axial core region was observed to be intermittent rather than approximating a solid-body-like rotating column, due to turbulence ingestion and associated viscous re-laminarization as the flow advanced in the axial direction. That flow effect was followed by the ejection of turbulent structures radially outwards. The turbulence intensities changed with the axial variation of the mean flow in terms of Rossby number more than with respect to changes in Reynolds number.

Jaarsveld et. al. (2011) performed a similar study utilizing Particle Image Velocimtry (PIV) technology to study the influence of external turbulence on single and

paired trailing line vortices in a wind tunnel. Their conclusion for the single vortex included a movement of the vortex center when the turbulence intensity was changed. The core was found to be laminar with inner Lamb-Oseen velocity profiles and outer power law profiles.

Flow visualization and velocity measurements can be acquired utilizing PIV, which utilizes a laser to illuminate a flow plane containing smoke particles within a wind tunnel flow; then particle image pairs are captured in closely-spaced (in time) high resolution, stereoscopic camera images. The resulting PIV data are supplied to a microcomputer utilizing special software to identify and track specific smoke particles in successive image frames, converting that data into a collection of particle velocity vectors. Multiple sets of these particle velocity frames can be processed subsequently to yield mean velocity profiles along with the associated turbulent intensities. The limitation to this technique is the camera image sampling rate and accordingly the range of turbulent intensities that can be measured is limited by that frequency.

Hotwire anemometers have been used for some time for precise temporal measurement of unsteady velocity components at specific spatial locations in a flow. Hotwires cannot measure fine-scale turbulent structure due to the overall size of the sensing elements and the diameter of the sensing filament (either a hot film or a hot wire). They can capture higher-frequency velocity fluctuations than can PIV systems, meaning they can resolve frequencies that are high enough to capture most instability modes. Dual-wire sensing probes can resolve three-dimensional, unsteady velocities through the inclination adjustment and angle between crossed wires. The disadvantages of hotwire anemometer

systems are their limitation of measuring velocities at a single, fixed point, along with limitations resulting from sensor materials and fabrication, as well as their fragility.

1.6 Wind tunnel experiments at ODU

A bi-wing vortex generator apparatus was employed to produce axial vortices in the Old Dominion University Low Speed Wind Tunnel (ODU LSWT). The vortex generator was positioned at the front end of the high-speed test section in order to allow the largest possible range of flow speeds. Near-steady axial vortices were generated along the centerline of the high-speed test section, and wind speeds ranging from 15 to 35 m/s could be utilized. The velocity surveys were produced at interrogation planes located at distances between 35 and 80 cm behind the trailing edges of the bi-wing vortex-generator.

A smoke particle generator was used to seed the wind tunnel flow and particle velocities within wind tunnel cross sections illuminated using a laser sheet were obtained utilizing a dual-camera stereoscopic particle imaging velocimetry (PIV) system. The PIV software was able to process the particle velocity data and generate two- and three-dimensional velocity fields characterizing the particular wind tunnel flow cross section. PIV also calculated intensities of physical quantities like the turbulent kinetic energy, shear stresses, and shear rates. The nominal turbulence level in the tunnel is estimated 0.2 % and the velocity of the fluid is captured using Particle Image Velocimetry (PIV) or hot-wire manometers.

The limitation on PIV technology is the frequency of capturing images; hopefully further breakthrough of camera resolution will advance the technology to higher frequency ranges, where the modes of instability can be found.

Five experimental data sets were generated by Jeff Ely (2013) and are characterized in Table 1.1. The maximum measured azimuthal velocity and its associated radial measurement location with respect to the vortex center of rotation were used to characterize the basic vortex. The far-field vortex circulation, Γ (m^2/s) was assumed to be twice the circulation measured at the core of the vortex, based on theory, i.e.

$$\Gamma = 2\pi r_c V_{\theta,\max} \tag{1.9}$$

However, this assumption may not be accurate, due both to differences between the actual vortex velocity field and the theoretical velocity profile and to possible flow modifications produced by interactions with the wind tunnel walls. The characteristic Reynolds number is defined as $\frac{r_c V_{\theta,\max}}{\nu}$.

Parameter	Run 1	Run 2	Run 3	Run 4	Run 5	Run 6	Run 7	Run 8	Run 9	Run 10
U_∞, *m/s*	15	17	19	21	23	25	27	29	31	33
T_{db}, *°C*	21.7	21.8	22.0	22.2	22.5	22.8	24.7	25.0	24.7	24.2
Rh, *%*	61	61	60	60	60	60	53	47	54	54
η_P, *μsec.*	0.38	0.38	0.39	0.39	0.39	0.39	0.42	0.45	0.42	0.42
r_c, *mm*	18.6	12.7	14.7	16.2	16.5	15.6	11.7	15.0	14.7	18.4
$V_{\theta,max}$, *m/s*	4.1	4.6	4.9	5.7	6.1	6.9	7.5	7.5	7.8	8.8
Γ, *m^2/s*	1.0	0.7	0.9	1.2	1.3	1.3	1.1	1.4	1.4	2.0
f_n, *Hz*	70.7	116.5	106.1	112.6	118.2	141.0	203.7	158.6	169.6	152.1
Re, *1*	5,104	3,932	4,819	6,193	6,745	7,153	5,516	6,997	7,649	10,762

Table 1.1. Reference data from ODU low speed wind tunnel

The other vortex parameter given in Table 1.1, is the natural frequency f_n (Hz) defined as the maximum azimuthal velocity of the vortex divided by the core radius. The

wind tunnel conditions for the particular test (tunnel air temperature T_{db}, relative humidity Rh, and theoretical value for the pressure relaxation coefficient η_P) are also listed.

1.7 Summary

The first chapter pointed out the importance of the axial vortex behavior study. It brings insight into the efforts made to model the steady axial vortex behavior with focus in the pressure relaxation model. The instability of the vortex flow was reviewed with a general understanding of the problem. Finally, experimental support work at ODU was listed as the ongoing research to extend the current work.

CHAPTER 2

STATE SPACE MODELING -BACKGROUND

2.1 Definitions

State-variable models have been used to describe state-control of electrical engineering systems for a very long time and have proven to be very stable even when dealing with non-linear equations according to Blais (1988). Bourles and Kwan (2013) described the state-variable approach as representing systems of higher order differential equations by a set of first-order equations. The *n*-dimensional mathematical domain in which this mapping representation takes place is called the *state-space.* The *state variables*, defining the system at any point, are the internal variables for the n-dimensional coordinate system. The state-variable method produces combinations of state variables that have physical meaning, generated in the form of output vectors.

The number of state variables varies from one dynamic system to another, but in all cases there must be at least a minimum number of state variables that can be identified, and that completely define the system at any point. The system will be defined according to the final number of state variables. In addition, it should be possible to determine the output vector from the state variables without requiring additional information or definitions. Thus, the state space representation incorporates a complete set of equations that represent input and output vectors, defined in terms of the state variables representing the system. It is very important to point out that while the minimum number of state variables required to define the system is unique, the state variable approach allows additional combinations of

these defined state variables, as long as the system has more than the minimum number of state variables.

The state variable model is expressed mathematically as a set of first-order, partial or ordinary differential equations known as *state-equations*. Rowell (2002) defined the state equation to be written for each derivative of each state variable, in terms of the state variables, along with the initial inputs to the system. The output vector can be any combination of state variables, as desired, for the physical problem.

For the analysis of complex systems with nonlinear elements, it is often appropriate to use matrix and vector methods. Rowell (2002) and Bourles and Kwan (2013) demonstrated that cases when multiple inputs are involved in developing solutions with multiple outputs, the state space numerical methods are ideal and self-consistent. The method employed in this research is called a *state variable representation.* The method is applicable to linear systems as well as non-linear systems with multiple input and output variables.

Meyer and Mathies (2004) utilized a state space representation to investigate the stability and sensitivity of wind turbine numerical schemes after including non-stationary aerodynamic loads. An important point raised in the study was that the state space representation produced meaningful results since it was based on flow physics.

Brunton and Rowley (2013) constructed a state space model and the corresponding transfer function of the generalized Theodorsen lift function, an unsteady behavior model for studying the aerodynamics of aircrafts and associated control loops. The proposed model retained the basic attributes of the theoretical Theodersen's model. An empirically based DNS version of Theodersen's model for a flat plate data pitching at low Reynolds

number was used to adjust the coefficients of the state variable model. Thus the model utilized both empirical and numerical simulations to define the system. A low order state variable model was also developed and demonstrated good agreement with empirical data. Their model implied the possibility of studying unsteady boundary layer physics at low Reynolds number and other unsteady phenomena using state variable modeling.

Taha, Hajj, and Beran (2014) developed a state variable model for studying the unsteady aerodynamics of flapping flight. The model was validated using direct numerical simulation data and produced good agreement at a lower computational cost than the classical unsteady models. The model had included one hundred state variables of the system. A reduced order model employing only the four main state variables was also proposed with an acceptable fit to the reference data.

2.2 Current Application

In classical mechanics, rotational flows have been described using the Navier-Stokes equations. Usually, the highest derivatives contained in the differential equations governing velocity are second order, while the highest order pressure derivatives are first order. The conventional conservation of momentum equations don't contain any velocity-pressure contracted terms; thus, the pressure gradient terms can be isolated from the governing equations by utilizing the curl of the vector form of the conservation of momentum equation.

This study has incorporated the pressure relaxation modification of the N-S equations, and, as a consequence, unsteady and convective pressure gradient terms in three dimensions are introduced. Conventional mathematical and numerical approaches fail to

solve these modified N-S equations for many reasons. One reason is the velocity-pressure contracted terms in the modified N-S equations (Equations A-30 to A-32 in Appendix A) make it difficult to isolate pressure. In addition, the sensitivity of most mathematical models to characteristic propagation speeds presents severe challenges to space-wise grid size/time step specifications because the appropriate "pressure relaxation time steps" are expected to be on the order of micro seconds whereas characteristic vortex velocity and characteristic length-based time steps can be many orders of magnitude larger. For these reasons, a more physics-based numerical model was required for the modified N-S equations.

Presently, the primary challenge is to develop a state variable model to solve the modified Navier-Stokes equations for this type of vortical flow. The flow incorporates a significant pressure deficit in the vicinity of the centerline which allows the non-equilibrium pressure forces to be present in the flow analysis. The state variable model development for this particular application follows.

2.3 Theory and assumptions

Blais (1988) showed that state variables for a large number of real physical processes have Gaussian noise distributions. It is not only practical to assume Gaussian state variables but also simpler to carry out the mathematical calculations.

In cases where repetitive estimations of the state vector amplitudes are required throughout the computational domain, it is also important to assume that the state vectors are *Markovian.* In addition to possessing the Gaussian noise property the Markovian property means that, in order to estimate the state vector at different locations in space and

time, it is only necessary to possess knowledge of the value of the state vector from the previous step, along with the transitional functions which determine the value of the state vector at the current location or instant.

In axial vortex flow, the parameters that determine the characteristics of the flow at some location and/or time are assumed to satisfy the Markovian property requirement. For instance, the parameters could be designated

$$x(r_1, z_1), x(r_2, z_2), x(r_3, z_3), \ldots, x(r_N, z_N)$$

where x could be a scalar (e.g. pressure perturbation) or a vector (e.g. velocity perturbation), while the subscripted (r,z) independent variables are the selected radial and axial coordinate locations, and the subscript integer , N, is the total number of specified points in the computational domain. These variables are assumed to be Markovian and the probability density distribution function for different state vectors (x) at specific locations (r_{k-1}, z_{k-1}), as represented by $p[x(r_{k-1}, z_{k-1})]$, depending only on the previous value $x(r_k, z_k)$ and not on $x(r_{k-l}, z_{k-l})$, $l = 1,2,\ldots$, in the sense that the Markovian property isolates the present "event" or "location" from past and future events or locations. Bryson (1975) and Blais (1988) commented that this generalized concept of the Markovian property enables representation of a great variety of physical phenomena.

The state variable model is applied to this axial vortex flow, exploiting the capabilities just outlined. The system is assumed to be fully represented by a set of state variables containing velocity and pressure amplitudes and their first derivatives. The radial coordinate locations where the state variables are estimated are measured from the centerline outwards. At each radial location, the perturbations in the flow are governed by

the perturbation equations (developed in the next chapter). Each state variable derivative must have a distinct governing equation.

2.4 Formulation of the model

Formulation of the state variable representation of the vortex flow system being investigated here is initiated by defining precisely the state variables in terms of continuous differential equations. Here, the state variables are the amplitudes of the velocity and pressure perturbations, along with their first partial derivatives with respect to the radial and axial coordinates. Palm (2010) represented the general form of the state equations symbolically as follows:

$$[\dot{\mathbf{x}}] = [\mathbf{A}][\mathbf{x}] + [\mathbf{B}][\mathbf{u}] \tag{2.1}$$

where [**x**] is the state variable vector, [**A**] and [**B**] are coefficient matrices, and [**u**] is the external input vector (a small disturbance to the initially-steady vortex flow being examined). The role of the external input vector is to initialize the stability problem. The matrix [**A**] for the vortex flow under study contains the coefficients of the conservation of momentum and Poisson's pressure equations, those coefficients are functions of r and the parameters characterizing the flow. The coefficient matrix [**B**] will have diagonal elements equal to unity and, depending on the state variables initialized, it could be a rectangular matrix.

As the solution to the state-variable differential equation progresses, the small perturbations introduced via **[u]** will either decay or grow, resulting either in a more complicated flow or, most-likely becoming turbulent. The physical basis for the external

input is the small pressure disturbances that can be generated inside the flow. The solution progresses utilizing the integration step

$$[\mathbf{y}] = \iint [\mathbf{A}][\mathbf{x}] dr dz \ , \tag{2.2}$$

to proceed through successive locations in the spatial domain. This solution is used as an initial solution for the next space-wise step. The integration is continued in the radial direction out to the specified maximum number of points (N), assuming that numerical integration is done at a fixed axial coordinate value (z-location). Numerical data produced in this study has shown that the state-space approach can proceed successfully out to negligible disturbance values by the time the limiting radial far field boundary was reached, meaning that it was not necessary to enforce a far-field amplitude specification. Thus, the double integration could be effected at the next axial cross section location. The output of the state variable representation of vortex flow is represented:

$$[\mathbf{y}] = [\mathbf{C}][\mathbf{x}] \tag{2.3}$$

where (**y**) is the output vector, and $\mathbf{C}=\begin{bmatrix} 1 & \dots & 0 \\ 0 & \dots 1 \dots & 0 \\ 0 & \dots & 1 \end{bmatrix}$ is the identity matrix.

A block diagram of the state variable model employed here is shown in Figure 2.1. In that figure, the random noise is scaled by a factor, B, and added to the system as an external input, and an integrated feedback state variable vector is employed at the starting node.

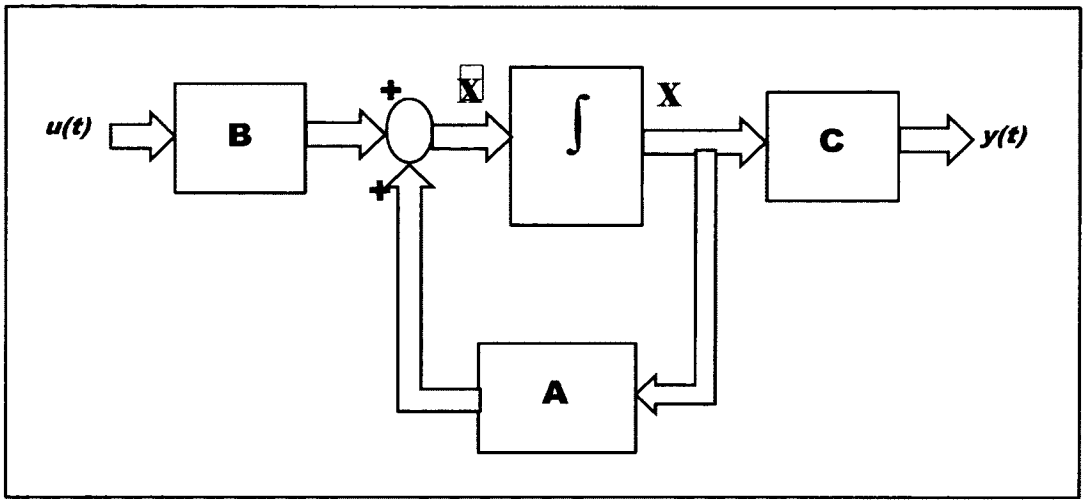

Figure 2.1 Vector block diagram for the state variable model

The resulting inputs are used to initialize the derivatives of the state-variables, denoted by $\dot{\mathbf{x}}$. A summation element (integral operator) is needed after the derivative calculation, in order to produce the step solution $\mathbf{x}$. This solution is utilized as feedback to the next step with a scaling parameter which is the matrix of coefficients **A**. This feedback solution is added via the summation point to yield the new input values for the derivatives of the state variable vector, $\dot{\mathbf{x}}$. Finally, the output of the state variable model y(t) is computed via a scaling parameter C (equal to unity in this study).

The state variable model will now be considered specifically for the reference axial vortex flow, perturbed from its steady-state solution by small amplitude perturbations. A modified set of Navier-Stokes equations incorporating the pressure relaxation terms will be developed in two dimensions and a pressure equation of Poisson type will be used to close the system of equations.

CHAPTER 3

GOVERNING PERTURBATION EQUATIONS FOR AN UNSTEADY AXIAL VORTEX FLOW

A three-dimensional unsteady set of governing perturbation equations for this incompressible vortex flow in cylindrical coordinates (neglecting gravity) will be developed, in preparation for the subsequent state variable-based analysis.

3.1 Formulation of the problem

Utilizing the exact non-equilibrium pressure solution by Ash, Zardadkhan and Zuckerwar (2011), the problem under consideration is the behavior of this type of vortex when it is subjected to small, unsteady departures from steady-state behavior. The conditions under which the steady, axial vortex becomes unstable and tends toward chaotic or turbulent behavior will be studied incorporating non-equilibrium pressure gradient forces. The relatively large pressure gradient forces within the non-equilibrium pressure zone represent a new avenue of research since those forces can alter the relaxation behavior of induced perturbations.

The perturbation solution is assumed to evolve, starting from an axial location where changes in the axial direction are so gradual that they can be ignored in the current investigation. Consequently, the primary focus of this investigation will be on the radial evolution of random perturbations introduced within the flow. In the meantime, these radial growing instability modes occur at different azimuthal orientations forming two or three modes with the same radial growth trend. Hence, the problem under consideration in this study represents an unsteady two-dimensional (radial and azimuthal) evolution of the basic vortical flow incorporating pressure relaxation.

3.1.1 The velocity and pressure fields

The azimuthal and radial velocity components and pressure are assumed to be decomposed in terms of the basic, steady-state solutions in the following manner:

$$v_\theta(r,\theta,t) = V_\theta(r) + v_\theta'(r,\theta,t) = 2V_{\theta,\max}\frac{r/r_{core}}{r/r_{core}+1} + v_\theta'(r,\theta,t)$$

$$v_r(r,\theta,t) = v_r'(r,\theta,t)$$

and (3.1)

$$P(r,\theta,t) = \bar{P}(r) + p'(r,\theta,t) = P_\infty - 4\frac{\mu}{\eta_p}\frac{1}{\left(r/r_{core}\right)^2+1} + p'(r,\theta,t)$$

where $r_{core} = \frac{\Gamma}{4\pi\sqrt{2}}\sqrt{\frac{\eta_P}{\nu}}$ and $V_{\theta,\max} = \sqrt{\frac{2\nu}{\eta_P}}$. The primed variables represent the perturbation contributions, whose magnitudes are assumed to be very small compared with the steady-state velocity and pressure distributions. This system of equations is amenable to a "small departures from steady-state" approach that will be developed in the next sections.

3.1.2 Assumptions

Before normalizing the governing equations, the perturbed velocity and pressure field representations, equations 3·1, were substituted into the governing equations, and the terms that constituted the original steady-state governing equations, and the associated steady-state solution, were removed. Subsequently, quadratic terms in the perturbation variables were assumed to be negligibly small.

3.2 Non-Dimensionalization

The modified Navier-Stokes equations have been normalized using the *core radius* ($r_c = r_{core}$) as the characteristic length and the maximum swirl velocity ($V_{\theta,\max}$) as the

velocity scale. The characteristic time and pressure magnitudes have been formulated using the basic length and velocity scales. Table 3.1, summarizes the different scaling parameters.

Length	r_c
Velocity	$V_{\theta,max}$
Pressure	$\rho\, V_{\theta,max}^{\ 2}$
Time	$r_c/V_{\theta,max}$

Table 3.1. Non-dimensional Scaling Parameters

The resulting dimensionless steady-state velocity and pressure solutions can be written:

$$V_\theta(r) = \frac{2r}{r^2 \square 1}, \text{ and } \quad \overline{P}(r) = \overline{P}_\infty \square \frac{2}{r^2 \square 1} \tag{3.2}$$

3.2.1 Conservation of mass in dimensionless form

Since the steady-state solution satisfies the continuity equation trivially, and that equation is linear, the continuity equation will be written in terms of the perturbation variables,

$$\frac{1}{r}\frac{\partial}{\partial r}\square rv_r' \square \square \frac{1}{r}\frac{\partial v_\theta'}{\partial \theta} = 0 \tag{3.3}$$

3.2.2. Conservation of linear Momentum in dimensionless form

From Equations A-30 and A-31 in Appendix A, the normalized conservation of momentum equations in cylindrical coordinates, considering only two independent spatial

variables (r and θ) can be written incorporating a non-equilibrium swirl parameter, $Np = \frac{\eta_P v_{\theta,\max}}{r_c}$, as:

Conservation of radial momentum

$$\frac{\partial v_r}{\partial t} + v_r \frac{\partial v_r}{\partial r} + \frac{v_\theta}{r}\frac{\partial v_r}{\partial \theta} - \frac{v_\theta^2}{r} = \frac{1}{\mathrm{Re}}\left\{\frac{\partial}{\partial r}\left[\frac{1}{r}\frac{\partial}{\partial r}\left(r v_r\right)\right] + \frac{1}{r^2}\frac{\partial^2 v_r}{\partial \theta^2} - \frac{2}{r^2}\frac{\partial v_\theta}{\partial \theta}\right\} +$$

$$+ Np\left[\frac{\partial^2 P}{\partial t \partial r} + v_r \frac{\partial^2 P}{\partial r^2} + \frac{v_\theta}{r}\frac{\partial^2 P}{\partial \theta \partial r} + \frac{v_\theta}{r^2}\left(\frac{\partial P}{\partial \theta}\right)\right] + \frac{\partial P}{\partial r} \qquad (3.4)$$

Conservation of azimuthal momentum

$$\frac{\partial v_\theta}{\partial t} + v_r \frac{\partial v_\theta}{\partial r} + \frac{v_\theta}{r}\frac{\partial v_\theta}{\partial \theta} + \frac{v_r v_\theta}{r} = \frac{1}{\mathrm{Re}}\left\{\frac{\partial}{\partial r}\left[\frac{1}{r}\frac{\partial}{\partial r}\left(r v_\theta\right)\right] + \frac{1}{r^2}\frac{\partial^2 v_\theta}{\partial \theta^2} + \frac{2}{r^2}\frac{\partial v_r}{\partial \theta}\right\} +$$

$$+ Np\left[\frac{1}{r}\frac{\partial^2 P}{\partial t \partial \theta} + \frac{v_r}{r}\frac{\partial^2 P}{\partial r \partial \theta} + \frac{v_\theta}{r^2}\frac{\partial^2 P}{\partial \theta^2} + \frac{v_\theta}{r}\left(\frac{\partial P}{\partial r}\right) + \frac{v_r}{r^2}\left(\frac{\partial P}{\partial \theta}\right)\right] + \frac{1}{r}\frac{\partial P}{\partial \theta} \qquad (3.5)$$

Substituting the perturbation variables, defined in Equation (3.1), removing the steady-state solution, and then neglecting the quadratic terms, yields the following non-dimensional perturbation governing equations:

Perturbation conservation of radial momentum equation

$$\frac{\partial v_r'}{\partial t} + \frac{V_\theta}{r}\frac{\partial v_r'}{\partial \theta} - 2\frac{V_\theta v_\theta'}{r} = \frac{1}{\mathrm{Re}}\left\{\frac{\partial}{\partial r}\left[\frac{1}{r}\frac{\partial}{\partial r}\left(r v_r'\right)\right] + \frac{1}{r^2}\frac{\partial^2 v_r'}{\partial \theta^2} + \frac{2}{r^2}\frac{\partial v_\theta'}{\partial \theta}\right\} +$$

$$+ Np\left[\frac{\partial^2 p'}{\partial t \partial r} + v_r' \frac{d^2 P}{dr^2} + \frac{V_\theta}{r}\frac{\partial^2 p'}{\partial \theta \partial r} + \frac{V_\theta}{r^2}\left(\frac{\partial p'}{\partial \theta}\right)\right] + \frac{\partial p'}{\partial r} \qquad (3.6)$$

Perturbation conservation of azimuthal momentum

$$\frac{\partial v_\theta'}{\partial t} + v_r'\frac{dV_\theta}{dr} + \frac{V_\theta}{r}\frac{\partial v_\theta'}{\partial \theta} + \frac{v_r' V_\theta}{r} = \frac{1}{\mathrm{Re}}\left\{\frac{\partial}{\partial r}\left[\frac{1}{r}\frac{\partial}{\partial r}\left(r v_\theta'\right)\right] + \frac{1}{r^2}\frac{\partial^2 v_\theta'}{\partial \theta^2} + \frac{2}{r^2}\frac{\partial v_r'}{\partial \theta}\right\} +$$

$$Np\left[\frac{1}{r}\frac{\partial p'}{\partial \theta \partial t} + \frac{V_\theta}{r^2}\frac{\partial^2 p'}{\partial \theta^2} + \frac{V_\theta}{r}\frac{\partial p'}{\partial r} + \frac{dP}{dr}\frac{v_\theta'}{r}\right] + \frac{1}{r}\frac{\partial p'}{\partial \theta} \qquad (3.7)$$

where $\mathrm{Re} = \frac{v_{\theta,\max} r_c}{\nu}$ is the Reynolds number based on the maximum azimuthal speed. Since the *Non-equilibrium swirl parameter, Np*, is a new dimensionless parameter, it warrants further discussion.

3.3 Non-equilibrium swirl parameter, (*Np*)

The non-equilibrium swirl parameter evolves logically from the dimensionless formulation of the perturbation equations. It has been defined as:

$$Np = \frac{\eta_P v_{\theta,\max}}{r_c} = \eta_P \omega \qquad (3.8)$$

where the quantities r_c, η_P, and $v_{\theta,\max}$ depend on the properties and characteristics of the underlying axial vortex. The non-equilibrium swirl parameter represents the ratio of the characteristic non-equilibrium relaxation time of fluid particles to the convective time characterizing particle movement in the vicinity of the vortex core, where the swirl velocities are largest.

As was mentioned in the introduction, when non-equilibrium pressure gradient forces are introduced into the Navier-Stokes equations governing an incompressible axial vortex, the resulting vector form of the modified Navier-Stokes equation no longer permits the utilization of the curl of the (classical) Navier-Stokes equation to eliminate pressure. A

new type of Poisson equation was required to model the perturbation pressure and that equation will be developed next.

3.4 The Pressure Poisson equation

A common numerical problem in computer codes employed to model sets of partial differential equations with varying differential orders is that Computational Fluid Dynamics (CFD) codes must handle the second-order velocity difference equations (momentum) with first-order pressure gradients, along with the first order continuity equation for incompressible flows. The solution in these classical cases require more computing time because the program must solve for the velocity field first, then close the solution by estimating the pressure field required to keep the incompressible flow solenoidal. In this study, the divergence of the perturbation momentum equations, incorporating the continuity equation, enables the development of a second order equation for the pressure perturbations and facilitates exploring the stability of the resulting numerical scheme. The Poisson-like equation governing the pressure perturbations is new and has been employed for the first time in the present study. That derivation starts by taking the divergence of the conservation of momentum equation, after first recognizing from the continuity equation (Appendix B is used as a reference for the equations in this section) that $\nabla \cdot \left(\frac{\partial \mathbf{v}}{\partial t} \right) = \frac{\partial}{\partial t} [\nabla \cdot \mathbf{v}] = 0$, so that,

$$\nabla \cdot \frac{D\mathbf{v}}{Dt} = \nabla \cdot [\mathbf{v} \cdot \nabla \mathbf{v}] = \left(-1 - Np \frac{\partial}{\partial t} \right) \nabla^2 P - Np \nabla \cdot [\mathbf{v} \cdot \nabla \nabla P],$$

Employing the curvilinear coordinate derivation of this equation described in Appendix B, the equation term-by-term development yields:

Gradient of the unsteady particle acceleration expression

$$\nabla\cdot\left[\mathbf{v}\cdot\nabla\mathbf{v}\right]=\left[\left(\frac{\partial v_r}{\partial r}\right)^2+\frac{1}{r^2}\left(\frac{\partial v_\theta}{\partial\theta}\right)^2+\frac{v_r}{r^2}\frac{\partial v_\theta}{\partial\theta}+\frac{v_r}{r}\frac{\partial v_r}{\partial r}\right]+2\frac{\partial v_r}{\partial\theta}\frac{\partial}{\partial r}\left(\frac{v_\theta}{r}\right)+2v_\theta\frac{\partial}{\partial r}\left(\frac{v_\theta}{r}\right)+2\frac{v_\theta}{r^2}\frac{\partial v_r}{\partial\theta}+2\frac{v_\theta^2}{r^2}$$

Divergence of the relaxation stress term

$$-\nabla^2P+Np\vec{\nabla}\cdot\left[\frac{D}{Dt}\vec{\nabla}P\right]=\left(-1+Np\frac{\partial}{\partial t}\right)\nabla^2P+Np\vec{\nabla}\cdot\left[\mathbf{v}\cdot\vec{\nabla}\vec{\nabla}P\right]=$$

$$\left(-1+Np\frac{\partial}{\partial t}\right)\left[\frac{1}{r}\frac{\partial}{\partial r}\left(r\frac{\partial P}{\partial r}\right)+\frac{1}{r^2}\frac{\partial^2P}{\partial\theta^2}\right]+\frac{Np}{r}\frac{\partial}{\partial r}\left\{r\left[v_r\frac{\partial^2P}{\partial r^2}+\frac{v_\theta}{r}\frac{\partial^2P}{\partial r\partial\theta}+\frac{v_\theta}{r^2}\left(\frac{\partial P}{\partial\theta}\right)\right]\right\}$$

$$+\frac{Np}{r}\frac{\partial}{\partial\theta}\left[\frac{v_r}{r}\frac{\partial^2P}{\partial r\partial\theta}+\frac{v_\theta}{r^2}\frac{\partial^2P}{\partial\theta^2}+\frac{v_r}{r^2}\left(\frac{\partial P}{\partial\theta}\right)+\frac{v_\theta}{r}\left(\frac{\partial P}{\partial r}\right)\right]$$

Then, from the perturbation assumption equation (3·1) the resulting perturbation expression for the gradient of the unsteady particle acceleration expression after excluding the steady-state solution and quadratic terms is,

$$\nabla\cdot\left[\mathbf{v}\cdot\nabla\mathbf{v}\right]=\frac{2}{r}\frac{dV_\theta}{dr}\frac{\partial v_r'}{\partial\theta}+\frac{2V_\theta}{r}\frac{\partial v_\theta'}{\partial r}+\frac{2}{r}\frac{dV_\theta}{dr}v_\theta',$$

and the *divergence of the relaxation stress term is,*

$$-\nabla^2P+Np\vec{\nabla}\cdot\left[\frac{D}{Dt}\vec{\nabla}P\right]=Np\frac{d^2\overline{P}}{dr^2}\frac{\partial v_r'}{\partial r}+Np\left(\frac{d^3\overline{P}}{dr^3}+\frac{1}{r}\frac{d^2\overline{P}}{dr^2}\right)v_r'+$$

$$+\left(-1+Np\frac{\partial}{\partial t}\right)\left[\frac{1}{r}\frac{\partial}{\partial r}\left(r\frac{\partial p'}{\partial r}\right)+\frac{1}{r^2}\frac{\partial^2p'}{\partial\theta^2}\right]+Np\left(\frac{1}{r}\frac{dV_\theta}{dr}+\frac{V_\theta}{r^2}\right)\frac{\partial^2p'}{\partial r\partial\theta}+Np\frac{V_\theta}{r}\frac{\partial^3p'}{\partial r^2\partial\theta}$$

$$+Np\frac{V_\theta}{r^3}\frac{\partial^3p'}{\partial\theta^3}+Np\left(+\frac{1}{r^2}\frac{dV_\theta}{dr}+\frac{V_\theta}{r^3}\right)\frac{\partial p'}{\partial\theta}+\frac{Np}{r^2}\frac{d\overline{P}}{dr}\frac{\partial v_\theta'}{\partial\theta}$$

The complete pressure equation becomes,

$$\frac{2}{r}\frac{dV_\theta}{dr}\frac{\partial v_r'}{\partial\theta} - \frac{2V_\theta}{r}\frac{\partial v_\theta'}{\partial r} - \frac{2}{r}\frac{dV_\theta}{dr}v_\theta' = Np\frac{d^2\overline{P}}{dr^2}\frac{\partial v_r'}{\partial r} - Np\left(\frac{d^3\overline{P}}{dr^3} - \frac{1}{r}\frac{d^2\overline{P}}{dr^2}\right)v_r' -$$

$$-\left(-1 - Np\frac{\partial}{\partial t}\right)\left[\frac{1}{r}\frac{\partial}{\partial r}\left(r\frac{\partial p'}{\partial r}\right) - \frac{1}{r^2}\frac{\partial^2 p'}{\partial\theta^2}\right] - Np\left(\frac{1}{r}\frac{dV_\theta}{dr} - \frac{V_\theta}{r^2}\right)\frac{\partial^2 p'}{\partial r\partial\theta} - Np\frac{V_\theta}{r}\frac{\partial^3 p'}{\partial r^2\partial\theta}$$

$$- Np\frac{V_\theta}{r^3}\frac{\partial^3 p'}{\partial\theta^3} - Np\left(-\frac{1}{r^2}\frac{dV_\theta}{dr} - \frac{V_\theta}{r^3}\right)\frac{\partial p'}{\partial\theta} - Np\frac{d\overline{P}}{dr}\frac{\partial v_\theta'}{\partial\theta} \quad (3.9)$$

3.5 Linear stability formulation

The perturbations imposed on the basic flow (with no pre-existing evidence of instability in the flow) utilize specified amplitude and frequency. In that way, they initiate instability in the flow by combining the most unstable modes of instability, travelling with a group velocity (dependent on the wave propagation speed of the source), and exhibiting an exponential amplification in the spatial domain as the group of modes progress. Drazin and Reid (2004) described the decay of these perturbations beyond some radial location, as resulting from modal interactions travelling with the group velocity, followed by a subsequent repeating instability mode and so on. Thus the instability modes grow only within a frame moving with the same velocity as the traveling modes.

For the vortex flow considered in this study, the perturbations extract mechanical energy from the mean flow and grow in the radial direction, carrying the most unstable vortical modes. The perturbations are assumed to be composed of periodic elements representing the initially-imposed, time-dependent functions. Roy et. al. (2011) discussed the mode of instability (characterized by a specific magnitude and frequency) that emerges in the flow and collectively travel in the spatial domain and grow exponentially causing the

flow to deviate from steady-state, those modes do not all persist in the flow and it is the amount of energy the mode carries that determines the dominant modes. Liang et al. (2002) explained that the dominant modes can be identified either using fast Fourier transform (FFT), power spectral density (PSD), or proper orthogonal decomposition (POD) methods

The perturbation variables have been represented as complex periodic functions in the following form:

$$\begin{aligned} v_r' &= iA(r)e^{i(\omega t - n\theta)} \\ v_\theta' &= B(r)e^{i(\omega t - n\theta)} \\ p' &= D(r)e^{i(\omega t - n\theta)} \end{aligned} \tag{3.10}$$

where amplitude functions *A,B,* and *D,* are non-dimensional complex functions of (r). In the following derivations, the real parts of these functions have subscripts (R) and the imaginary parts have subscripts (I), e.g. $A = A_R - iA_I$. The radial complex amplitude function, *A(r)*, is pre-multiplied by the complex root (i), in order to enforce perpendicularity of that component with respect to the azimuthal component.

The complex frequency (ω) is defined:

$$\omega = \omega_R - i\omega_I \tag{3.11}$$

where ω_R is the *circular frequency of the perturbation* and ω_I is the *damping factor.*

The perturbation conservation of momentum and the Poisson equation governing the pressure perturbations will now be rewritten in terms of these functions. For the purpose of facilitating the derivation, the following differential operators have been employed,

$$\frac{\partial}{\partial t} = e^{i(\omega_R t - i\omega_I t - n\theta)}(i\omega_R - \omega_I), \quad \frac{\partial}{\partial \theta} = e^{i(\omega_R t - i\omega_I t - n\theta)}(-in) \quad \frac{\partial^2}{\partial \theta^2} = e^{i(\omega_R t - i\omega_I t - n\theta)}(-n^2)$$

$$\frac{\partial}{\partial r} = e^{i(\omega_R t - i\omega_I t + n\theta)} \frac{\partial}{\partial r}, \quad \frac{\partial^2}{\partial r^2} = e^{i(\omega_R t - i\omega_I t + n\theta)} \frac{\partial^2}{\partial r^2},$$

and $\tilde{\nabla}^2 \equiv e^{i(\omega_R t - i\omega_I t + n\theta)} \left(\frac{\partial^2}{\partial r^2} + \frac{1}{r}\frac{\partial}{\partial r} - \frac{n^2}{r^2} \right)$.

where the derivatives of perturbation amplitudes with respect to r become total derivatives since we are assuming diffusion of disturbances in the radial direction only in this study.

Conservation of mass

The conservation of mass equation 3.3 becomes the following after substituting the perturbation assumption,

$$e^{i(\omega t + n\theta)} \left[i\frac{\partial (A_R + iA_I)}{\partial r} + \frac{iA_R + A_I}{r} + i\frac{n}{r}(B_R + iB_I) \right] = 0$$

Separating real and imaginary parts and factoring out the exponential,

The real part is,

$$\frac{dA_I}{dr} + \frac{A_I}{r} + \frac{n}{r} B_I = 0 \tag{3.12}$$

And the imaginary part is,

$$\frac{dA_R}{dr} + \frac{A_R}{r} + \frac{n}{r} B_R = 0 \tag{3.13}$$

Conservation of radial perturbation momentum

Substituting the perturbations into the equations (3·6), the radial perturbation of momentum equation becomes:

$$\left(-\omega A - i2\frac{V_\theta}{r}A - in\frac{V_\theta}{r}A\right)e^{i\omega_R t - i\omega_I t - n\theta} = e^{i\omega_R t - i\omega_I t - n\theta}\left\langle \frac{i}{\mathrm{Re}}\left\{\tilde{\nabla}^2 A - \frac{2n}{r^2}B\right\}\right\rangle -$$

$$- e^{i\omega_R t - i\omega_I t - n\theta}\left\langle Np\left[i\omega\frac{dD}{dr} - i\frac{d^2P}{dr^2}A - in\frac{V_\theta}{r}\frac{dD}{dr} - in\frac{V_\theta}{r^2}D\right] - \frac{dD}{dr}\right\rangle$$

Factoring out the exponential function, the resulting radial equation is:

$$\left(-\omega - i2\frac{V_\theta}{r} - in\frac{V_\theta}{r}\right)A = \frac{i}{\mathrm{Re}}\left\{\tilde{\nabla}^2 A - \frac{2n}{r^2}B\right\} - Np\left[i\omega\frac{dD}{dr} - i\frac{d^2P}{dr^2}A - in\frac{V_\theta}{r}\frac{dD}{dr} - in\frac{V_\theta}{r^2}D\right] - \frac{dD}{dr}$$

In complex form,

$$\left[-\omega_R - i\omega_I - i2\frac{V_\theta}{r} - in\frac{V_\theta}{r} - \frac{i}{\mathrm{Re}}\tilde{\nabla}^2 - iNp\frac{d^2P}{dr^2}\right](A_R - iA_I) =$$

$$- \frac{1}{\mathrm{Re}}\frac{2n}{r^2}(iB_R - B_I) - Np\left[(-\omega_R - i\omega_I)\left(-\frac{d}{dr} - n\frac{V_\theta}{r}\frac{d}{dr} - n\frac{V_\theta}{r^2}\right)\right](iD_R - D_I) - \frac{d}{dr}(D_R - iD_I)$$

The real part of this equation is:

$$\frac{1}{\mathrm{Re}}\tilde{\nabla}^2 A_R = -\left(\omega_I - 2\frac{V_\theta}{r} - n\frac{V_\theta}{r} - Np\frac{d^2P}{dr^2}\right)A_R - \omega_R A_I - \frac{1}{\mathrm{Re}}\frac{2n}{r^2}B_R$$

$$- n\cdot Np\frac{V_\theta}{r^2}D_R - Np\left(\omega_R - n\frac{V_\theta}{r}\right)\frac{dD_R}{dr} - 1 - Np\cdot\omega_I - \frac{dD_I}{dr} \quad (3.14)$$

Incorporating the steady-state solution yields,

$$\frac{1}{\mathrm{Re}}\tilde{\nabla}^2 A_R = -\left[\omega_I - \frac{4 - 2n}{r^2 - 1} - \frac{4Np(1 - 3r^2)}{r^2(1 - r^3)}\right]A_R - \omega_R A_I - \frac{1}{\mathrm{Re}}\frac{2n}{r^2}B_R$$

$$- \frac{2nNp}{r(r^2 - 1)}D_R - Np\left(\omega_R - \frac{2n}{r^2 - 1}\right)\frac{dD_R}{dr} - 1 - Np\cdot\omega_I - \frac{dD_I}{dr} \quad (3.15)$$

The corresponding imaginary part of the radial perturbation equation is:

$$\frac{1}{\mathrm{Re}}\tilde{\nabla}^2 A_I = \omega_R A_R - \left[\omega_I - 2n\frac{V_\theta}{r} - Np\frac{d^2P}{dr^2}\right]A_I - \frac{1}{\mathrm{Re}}\frac{2n}{r^2}B_I$$

$$- Np\cdot\omega_I - 1 - \frac{dD_R}{dr} - n\cdot Np\frac{V_\theta}{r^2}D_I - Np\left(\omega_R - n\frac{V_\theta}{r}\right)\frac{dD_I}{dr} \qquad (3.16)$$

Incorporating the steady-state solution (2·2), the imaginary part of the radial perturbation conservation of momentum equation is:

$$\frac{1}{\mathrm{Re}}\tilde{\nabla}^2 A_I = \omega_R A_R - \left[\omega_I - \frac{2-n}{r^2-1} - \frac{4Np(1-3r^2)}{(r^2-1)^3}\right]A_I - \frac{1}{\mathrm{Re}}\frac{2n}{r^2}B_I$$

$$- Np\cdot\omega_I - 1 - \frac{dD_R}{dr} - \frac{2n\cdot Np}{r(r^2-1)}D_I - Np\left(\omega_R - \frac{2n}{r^2-1}\right)\frac{dD_I}{dr} \qquad (3.17)$$

Conservation of azimuthal perturbation momentum

The azimuthal perturbation momentum Equation (3.8) becomes:

$$i\omega B - \left(\frac{dV_\theta}{dr} - \frac{V_\theta}{r}\right)A - in\frac{V_\theta}{r}B = \frac{1}{\mathrm{Re}}\left(\tilde{\nabla}^2 B - \frac{B}{r^2} - i\frac{2n}{r^2}A\right) -$$

$$Np\left[-\frac{n}{r}\omega D - \frac{n^2V_\theta}{r^2}D - \frac{1}{r}\left(\frac{dP}{dr}\right)B - \frac{V_\theta}{r}\frac{dD}{dr}\right] - i\frac{n}{r}D$$

and the complex form of the perturbation azimuthal momentum equation can be written as:

$$\left[\left(\frac{dV_\theta}{dr} - \frac{V_\theta}{r}\right) - i\frac{1}{\mathrm{Re}}\frac{2n}{r^2}\right]A_R - iA_I - \left[-\left[-\omega_I - Np\frac{1}{r}\left(\frac{dP}{dr}\right) - \frac{1}{\mathrm{Re}}\left(\tilde{\nabla}^2 - \frac{1}{r^2}\right)\right]B_R - iB_I -\right.$$

$$= -i\left(\omega_R - n\frac{V_\theta}{r}\right)B_R - iB_I - Np\frac{V_\theta}{r}\frac{d}{dr}D_R - iD_I - Np\frac{n}{r}\left[\omega_R - i\omega_I - \frac{nV_\theta}{r}\right]D_R - iD_I - \frac{n}{r}iD_R - D_I -$$

Therefore, the real part of the perturbation azimuthal momentum equation is:

$$\frac{1}{\mathrm{Re}}\tilde{\nabla}^2 B_R = -\left(\frac{dV_\theta}{dr} - \frac{V_\theta}{r}\right)A_R - \frac{1}{\mathrm{Re}}\frac{2n}{r^2}A_I - \left[\omega_I - Np\frac{1}{r}\left(\frac{dP}{dr}\right) - \frac{1}{r^2}\right]B_R - \left(\omega_R - n\frac{V_\theta}{r}\right)B_I$$

$$- Np\frac{V_\theta}{r}\frac{dD_R}{dr} - Np\frac{n}{r}\left(\omega_R - \frac{nV_\theta}{r}\right)D_R - \frac{n}{r}\tilde{1} - Np\omega_I\tilde{D}_I \quad (3.18)$$

and, after incorporating the steady-state solution,

$$\frac{1}{\mathrm{Re}}\tilde{\nabla}^2 B_R = \frac{4}{r^2\left(1-r^2\right)^2}A_R - \frac{1}{\mathrm{Re}}\frac{2n}{r^2}A_I - \left[\omega_I - \frac{4Np}{r\left(1-r^2\right)^2} - \frac{1}{r^2}\right]B_R - \left(\omega_R - \frac{2n}{r^2\left(1-r^2\right)}\right)B_I -$$

$$- Np\frac{n}{r}\left(\omega_R - \frac{2n}{r^2\left(1-r^2\right)}\right)D_R - \frac{2Np}{r^2\left(1-r^2\right)}\frac{dD_R}{dr} - \frac{n}{r}\tilde{1} - Np\cdot\omega_I\tilde{D}_I \quad (3.19)$$

The imaginary part of the azimuthal perturbation momentum equation is:

$$\frac{1}{\mathrm{Re}}\tilde{\nabla}^2 B_I = \frac{1}{\mathrm{Re}}\frac{2n}{r^2}A_R - \left(\frac{dV_\theta}{dr} - \frac{V_\theta}{r}\right)A_I - \left(\omega_R - n\frac{V_\theta}{r}\right)B_R - \left[\omega_I - Np\frac{1}{r}\left(\frac{dP}{dr}\right) - \frac{1}{r^2}\right]B_I$$

$$- \frac{n}{r}\tilde{1} - Np\cdot\omega_I\tilde{D}_R - Np\frac{n}{r}\left(\omega_R - \frac{nV_\theta}{r}\right)D_I - Np\frac{V_\theta}{r}\frac{dD_I}{dr} \quad (3.20)$$

After introducing the steady-state solution,

$$\frac{1}{\mathrm{Re}}\tilde{\nabla}^2 B_I = \frac{1}{\mathrm{Re}}\frac{2n}{r^2}A_R - \frac{4}{r^2\left(1-r^2\right)^2}A_I - \left(\omega_R - \frac{2n}{r^2\left(1-r^2\right)}\right)B_R - \left[\omega_I - \frac{4Np}{r\left(1-r^2\right)^2} - \frac{1}{r^2}\right]B_I -$$

$$- \frac{n}{r}\tilde{1} - Np\cdot\omega_I\tilde{D}_R - Np\frac{n}{r}\left(\omega_R - \frac{2n}{r^2\left(1-r^2\right)}\right)D_I - \frac{2Np}{r^2\left(1-r^2\right)}\frac{dD_I}{dr} \quad (3.21)$$

Perturbation Pressure equation

The pressure Equation (3.9) after substituting the perturbation expressions, factoring the exponential expression, and utilizing the differential operators, can be written:

$$\left(\frac{2n}{r}\frac{dV_\theta}{dr}\right)A+\left(\frac{2V_\theta}{r}\frac{dB}{dr}\right)+\left(\frac{2}{r}\frac{dV_\theta}{dr}\right)B=$$

$$iNp\frac{d^2\overline{P}}{dr^2}\frac{dA}{dr}+Np\left(\frac{d^3\overline{P}}{dr^3}+\frac{1}{r}\frac{d^2\overline{P}}{dr^2}\right)iA+\left[1+Np\left(i\omega_R-\omega_I\right)\right]\tilde{\nabla}^2D+$$

$$+iNp\frac{nV_\theta}{r}\tilde{\nabla}^2D+iNp\frac{n}{r}\frac{dV_\theta}{dr}\frac{dD}{dr}+inNp\left(+\frac{1}{r^2}\frac{dV_\theta}{dr}+\frac{V_\theta}{r^3}\right)D+iNp\frac{n}{r^2}\frac{d\overline{P}}{dr}B \qquad (3.22)$$

Writing the complex form of Equation (3.22) after re-arranging in term of the second derivatives of pressure amplitudes,

$$\left[1+Np\omega_I+iNp\left(\omega_R+n\frac{V_\theta}{r}\right)\right]\tilde{\nabla}^2D_R+iD_I=+Np\frac{d^2\overline{P}}{dr^2}\frac{d\left(iA_R+A_I\right)}{dr}+\left(\frac{2n}{r}\frac{dV_\theta}{dr}\right)A_R+iA_I+$$

$$Np\left(\frac{d^3\overline{P}}{dr^3}+\frac{1}{r}\frac{d^2\overline{P}}{dr^2}\right)iA_R+A_I+\left(\frac{2V_\theta}{r}\frac{d\left(B_R+iB_I\right)}{dr}\right)+\left(iNp\frac{n}{r^2}\frac{d\overline{P}}{dr}+\left(\frac{2}{r}\frac{dV_\theta}{dr}\right)\right)B_R+iB_I+$$

$$+Np\frac{n}{r}\frac{dV_\theta}{dr}\frac{d\left(iD_R+D_I\right)}{dr}+n\cdot Np\left[+\frac{1}{r^2}\frac{dV_\theta}{dr}+\frac{V_\theta}{r^3}\right]iD_R+D_I+ \qquad (3.23)$$

The real part of Equation (3.23) is,

$$\left[1+Np\omega_I\right]\tilde{\nabla}^2D_R+Np\left(\omega_R+n\frac{V_\theta}{r}\right)\tilde{\nabla}^2D_I=$$

$$+Np\frac{d^2\overline{P}}{dr^2}\frac{dA_I}{dr}+\left[\frac{2n}{r}\frac{dV_\theta}{dr}+Np\left(\frac{d^3\overline{P}}{dr^3}+\frac{1}{r}\frac{d^2\overline{P}}{dr^2}\right)\right]A_I+\left(\frac{2V_\theta}{r}\frac{dB_R}{dr}+\right.$$

$$\left.+\frac{2}{r}\frac{dV_\theta}{dr}B_R+Np\frac{n}{r^2}\frac{d\overline{P}}{dr}B_I+Np\frac{n}{r}\frac{dV_\theta}{dr}\frac{dD_I}{dr}+n\cdot Np\left(+\frac{1}{r^2}\frac{dV_\theta}{dr}+\frac{V_\theta}{r^3}\right)D_I\right. \qquad (3.24)$$

and the imaginary part is,

$$\square Np\left(\omega_R \square n\frac{V_\theta}{r}\right)\widetilde{\nabla}^2 D_R \square 1 \square Np\omega_I \widetilde{\nabla}^2 D_I =$$

$$\square Np\frac{d^2\overline{P}}{dr^2}\frac{dA_R}{dr} \square \left[\frac{2n}{r}\frac{dV_\theta}{dr} \square Np\left(\frac{d^3\overline{P}}{dr^3} \square \frac{1}{r}\frac{d^2\overline{P}}{dr^2}\right)\right]A_R \square Np\frac{n}{r^2}\frac{d\overline{P}}{dr}B_R \square \frac{2V_\theta}{r}\frac{dB_I}{\partial r} \square$$

$$\square \frac{2}{r}\frac{dV_\theta}{dr}B_I \square Np\frac{n}{r}\frac{dV_\theta}{dr}\frac{dD_R}{dr} \square n\cdot Np\left(\square \frac{1}{r^2}\frac{dV_\theta}{dr} \square \frac{V_\theta}{r^3}\right)D_R \qquad (3.25)$$

Utilizing the following functions,

$$c_1 = Np\left(\omega_R \square n\frac{V_\theta}{r}\right),\quad c_2 = \frac{2n}{r}\frac{dV_\theta}{dr} \square Np\left(\frac{d^3\overline{P}}{dr^3} \square \frac{1}{r}\frac{d^2\overline{P}}{dr^2}\right),\quad c_3 = Np\left[\square \frac{1}{r^2}\frac{dV_\theta}{dr} \square \frac{V_\theta}{r^3}\right],$$

and the constant $c_4 = 1 \square Np\omega_I$, to re-write equations (3·24) and (3·25), yields,

$$c_4\widetilde{\nabla}^2 D_R \square c_1\widetilde{\nabla}^2 D_I = \square Np\frac{d^2\overline{P}}{dr^2}\frac{dA_I}{dr} \square c_3 A_I \square$$

$$\frac{2V_\theta}{r}\frac{dB_R}{\partial r} \square \frac{2}{r}\frac{dV_\theta}{dr}B_R \square Np\frac{n}{r^2}\frac{d\overline{P}}{dr}B_I \square Np\frac{n}{r}\frac{dV_\theta}{dr}\frac{dD_I}{dr} \square c_2 nD_I \qquad (3.26)$$

$$\square c_1\widetilde{\nabla}^2 D_R \square c_4\widetilde{\nabla}^2 D_I = Np\frac{d^2\overline{P}}{dr^2}\frac{dA_R}{dr} \square c_3 A_R \square$$

$$\square \frac{2V_\theta}{r}\frac{dB_I}{\partial r} \square \frac{2}{r}\frac{dV_\theta}{dr}B_I \square Np\frac{n}{r^2}\frac{d\overline{P}}{dr}B_R \square Np\frac{n}{r}\frac{dV_\theta}{dr}\frac{dD_R}{dr} \square c_2 nD_R \qquad (3.27)$$

We can write a separate equation for each of the real and imaginary pressure functions D_R and D_I by solving equations (3·26) and (3·27) simultaneously, which results in the real and imaginary parts of pressure equation as follows:

$$\tilde{\nabla}^2 D_R =$$

$$\frac{c_4}{c_4^2 - c_1^2}\left(-Np\frac{d^2\bar{P}}{dr^2}\frac{dA_I}{dr} - c_3 A_I - \frac{2V_\theta}{r}\frac{dB_R}{dr} - \frac{2}{r}\frac{dV_\theta}{dr}B_R - Np\frac{n}{r^2}\frac{d\bar{P}}{dr}B_I - Np\frac{n}{r}\frac{dV_\theta}{dr}\frac{dD_I}{dr} - c_2 n D_I\right)$$

$$-\frac{c_1}{c_4^2 - c_1^2}\left(Np\frac{d^2\bar{P}}{dr^2}\frac{dA_R}{dr} - c_3 A_R - \frac{2V_\theta}{r}\frac{dB_I}{\partial r} - \frac{2}{r}\frac{dV_\theta}{dr}B_I - Np\frac{n}{r^2}\frac{d\bar{P}}{dr}B_R - Np\frac{n}{r}\frac{dV_\theta}{dr}\frac{dD_R}{dr} - c_2 n D_R\right)$$

(3.28)

$$\tilde{\nabla}^2 D_I =$$

$$\frac{c_1}{c_4^2 - c_1^2}\left(-Np\frac{d^2\bar{P}}{dr^2}\frac{dA_I}{dr} - c_3 A_I - \frac{2V_\theta}{r}\frac{dB_R}{\partial r} - \frac{2}{r}\frac{dV_\theta}{dr}B_R - Np\frac{n}{r^2}\frac{d\bar{P}}{dr}B_I - Np\frac{n}{r}\frac{dV_\theta}{dr}\frac{dD_I}{dr} - c_2 n D_I\right)$$

$$-\frac{c_4}{c_4^2 - c_1^2}\left(Np\frac{d^2\bar{P}}{dr^2}\frac{dA_R}{dr} - c_3 A_R - \frac{2V_\theta}{r}\frac{dB_I}{\partial r} - \frac{2}{r}\frac{dV_\theta}{dr}B_I - Np\frac{n}{r^2}\frac{d\bar{P}}{dr}B_R - Np\frac{n}{r}\frac{dV_\theta}{dr}\frac{dD_R}{dr} - c_2 n D_R\right)$$

(3.29)

And this is the end of the derivation of the linear perturbation equations in two dimensions, to summarize they are listed here again,

The conservation of radial momentum

$$\frac{1}{\mathrm{Re}}\tilde{\nabla}^2 A_R = -\left(\omega_I - 2\frac{V_\theta}{r} - n\frac{V_\theta}{r} - Np\frac{d^2 P}{dr^2}\right)A_R - \omega_R A_I - \frac{1}{\mathrm{Re}}\frac{2n}{r^2}B_R$$

$$-n\cdot Np\frac{V_\theta}{r^2}D_R - Np\left(\omega_R - n\frac{V_\theta}{r}\right)\frac{dD_R}{dr} - 1 - Np\cdot\omega_I - \frac{dD_I}{dr} \quad (3.14)$$

$$\frac{1}{\mathrm{Re}}\tilde{\nabla}^2 A_I = \omega_R A_R - \left[\omega_I - 2 - n\frac{V_\theta}{r} - Np\frac{d^2 P}{dr^2}\right]A_I - \frac{1}{\mathrm{Re}}\frac{2n}{r^2}B_I$$

$$-Np\cdot\omega_I - 1 - \frac{dD_R}{dr} - n\cdot Np\frac{V_\theta}{r^2}D_I - Np\left(\omega_R - n\frac{V_\theta}{r}\right)\frac{dD_I}{dr} \quad (3.16)$$

The conservation of azimuthal momentum

$$\frac{1}{\mathrm{Re}}\tilde{\nabla}^2 B_R = -\left(\frac{dV_\theta}{dr} - \frac{V_\theta}{r}\right)A_R - \frac{1}{\mathrm{Re}}\frac{2n}{r^2}A_I - \left[\omega_I - Np\frac{1}{r}\left(\frac{dP}{dr}\right) - \frac{1}{r^2}\right]B_R - \left(\omega_R - n\frac{V_\theta}{r}\right)B_I$$

$$- Np\left[-\frac{n}{r}\omega_R - \frac{n^2 V_\theta}{r^2} - \frac{V_\theta}{r}\frac{\partial}{\partial r}\right]D_R - Np\frac{n}{r}\omega_I D_I - \frac{n}{r}D_I \quad (3.18)$$

$$\frac{1}{\mathrm{Re}}\tilde{\nabla}^2 B_I = \frac{1}{\mathrm{Re}}\frac{2n}{r^2}A_R - \left(\frac{dV_\theta}{dr} - \frac{V_\theta}{r}\right)A_I - \left(\omega_R - n\frac{V_\theta}{r}\right)B_R - \left[\omega_I - Np\frac{1}{r}\left(\frac{dP}{dr}\right) - \frac{1}{r^2}\right]B_I$$

$$-\frac{n}{r}\left[1 - Np\cdot\omega_I\right]D_R - Np\frac{n}{r}\left(\omega_R - \frac{nV_\theta}{r}\right)D_I - Np\frac{V_\theta}{r}\frac{\partial D_I}{\partial r} \quad (3.20)$$

The pressure equations

$$\tilde{\nabla}^2 D_R =$$

$$\frac{c_4}{c_4^2 - c_1^2}\left(-Np\frac{d^2\bar{P}}{dr^2}\frac{dA_I}{dr} - c_3 A_I - \frac{2V_\theta}{r}\frac{dB_R}{dr} - \frac{2}{r}\frac{dV_\theta}{dr}B_R - Np\frac{n}{r^2}\frac{d\bar{P}}{dr}B_I - Np\frac{n}{r}\frac{dV_\theta}{dr}\frac{dD_I}{dr} - c_2 n D_I\right)$$

$$-\frac{c_1}{c_4^2 - c_1^2}\left(Np\frac{d^2\bar{P}}{dr^2}\frac{dA_R}{dr} - c_3 A_R - \frac{2V_\theta}{r}\frac{dB_I}{\partial r} - \frac{2}{r}\frac{dV_\theta}{dr}B_I - Np\frac{n}{r^2}\frac{d\bar{P}}{dr}B_R - Np\frac{n}{r}\frac{dV_\theta}{dr}\frac{dD_R}{dr} - c_2 n D_R\right)$$

(3.28)

$$\tilde{\nabla}^2 D_I =$$

$$\frac{c_1}{c_4^2 - c_1^2}\left(-Np\frac{d^2\bar{P}}{dr^2}\frac{dA_I}{dr} - c_3 A_I - \frac{2V_\theta}{r}\frac{dB_R}{\partial r} - \frac{2}{r}\frac{dV_\theta}{dr}B_R - Np\frac{n}{r^2}\frac{d\bar{P}}{dr}B_I - Np\frac{n}{r}\frac{dV_\theta}{dr}\frac{dD_I}{dr} - c_2 n D_I\right)$$

$$-\frac{c_4}{c_4^2 - c_1^2}\left(Np\frac{d^2\bar{P}}{dr^2}\frac{dA_R}{dr} - c_3 A_R - \frac{2V_\theta}{r}\frac{dB_I}{\partial r} - \frac{2}{r}\frac{dV_\theta}{dr}B_I - Np\frac{n}{r^2}\frac{d\bar{P}}{dr}B_R - Np\frac{n}{r}\frac{dV_\theta}{dr}\frac{dD_R}{dr} - c_2 n D_R\right)$$

(3.29)

These are six equations in the dependent variables of the vortical flow system which are the real and imaginary parts of the functions (A, B, D) for the radial velocity perturbation, azimuthal velocity perturbation and pressure perturbations respectively. In the next section

the non-linear problem will be developed, before proceeding to the state-variable model for the linear part of this study.

3.6 Non-linear consideration

In the previous formulation, the non-linear terms (or quadratic terms) were neglected; those terms are considered here in order to evaluate the degree to which the linear system solution approaches an exact, finite amplitude solution for a two-dimensional flow representation of this type of axial vortex.

The state-variable model continues to serve as a powerful tool and has been utilized to develop a non-linear system model. Utilizing useful functions in Matlab® to define complex variables like "complex, real, imag, abs", it was possible to separate the representation into real and imaginary parts for the stability analysis without requiring excessive algebraic manipulations.

The derivation of the non-linear problem starts from the basic governing equations for the flow which becomes (excluding steady terms),

Conservation of radial momentum Equation (3.4)

$$\frac{\partial v_r'}{\partial t} + v_r'\frac{\partial v_r'}{\partial r} + \frac{V_\theta + v_\theta'}{r}\frac{\partial v_r'}{\partial \theta} + \frac{2V_\theta v_\theta' + v_\theta'^2}{r} = \frac{1}{\mathrm{Re}}\left\{\frac{\partial}{\partial r}\left[\frac{1}{r}\frac{\partial}{\partial r}\left(r v_r'\right)\right] + \frac{1}{r^2}\frac{\partial^2 v_r'}{\partial \theta^2} + \frac{2}{r^2}\frac{\partial v_\theta'}{\partial \theta}\right\} +$$

$$+ Np\left[\frac{\partial^2 p'}{\partial t \partial r} + v_r'\frac{\partial^2 \bar{P} + p'}{\partial r^2} + \frac{V_\theta + v_\theta'}{r}\frac{\partial^2 p'}{\partial \theta \partial r} + \frac{V_\theta + v_\theta'}{r^2}\left(\frac{\partial p'}{\partial \theta}\right)\right] = \frac{\partial p'}{\partial r} \qquad (3.30)$$

The perturbation conservation of azimuthal momentum equation becomes:

$$\frac{\partial v_\theta'}{\partial t} + v_r'\frac{\partial V_\theta + v_\theta'}{\partial r} + \frac{V_\theta + v_\theta'}{r}\frac{\partial v_\theta'}{\partial \theta} + \frac{v_r'(V_\theta + v_\theta')}{r} = \frac{1}{\mathrm{Re}}\left\{\frac{\partial}{\partial r}\left[\frac{1}{r}\frac{\partial}{\partial r}(rv_\theta')\right] + \frac{1}{r^2}\frac{\partial^2 v_\theta'}{\partial \theta^2} + \frac{2}{r^2}\frac{\partial v_r'}{\partial \theta}\right\} +$$

$$+ Np\left[\frac{1}{r}\frac{\partial^2 p'}{\partial t \partial \theta} + \frac{v_r'}{r}\frac{\partial^2 p'}{\partial r \partial \theta} + \frac{V_\theta + v_\theta'}{r^2}\frac{\partial^2 p'}{\partial \theta^2} + \frac{V_\theta}{r}\frac{\partial p'}{\partial r} + \frac{v_\theta'}{r}\left(\frac{\partial \bar{P} + p'}{\partial r}\right) + \frac{v_r'}{r^2}\left(\frac{\partial p'}{\partial \theta}\right)\right] + \frac{1}{r}\frac{\partial p'}{\partial \theta}$$

(3.31)

and the non-linear form of the pressure equation can be derived as follows,

$$\nabla \cdot \frac{D\mathbf{v}}{Dt} = \nabla \cdot [\bar{\mathbf{v}} \cdot \nabla \mathbf{v}] = \left(1 + Np\frac{\partial}{\partial t}\right)\nabla^2 P + Np\nabla \cdot [\bar{\mathbf{v}} \cdot \nabla \bar{\nabla} P].$$

Term-by-term expansions are as follows:

$$\nabla \cdot [\bar{\mathbf{v}} \cdot \nabla \mathbf{v}] = \left[\left(\frac{\partial v_r}{\partial r}\right)^2 + \frac{1}{r^2}\left(\frac{\partial v_\theta}{\partial \theta}\right)^2 + \frac{v_r}{r^2}\frac{\partial v_\theta}{\partial \theta} + \frac{v_r}{r}\frac{\partial v_r}{\partial r}\right] +$$

$$2\frac{\partial v_r}{\partial \theta}\frac{\partial}{\partial r}\left(\frac{v_\theta}{r}\right) + 2v_\theta\frac{\partial}{\partial r}\left(\frac{v_\theta}{r}\right) + 2\frac{v_\theta}{r^2}\frac{\partial v_r}{\partial \theta} + 2\frac{v_\theta^2}{r^2}$$

and,

$$\left(1 + Np\frac{\partial}{\partial t}\right)\nabla^2 P + \bar{\nabla} \cdot [\bar{\mathbf{v}} \cdot \bar{\nabla}\bar{\nabla} P] =$$

$$\left(1 + Np\frac{\partial}{\partial t}\right)\left[\frac{1}{r}\frac{\partial}{\partial r}\left(r\frac{\partial P}{\partial r}\right) + \frac{1}{r^2}\frac{\partial^2 P}{\partial \theta^2}\right] + \frac{Np}{r}\frac{\partial}{\partial r}\left\{r\left[v_r\frac{\partial^2 P}{\partial r^2} + \frac{v_\theta}{r}\frac{\partial^2 P}{\partial r \partial \theta} + \frac{v_\theta}{r^2}\left(\frac{\partial P}{\partial \theta}\right)\right]\right\}$$

$$+ \frac{Np}{r}\frac{\partial}{\partial \theta}\left[\frac{v_r}{r}\frac{\partial^2 P}{\partial r \partial \theta} + \frac{v_\theta}{r^2}\frac{\partial^2 P}{\partial \theta^2} + \frac{v_r}{r^2}\left(\frac{\partial P}{\partial \theta}\right) + \frac{v_\theta}{r}\left(\frac{\partial P}{\partial r}\right)\right].$$

Substitution into the pressure Equation (3.28) yields,

$$\left[\left(\frac{\partial v_r}{\partial r}\right)^2 \square \frac{1}{r^2}\left(\frac{\partial v_\theta}{\partial \theta}\right)^2 \square \frac{v_r}{r^2}\frac{\partial v_\theta}{\partial \theta} \square \frac{v_r}{r}\frac{\partial v_r}{\partial r}\right] \square 2\frac{\partial v_r}{\partial \theta}\frac{\partial}{\partial r}\left(\frac{v_\theta}{r}\right) \square 2v_\theta \frac{\partial}{\partial r}\left(\frac{v_\theta}{r}\right) \square 2\frac{v_\theta}{r^2}\frac{\partial v_r}{\partial \theta} \square 2\frac{v_\theta^2}{r^2} =$$

$$\left(\square 1 \square Np\frac{\partial}{\partial t}\right)\left[\frac{1}{r}\frac{\partial}{\partial r}\left(r\frac{\partial P}{\partial r}\right) \square \frac{1}{r^2}\frac{\partial^2 P}{\partial \theta^2}\right] \square \frac{Np}{r}\frac{\partial}{\partial r}\left\{r\left[v_r\frac{\partial^2 P}{\partial r^2} \square \frac{v_\theta}{r}\frac{\partial^2 P}{\partial r \partial \theta} \square \frac{v_\theta}{r^2}\left(\frac{\partial P}{\partial \theta}\right)\right]\right\}$$

$$\square \frac{Np}{r}\frac{\partial}{\partial \theta}\left[\frac{v_r}{r}\frac{\partial^2 P}{\partial r \partial \theta} \square \frac{v_\theta}{r^2}\frac{\partial^2 P}{\partial \theta^2} \square \frac{v_r}{r^2}\left(\frac{\partial P}{\partial \theta}\right) \square \frac{v_\theta}{r}\left(\frac{\partial P}{\partial r}\right)\right] \quad (3.32)$$

Utilizing the perturbation expressions from Equation (3.1), and removing the steady-state solution,

$$\left[\left(\frac{\partial v_r'}{\partial r}\right)^2 \square \frac{1}{r^2}\left(\frac{\partial v_\theta'}{\partial \theta}\right)^2 \square \frac{v_r'}{r^2}\frac{\partial v_\theta'}{\partial \theta} \square \frac{v_r'}{r}\frac{\partial v_r'}{\partial r}\right] \square 2\frac{\partial v_r'}{\partial \theta}\frac{\partial}{\partial r}\left(\frac{V_\theta \square v_\theta'}{r}\right) =$$

$$\square 2V_\theta \frac{\partial}{\partial r}\left(\frac{v_\theta'}{r}\right) \square 2v_\theta' \frac{\partial}{\partial r}\left(\frac{V_\theta \square v_\theta'}{r}\right) \square 2\frac{V_\theta \square v_\theta'}{r^2}\frac{\partial v_r'}{\partial \theta} \square \frac{4V_\theta v_\theta' \square 2v_\theta'^2}{r^2}$$

$$\square Np\frac{1}{r}\frac{\partial}{\partial \theta}\left[\frac{v_r'}{r}\frac{\partial^2 p'}{\partial r \partial \theta} \square \frac{V_\theta \square v_\theta'}{r^2}\frac{\partial^2 p'}{\partial \theta^2} \square \frac{v_r'}{r^2}\left(\frac{\partial p'}{\partial \theta}\right) \square \frac{V_\theta \square v_\theta'}{r}\left(\frac{\partial \overline{P} \square p'}{\partial r}\right)\right]$$

$$\square\left[\frac{1}{r}\frac{\partial}{\partial r}\left(r\frac{\partial p'}{\partial r}\right) \square \frac{1}{r^2}\frac{\partial^2 p'}{\partial \theta^2}\right] \square Np\frac{\partial}{\partial t}\left[\frac{1}{r}\frac{\partial}{\partial r}\left(r\frac{\partial \overline{P} \square p'}{\partial r}\right) \square \frac{1}{r^2}\frac{\partial^2 p'}{\partial \theta^2}\right] \square$$

$$\square Np\frac{1}{r}\frac{\partial}{\partial r}\left\{r\left[v_r'\frac{\partial^2 \overline{P} \square p'}{\partial r^2} \square \frac{V_\theta \square v_\theta'}{r}\frac{\partial^2 p'}{\partial r \partial \theta} \square \frac{V_\theta \square v_\theta'}{r^2}\left(\frac{\partial p'}{\partial \theta}\right)\right]\right\} \quad (3.33)$$

Using the same perturbation functional form as Equation (3.10) and the differential operators, we can write the equations in terms of the perturbation functions *A,B* and *D*.

The radial momentum of perturbation

From Equation (3.30)

$$i\omega A \square n\frac{V_\theta}{r}A \square \frac{2V_\theta}{r}B =$$

$$\frac{i}{\mathrm{Re}}\left\{\frac{d^2A}{dr^2} \square \frac{1}{r}\frac{dA}{dr} \square \frac{n^2}{r^2}A \square \frac{2n}{r^2}B\right\} \square iNp\left[\omega\frac{dD}{dr} \square n\frac{V_\theta}{r}\frac{dD}{dr} \square n\frac{V_\theta}{r^2}D \square A\frac{d^2\overline{P}}{dr^2}\right] \square \frac{dD}{dr}$$

$$\square e^{i(\omega t \square n\theta)}\left[\left(A\frac{dA}{dr} \square \frac{n}{r}AB \square \frac{B^2}{r}\right) \square iNp\left(A\frac{d^2D}{dr^2} \square n\frac{B}{r}\frac{dD}{dr} \square \frac{n}{r^2}DB\right)\right]$$

Here the higher derivative of the radial velocity perturbation amplitude is the second derivative ($\frac{d^2A}{dr^2}$) which is the same order as the linear system Equations (3.14 and 3.16).

Next, the quadratic terms involving the second pressure derivative $A\frac{d^2D}{dr^2}$ and the like are considered to be negligibly small in comparison with other non-linear terms. Dropping that term from the radial momentum equation leaves,

$$i\omega A \square n\frac{V_\theta}{r}A \square \frac{2V_\theta}{r}B = \frac{i}{\mathrm{Re}}\left\{\frac{d^2A}{dr^2} \square \frac{1}{r}\frac{dA}{dr} \square \frac{n^2}{r^2}A \square \frac{2n}{r^2}B\right\} \square$$

$$\square iNp\left[\omega\frac{dD}{dr} \square n\frac{V_\theta}{r}\frac{dD}{dr} \square n\frac{V_\theta}{r^2}D \square A\frac{d^2\overline{P}}{dr^2}\right] \square \frac{dD}{dr} \square$$

$$\square e^{i(\omega t \square n\theta)}\left[\left(A\frac{dA}{dr} \square \frac{n}{r}AB \square \frac{B^2}{r}\right) \square iNp\left(n\frac{B}{r}\frac{dD}{dr} \square \frac{n}{r^2}DB\right)\right] \qquad (3.34)$$

The azimuthal momentum of perturbations

$$i\omega B \square iA\frac{dV_\theta}{dr} \square in\frac{V_\theta}{r}B \square \frac{V_\theta}{r}A = \frac{1}{\mathrm{Re}}\left\{\frac{d^2B}{dr^2} \square \frac{1}{r}\frac{dB}{dr} \square \frac{n^2}{r^2}B \square n\frac{2}{r^2}A\right\} \square$$

$$\square Np\left[in\frac{\omega}{r}D \square \frac{n^2V_\theta}{r^2}D \square \frac{V_\theta}{r}\frac{dD}{dr} \square \frac{B}{r}\frac{d\overline{P}}{dr}\right] \square i\frac{n}{r}D$$

$$\square e^{i(\omega t \square n\theta)}\left[Np\left(\square n\frac{A}{r}\frac{dD}{dr} \square \frac{n^2}{r^2}BD \square \frac{B}{r}\frac{dD}{dr} \square n\frac{A}{r^2}D\right) \square \left(iA\frac{dB}{dr} \square in\frac{B^2}{r} \square i\frac{AB}{r}\right)\right] \qquad (3.35)$$

The highest derivative of the azimuthal velocity perturbation amplitude is the second derivative ($\frac{d^2B}{dr^2}$) which is consistent with the linear system Equations (3.18 and 3.20).

The pressure equation (3.33),

$$-\frac{2n}{r}\frac{dV_\theta}{dr}A-\frac{2V_\theta}{r}\frac{dB}{\partial r}-\frac{2}{r}\frac{dV_\theta}{dr}B=Np\left(\frac{d^2\overline{P}}{dr^2}\frac{d}{dr}-\frac{d^3\overline{P}}{dr^3}-\frac{1}{r}\frac{d^2\overline{P}}{dr^2}\right)iA-$$

$$\left[-1-iNp\omega\right]\tilde{\nabla}^2D-Np\left[\frac{V_\theta}{r}\tilde{\nabla}^2-\frac{1}{r}\frac{dV_\theta}{dr}\frac{d}{dr}-\frac{1}{r^2}\frac{dV_\theta}{dr}-\frac{V_\theta}{r^3}\right]inD-iNp\frac{n}{r^2}\frac{d\overline{P}}{dr}B$$

$$-e^{i\omega t-in\theta}\left[\left(\frac{dA}{dr}\right)^2-\frac{n^2}{r^2}B^2-\frac{n}{r^2}AB-\frac{A}{r}\frac{dA}{dr}-\frac{2n}{r}A\frac{dB}{dr}-\frac{2}{r}B\frac{dB}{dr}\right]$$

$$-ie^{i\omega t-in\theta}Np\left[\frac{d}{dr}\left(A\frac{d^2D}{dr^2}-\frac{n}{r}B\frac{dD}{dr}\right)-\frac{A}{r}\frac{d^2D}{dr^2}-\frac{2n}{r^2}B\frac{dD}{dr}-\frac{n}{r^2}D\frac{dB}{dr}-\left(\frac{n}{r^3}-\frac{2n^3}{r^3}\right)BD-\frac{2n^2}{r^2}A\frac{dD}{dr}-\frac{2n^2}{r^3}AD\right] \tag{3.36}$$

After dropping the quadratic term with the second pressure derivative and higher derivatives,

$$-\frac{2n}{r}\frac{dV_\theta}{dr}A-\frac{2V_\theta}{r}\frac{dB}{\partial r}-\frac{2}{r}\frac{dV_\theta}{dr}B=Np\left(\frac{d^2\overline{P}}{dr^2}\frac{d}{dr}-\frac{d^3\overline{P}}{dr^3}-\frac{1}{r}\frac{d^2\overline{P}}{dr^2}\right)iA-\left[-1-iNp\omega\right]\tilde{\nabla}^2D-$$

$$-Np\left[\frac{V_\theta}{r}\tilde{\nabla}^2-\frac{1}{r}\frac{dV_\theta}{dr}\frac{d}{dr}-\frac{1}{r^2}\frac{dV_\theta}{dr}-\frac{V_\theta}{r^3}\right]inD-iNp\frac{n}{r^2}\frac{d\overline{P}}{dr}B-$$

$$-e^{i\omega t-in\theta}\left[\left(\frac{dA}{dr}\right)^2-\frac{n^2}{r^2}B^2-\frac{n}{r^2}AB-\frac{A}{r}\frac{dA}{dr}-\frac{2n}{r}A\frac{dB}{dr}-\frac{2}{r}B\frac{dB}{dr}\right]$$

$$-ie^{i\omega t-in\theta}Np\left[\frac{2n}{r^2}B\frac{dD}{dr}-\frac{n}{r^2}D\frac{dB}{dr}-\left(\frac{n}{r^3}-\frac{2n^3}{r^3}\right)BD-\frac{2n^2}{r^2}A\frac{dD}{dr}-\frac{2n^2}{r^3}AD\right] \tag{3.37}$$

3.7 Summary

In this chapter the perturbation governing equations have been derived in two dimensions, along with the linear and non-linear stability equations assuming periodic perturbations. Next, the state-variable model will be developed for both the linear and non-linear problems.

CHAPTER 4

STATE-VARIABLE NUMERICAL MODEL

The next steps in developing the state variable model is to assume the number of state variables needed to define the linear system equations (3.14), (3.16), (3.18), (3.20), (3.28), and (3.29) as well as the non-linear system equations (3.34), (3.35), and (3.37). Each state variable should appear at least once in the set of equations and should have a separate equation defining its derivative.

4.1 Linear system state-variable model

The state variables of the linear system for perturbed axial vortex flow equations [(3.14), (3.16), (3.18), (3.20), (3.28), and (3.29)] contains 12 state variables representing the velocity and pressure fields and their respective first derivatives with respect to the radial direction (r). The state variables are listed in the table below:

$\frac{dA_R}{dr} \rightarrow \chi_1$	$A_R \rightarrow \chi_2$
$\frac{dA_I}{dr} \rightarrow \chi_3$	$A_I \rightarrow \chi_4$
$\frac{dB_R}{dr} \rightarrow \chi_5$	$B_R \rightarrow \chi_6$
$\frac{dB_I}{dr} \rightarrow \chi_7$	$B_I \rightarrow \chi_8$
$\frac{dD_R}{dr} \rightarrow \chi_9$	$D_R \rightarrow \chi_{10}$
$\frac{dD_I}{dr} \rightarrow \chi_{11}$	$D_I \rightarrow \chi_{12}$

Table 4.1 State variables of the linear system for axial vortex flow

4.1.1 State equations for linear system

The state equations for the linear system are the same governing equations (3.14), (3.16), (3.18), (3.20), (3.28), and (3.29) after replacing the derivatives and functions with their state variable names. The following system of equations resulted:

The conservation of radial momentum

Equations (3.14) and (3·16) become,

$$\frac{d\chi_1}{dr} = -\frac{1}{r}\chi_1 - \left\{\frac{n^2}{r^2} - \mathrm{Re}\cdot\left[\omega_I - 2n\frac{V_\theta}{r} - Np\frac{d^2P}{dr^2}\right]\right\}\chi_2 - \mathrm{Re}\cdot\omega_R\chi_4 -$$

$$-\frac{2n}{r^2}\chi_6 - n\cdot\mathrm{Re}\cdot Np\frac{V_\theta}{r^2}\chi_{10} - \mathrm{Re}\cdot Np\left(\omega_R - n\frac{V_\theta}{r}\right)\chi_9 - \mathrm{Re}\cdot 1 - Np\cdot\omega_I\chi_{11} \quad (4.1)$$

$$\frac{d\chi_2}{dr} = \chi_1 \quad (4.2)$$

$$\frac{d\chi_3}{dr} = \mathrm{Re}\cdot\omega_R\chi_2 - \frac{1}{r}\chi_3 - \left\{\frac{n^2}{r^2} - \mathrm{Re}\cdot\left[\omega_I - 2n\frac{V_\theta}{r} - Np\frac{d^2P}{dr^2}\right]\right\}\chi_4 - \frac{2n}{r^2}\chi_8 -$$

$$-\mathrm{Re}\cdot Np\cdot\omega_I - 1\chi_9 - n\cdot\mathrm{Re}\cdot Np\frac{V_\theta}{r^2}\chi_{12} - \mathrm{Re}\cdot Np\left(\omega_R - n\frac{V_\theta}{r}\right)\chi_{11} \quad (4.3)$$

$$\frac{d\chi_4}{dr} = \chi_3 \quad (4.4)$$

The conservation of azimuthal momentum becomes,

$$\frac{d\chi_5}{dr} = -\mathrm{Re}\cdot\left(\frac{dV_\theta}{dr} - \frac{V_\theta}{r}\right)\chi_2 - \frac{2n}{r^2}\chi_4 - \frac{1}{r}\chi_5 - \left\{\frac{n^2}{r^2} - \mathrm{Re}\cdot\left[\omega_I - Np\frac{1}{r}\left(\frac{dP}{dr}\right) - \frac{1}{r^2}\right]\right\}\chi_6$$

$$-\mathrm{Re}\cdot\left(\omega_R - n\frac{V_\theta}{r}\right)\chi_8 - \mathrm{Re}\cdot Np\frac{V_\theta}{r}\chi_9 - \mathrm{Re}\cdot Np\cdot\frac{n}{r}\left(\omega_R - \frac{nV_\theta}{r}\right)\chi_{10} - \mathrm{Re}\cdot\frac{n}{r} - Np\omega_I - 1\chi_{12} \quad (4.5)$$

$$\frac{d\chi_6}{dr} = \chi_5 \quad (4.6)$$

$$\frac{d\chi_7}{dr} = \frac{2n}{r^2}\chi_2 - \mathrm{Re}\cdot\left(\frac{dV_\theta}{dr} - \frac{V_\theta}{r}\right)\chi_4 - \mathrm{Re}\cdot\left(\omega_R - n\frac{V_\theta}{r}\right)\chi_6 - \frac{1}{r}\chi_7 -$$

$$\left\{\frac{n^2}{r^2} - \mathrm{Re}\cdot\left[\omega_I - Np\frac{1}{r}\left(\frac{dP}{dr}\right) - \frac{1}{r^2}\right]\right\}\chi_8 - \mathrm{Re}\cdot\frac{n}{r}\bar{1} - Np\cdot\omega_I\chi_{10}$$

$$- \mathrm{Re}\cdot Np\frac{n}{r}\left(\omega_R - \frac{nV_\theta}{r}\right)\chi_{12} - \mathrm{Re}\cdot Np\frac{V_\theta}{r}\chi_{11} \quad (4.7)$$

$$\frac{d\chi_8}{dr} = \chi_7 \quad (4.8)$$

The pressure equation becomes,

$$\frac{d\chi_9}{dr} =$$

$$\frac{c_4}{c_4^2 - c_1^2}\left(-Np\frac{d^2\bar{P}}{dr^2}\chi_3 - c_3\chi_4 - \frac{2V_\theta}{r}\chi_5 - \frac{2}{r}\frac{dV_\theta}{dr}\chi_6 - Np\frac{n}{r^2}\frac{d\bar{P}}{dr}\chi_8 - Np\frac{n}{r}\frac{dV_\theta}{dr}\chi_{11} - c_2n\chi_{12}\right)$$

$$- \frac{c_1}{c_4^2 - c_1^2}\left(Np\frac{d^2\bar{P}}{dr^2}\chi_1 - c_3\chi_2 - \frac{2V_\theta}{r}\chi_7 - \frac{2}{r}\frac{dV_\theta}{dr}\chi_8 - Np\frac{n}{r^2}\frac{d\bar{P}}{dr}\chi_6\right) -$$

$$- \left[Np\frac{n}{r}\frac{c_1}{c_4^2 - c_1^2}\frac{dV_\theta}{dr} - \frac{1}{r}\right]\chi_9 - \left[\frac{n^2}{r^2} - \frac{n\cdot c_2c_1}{c_4^2 - c_1^2}\right]\chi_{10} \quad (4.9)$$

$$\frac{d\chi_{10}}{dr} = \chi_9 \quad (4.10)$$

$$\frac{d\chi_{11}}{dr} = \frac{c_1}{c_4^2 - c_1^2}\left(-Np\frac{d^2\bar{P}}{dr^2}\chi_3 - c_3\chi_4 - \frac{2V_\theta}{r}\chi_5 - \frac{2}{r}\frac{dV_\theta}{dr}\chi_6 - Np\frac{n}{r^2}\frac{d\bar{P}}{dr}\chi_8\right)$$

$$- \frac{c_4}{c_4^2 - c_1^2}\left(Np\frac{d^2\bar{P}}{dr^2}\chi_1 - c_3\chi_2 - \frac{2V_\theta}{r}\chi_7 - \frac{2}{r}\frac{dV_\theta}{dr}\chi_8 - Np\frac{n}{r^2}\frac{d\bar{P}}{dr}\chi_6 - Np\frac{n}{r}\frac{dV_\theta}{dr}\chi_9 - c_2n\chi_{10}\right) -$$

$$- \left[Np\frac{n}{r}\frac{c_1}{c_4^2 - c_1^2}\frac{dV_\theta}{dr} - \frac{1}{r}\right]\chi_{11} - \left[\frac{n^2}{r^2} - \frac{n\cdot c_2c_1}{c_4^2 - c_1^2}\right]\chi_{12} \quad (4.11)$$

$$\frac{d\chi_{12}}{dr} = \chi_{11} \tag{4.12}$$

The state equations (4·1) to (4.12) are first order differential equations in the state variables, a property of the state variable model that allows representing the axial vortex system with easily integrated equations. Also, the independent variables of integration will be the 12- state variables and the radial coordinate is of course used as a stepping variable.

4.1.2 Fundamental Interpretation of State Variable Model Parameters

The state variable input parameters are characteristic *Reynolds number (Re)* and the new *non-equilibrium swirl parameter (Np)* employed to fully-characterize the unperturbed axial vortex state. Additional unsteady input parameters are the circular frequency of the imposed perturbations, ω_R, and a mode number, n, specifying the azimuthal modes. Finally, a damping parameter, ω_I, is employed to describe the transient growth of the perturbations. The state variable model will use ω_I to find the converged solution according to the prescribed magnitude of the perturbations in the flow. It also determines whether the perturbation mode is going to grow in the flow or not.

For the present axial vortex case, it is important to recognize that the two flow parameters *Re* and *Np* can be related theoretically through their definitions:

$$\mathrm{Re}\cdot Np = \frac{r_c V_{\theta,\max}}{\nu_{air}} \cdot \frac{\eta_{P,air} V_{\theta,\max}}{r_c} = \frac{\eta_{P,air} V_{\theta,\max}^2}{\nu_{air}}, \tag{4.13}$$

From Equation (3.1), the theoretically-based maximum azimuthal velocity is $V_{\theta,\max} = \sqrt{\frac{2\nu_{air}}{\eta_{P.air}}}$. Consequently,

$$\mathrm{Re}\cdot Np = 2 \tag{4.14}$$

Since the relationship between the Reynolds number and the non-equilibrium swirl parameter assumes that the experimentally-generated axial vortex is identical with the theoretical vortex, it is necessary to examine the actual experimentally-measured product against equation (4.14) Based on theoretical predictions (Ash and Zuckerwar, 2006) the pressure relaxation coefficient for air varies with temperature and relative humidity, but pressure relaxation coefficients for air have not yet been validated experimentally. Furthermore, the accuracy of the measured wind tunnel air temperature and relative humidity during each experimental run is uncertain. The calculated value of the Reynolds number-non-equilibrium swirl parameter product for the ten reference cases summarized in Table 1.1, along with additional measurements from Ely (2013) have been plotted in Figure 5.1. Virtually all of the experimental values are scattered below the theoretical value of two.

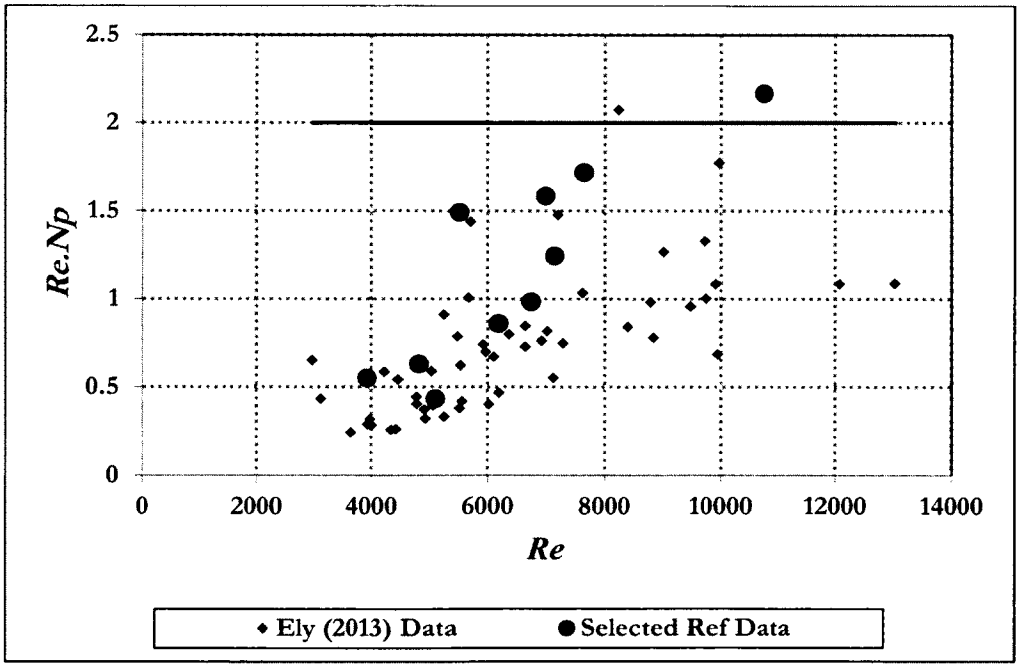

Figure 4.1 The values of *Re·Np* at different levels of *Re* (Ely, 2013)

Finally, the parameters, n, ω_R, and ω_I, can be related utilizing an important stability theorem from Schlichting (1968), stating that the speed of propagation of neutral perturbations (ω_I =0) for boundary layer flows must be smaller than the maximum velocity of the mean flow, i.e.

$$\omega_R < n\frac{V_{\max}}{r_c} \quad . \tag{4.15}$$

If inequality (4·14) is written in dimensionless form, it translates to the requirement that:

$$\omega_R < n \quad . \tag{4.16}$$

Thus, the five paramters of the state variable model will be (Re, Np, ω_R, ω_I and n.). Figure (4.2) represents the five parameters and the related processes used to evaluate them. The state variable model utilizes the parameters Re and Np obtained from the steady state runs employing the wind tunnel.

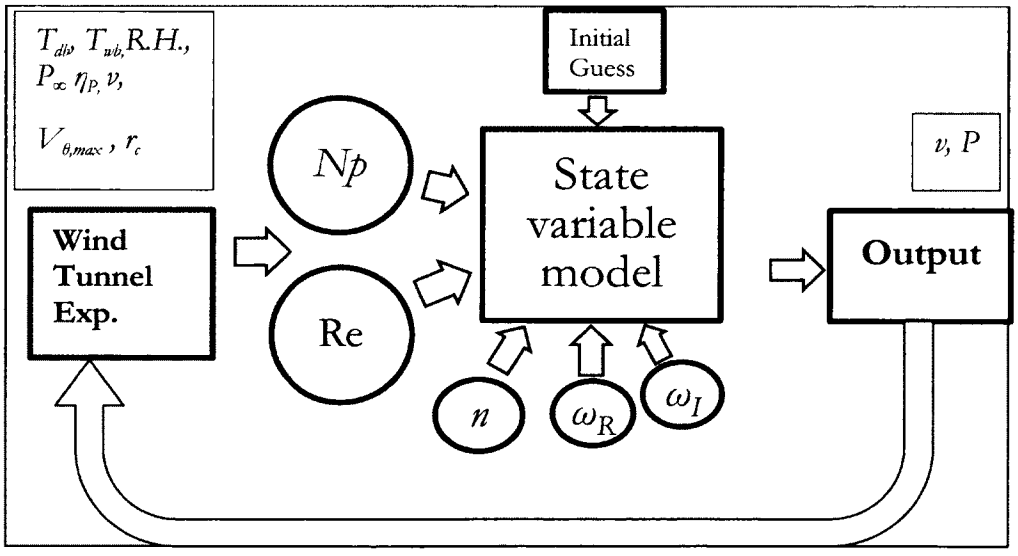

Figure 4.2 Schematic of state variable model input and output parameters

4.1.3 Numerical integration of state-vector

The next step in developing the state-variable model was to integrate the state vector containing all the state variables. An initial guess was supplied to the state vector in the form of an external disturbance, and then the Runge-Kutta method was employed to carry out the integration from the first point. All the state equations were integrated simultaneously in order to proceed to the next spatial step.

4.2 The non-linear state-variable model

The non-linear system of equations derived in Chapter 3 [equations (3.34),(3.35), and (3.37)] require the same set of state variables used for the linear system (listed in Table 4.1).

4.2.1 State equations for non-linear system

The state equations for each of these state variables are derived as follows:

First writing the definition of the perturbation amplitudes in terms of the new state-variables as:

$$A = \chi_2 \pm i\chi_4\,,\ B = \chi_6 \pm i\chi_8 \text{ and } D = \chi_{10} \pm i\chi_{12}\,.$$

Now, Equation (3.36) can be re-written as follows,

$$\frac{1}{\mathrm{Re}}\frac{d^2A}{dr^2} =$$

$$\mp \omega A \mp in\frac{V_\theta}{r}A \mp i\frac{2V_\theta}{r}B \mp \frac{1}{\mathrm{Re}}\left\{\frac{1}{r}\frac{dA}{dr} \mp \frac{n^2}{r^2}A \mp \frac{2n}{r^2}B\right\} \mp Np\left[\omega\frac{dD}{dr} \mp n\frac{V_\theta}{r}\frac{dD}{dr} \mp n\frac{V_\theta}{r^2}D \mp A\frac{d^2\overline{P}}{dr^2}\right] \mp i\frac{dD}{dr} \mp$$

$$\mp ie^{i(\omega t + n\theta)}\left[\left(A\frac{dA}{dr} \mp \frac{n}{r}AB \mp \frac{B^2}{r}\right) \mp iNp\left(A\frac{d^2D}{dr^2} \mp n\frac{B}{r}\frac{dD}{dr} \mp \frac{n}{r^2}DB\right)\right]$$

The real part of this equation is the governing equation for the state variable χ_1 , as follow,

$$\frac{d\chi_1}{dr} =$$

$$\text{Re}\cdot real\left\langle \left[\omega A + in\frac{V_\theta}{r}A + i\frac{2V_\theta}{r}B + \frac{1}{\text{Re}}\left\{\frac{1}{r}\frac{dA}{dr} + \frac{n^2}{r^2}A + \frac{2n}{r^2}B\right\} + Np\left[\omega\frac{dD}{dr} + n\frac{V_\theta}{r}\frac{dD}{dr} + n\frac{V_\theta}{r^2}D + A\frac{d^2\overline{P}}{dr^2}\right] + i\frac{dD}{dr} + \right.\right.$$
$$\left.\left. + ie^{i(\omega t + n\theta)}\left[\left(A\frac{dA}{dr} + \frac{n}{r}AB + \frac{B^2}{r}\right) + iNp\left(n\frac{B}{r}\frac{dD}{dr} + \frac{n}{r^2}DB\right)\right]\right\rangle \quad (4.17)$$

Accordingly, the imaginary part is the governing equation for χ_3 ,

$$\frac{d\chi_3}{dr} =$$

$$\text{Re}\cdot imag\left\langle \left[\omega A + in\frac{V_\theta}{r}A + i\frac{2V_\theta}{r}B + \frac{1}{\text{Re}}\left\{\frac{1}{r}\frac{dA}{dr} + \frac{n^2}{r^2}A + \frac{2n}{r^2}B\right\} + Np\left[\omega\frac{dD}{dr} + n\frac{V_\theta}{r}\frac{dD}{dr} + n\frac{V_\theta}{r^2}D + A\frac{d^2\overline{P}}{dr^2}\right] + i\frac{dD}{dr} + \right.\right.$$
$$\left.\left. + ie^{i(\omega t + n\theta)}\left[\left(A\frac{dA}{dr} + \frac{n}{r}AB + \frac{B^2}{r}\right) + iNp\left(n\frac{B}{r}\frac{dD}{dr} + \frac{n}{r^2}DB\right)\right]\right\rangle \quad (4.18)$$

Equation (3.37) can be re-written as,

$$\frac{1}{\text{Re}}\frac{d^2B}{dr^2} = i\omega B + iA\frac{dV_\theta}{dr} + in\frac{V_\theta}{r}B + \frac{V_\theta}{r}A + \frac{1}{\text{Re}}\left\{\frac{1}{r}\frac{dB}{dr} + \frac{n^2}{r^2}B + n\frac{2}{r^2}A\right\} + Np\left[in\frac{\omega}{r}D + \frac{n^2V_\theta}{r^2}D + \frac{V_\theta}{r}\frac{dD}{dr} + \frac{B}{r}\frac{d\overline{P}}{dr}\right]$$
$$+ i\frac{n}{r}D + e^{i(\omega t + n\theta)}\left[Np\left(+ n\frac{A}{r}\frac{dD}{dr} + \frac{n^2}{r^2}BD + \frac{B}{r}\frac{dD}{dr} + n\frac{A}{r^2}D\right) + \left(iA\frac{dB}{dr} + in\frac{B^2}{r} + i\frac{AB}{r}\right)\right]$$

The real part of this equation is governing equation for χ_5 ,

$$\frac{d\chi_5}{dr} = \text{Re}\cdot real\left\langle i\omega B + iA\frac{dV_\theta}{dr} + in\frac{V_\theta}{r}B + \frac{V_\theta}{r}A + \frac{1}{\text{Re}}\left\{\frac{1}{r}\frac{dB}{dr} + \frac{n^2}{r^2}B + n\frac{2}{r^2}A\right\} + Np\left[in\frac{\omega}{r}D + \frac{n^2V_\theta}{r^2}D + \frac{V_\theta}{r}\frac{dD}{dr} + \frac{B}{r}\frac{d\overline{P}}{dr}\right]\right.$$
$$\left. + i\frac{n}{r}D + e^{i(\omega t + n\theta)}\left[Np\left(+ n\frac{A}{r}\frac{dD}{dr} + \frac{n^2}{r^2}BD + \frac{B}{r}\frac{dD}{dr} + n\frac{A}{r^2}D\right) + \left(iA\frac{dB}{dr} + in\frac{B^2}{r} + i\frac{AB}{r}\right)\right]\right\rangle \quad (4.19)$$

And the imaginary is for χ_7 ,

$$\frac{d\chi_7}{dr} =$$

$$\text{Re}\cdot imag\left\langle i\omega B - iA\frac{dV_\theta}{dr} - in\frac{V_\theta}{r}B - \frac{V_\theta}{r}A - \frac{1}{\text{Re}}\left\{\frac{1}{r}\frac{dB}{dr} - \frac{n^2}{r^2}B - n\frac{2}{r^2}A\right\} - Np\left[in\frac{\omega}{r}D - \frac{n^2V_\theta}{r^2}D - \frac{V_\theta}{r}\frac{dD}{dr} - \frac{B}{r}\frac{d\bar{P}}{dr}\right]\right.$$
$$\left. - i\frac{n}{r}D - e^{i(\omega t - n\theta)}\left[Np\left(-n\frac{A}{r}\frac{dD}{dr} - \frac{n^2}{r^2}BD - \frac{B}{r}\frac{dD}{dr} - n\frac{A}{r^2}D\right) - \left(iA\frac{dB}{dr} - in\frac{B^2}{r} - i\frac{AB}{r}\right)\right]\right\rangle \quad (4.20)$$

Now the pressure equation (3.52) is re-written after combining similar terms and writing the equation in term of the highest pressure function derivative,

$$\left[1 - iNp\left(\omega - \frac{nV_\theta}{r}\right)\right]\tilde{\nabla}^2 D =$$

$$iNp\frac{d^2\bar{P}}{dr^2}\frac{dA}{dr} - \left[\frac{2n}{r}\frac{dV_\theta}{dr} - iNp\left(\frac{d^3\bar{P}}{dr^3} - \frac{1}{r}\frac{d^2\bar{P}}{dr^2}\right)\right]A - \frac{2V_\theta}{r}\frac{dB}{\partial r} - \left(iNp\frac{n}{r^2}\frac{d\bar{P}}{dr} - \frac{2}{r}\frac{dV_\theta}{dr}\right)B -$$

$$- Np\left[\frac{1}{r}\frac{dV_\theta}{dr}\frac{d}{dr} - \frac{1}{r^2}\frac{dV_\theta}{dr} - \frac{V_\theta}{r^3}\right]inD - e^{i(\omega t - n\theta)}\left[\left(\frac{dA}{dr}\right)^2 - \frac{n^2}{r^2}B^2 - \frac{n}{r^2}AB - \frac{A}{r}\frac{dA}{dr} - \frac{2n}{r}A\frac{dB}{dr} - \frac{2}{r}B\frac{dB}{dr}\right]$$

$$- ie^{i(\omega t - n\theta)}Np\left[\frac{2n}{r^2}B\frac{dD}{dr} - \frac{n}{r^2}D\frac{dB}{dr} - \left(\frac{n}{r^3} - \frac{2n^3}{r^3}\right)BD - \frac{2n^2}{r^2}A\frac{dD}{dr} - \frac{2n^2}{r^3}AD\right] \quad (4.21)$$

Writing the Equation (4.20) in terms of the second derivative of pressure,

$$\left[1 - iNp\left(\omega - \frac{nV_\theta}{r}\right)\right]\frac{d^2D}{dr^2} = iNp\frac{d^2\bar{P}}{dr^2}\frac{dA}{dr} - \left[\frac{2n}{r}\frac{dV_\theta}{dr} - iNp\left(\frac{d^3\bar{P}}{dr^3} - \frac{1}{r}\frac{d^2\bar{P}}{dr^2}\right)\right]A -$$

$$- \frac{2V_\theta}{r}\frac{dB}{\partial r} - \left(iNp\frac{n}{r^2}\frac{d\bar{P}}{dr} - \frac{2}{r}\frac{dV_\theta}{dr}\right)B -$$

$$- \left[1 - iNp\left(\omega - \frac{nV_\theta}{r}\right)\right]\left(\frac{1}{r}\frac{dD}{dr} - \frac{n^2}{r^2}D\right) - Np\left[\frac{1}{r}\frac{dV_\theta}{dr}\frac{d}{dr} - \frac{1}{r^2}\frac{dV_\theta}{dr} - \frac{V_\theta}{r^3}\right]inD -$$

$$- e^{i(\omega t - n\theta)}\left[\left(\frac{dA}{dr}\right)^2 - \frac{n^2}{r^2}B^2 - \frac{n}{r^2}AB - \frac{A}{r}\frac{dA}{dr} - \frac{2n}{r}A\frac{dB}{dr} - \frac{2}{r}B\frac{dB}{dr}\right]$$
$$- ie^{i(\omega t - n\theta)}Np\left[\frac{2n}{r^2}B\frac{dD}{dr} - \frac{n}{r^2}D\frac{dB}{dr} - \left(\frac{n}{r^3} - \frac{2n^3}{r^3}\right)BD - \frac{2n^2}{r^2}A\frac{dD}{dr} - \frac{2n^2}{r^3}AD\right]$$

Arranging the coefficients from the right hand side,

$$\frac{d^2D}{dr^2}=\frac{1}{\left[1-iNp\left(\omega-\frac{nV_\theta}{r}\right)\right]}\left\langle iNp\frac{d^2\overline{P}}{dr^2}\frac{dA}{dr}-\left[\frac{2n}{r}\frac{dV_\theta}{dr}-iNp\left(\frac{d^3\overline{P}}{dr^3}-\frac{1}{r}\frac{d^2\overline{P}}{dr^2}\right)\right]A-\frac{2V_\theta}{r}\frac{dB}{\partial r}-\right.$$

$$-\left(iNp\frac{n}{r^2}\frac{d\overline{P}}{dr}-\frac{2}{r}\frac{dV_\theta}{dr}\right)B-\left\{-\frac{1}{r}\left[1-iNp\left(\omega-\frac{nV_\theta}{r}\right)\right]-iNp\frac{n}{r}\frac{dV_\theta}{dr}\right\}\frac{dD}{dr}-$$

$$-\left\{\frac{n^2}{r^2}\left[1-iNp\left(\omega-\frac{nV_\theta}{r}\right)\right]-inNp\left(-\frac{1}{r^2}\frac{dV_\theta}{dr}-\frac{V_\theta}{r^3}\right)\right\}D$$

$$-e^{i(\omega t-n\theta)}\left\{iNp\left[\frac{2n}{r^2}B\frac{dD}{dr}-\frac{n}{r^2}D\frac{dB}{dr}-\left(\frac{n}{r^3}-\frac{2n^3}{r^3}\right)BD-\frac{2n^2}{r^2}A\frac{dD}{dr}-\frac{2n^2}{r^3}AD\right]\right\}$$

$$\left.-e^{i(\omega t-n\theta)}\left\{\left[\left(\frac{dA}{dr}\right)^2-\frac{n^2}{r^2}B^2-\frac{n}{r^2}AB-\frac{A}{r}\frac{dA}{dr}-\frac{2n}{r}A\frac{dB}{dr}-\frac{2}{r}B\frac{dB}{dr}\right]\right\}\right\rangle \quad (4.22)$$

The real part of this equation is the governing equation for state-variable χ_9,

$$\frac{d\chi_9}{dr}=real\left|\frac{1}{\left[1-iNp\left(\omega-\frac{nV_\theta}{r}\right)\right]}\left\langle iNp\frac{d^2\overline{P}}{dr^2}\frac{dA}{dr}-\left[\frac{2n}{r}\frac{dV_\theta}{dr}-iNp\left(\frac{d^3\overline{P}}{dr^3}-\frac{1}{r}\frac{d^2\overline{P}}{dr^2}\right)\right]A-\frac{2V_\theta}{r}\frac{dB}{\partial r}-\right.\right.$$

$$-\left(iNp\frac{n}{r^2}\frac{d\overline{P}}{dr}-\frac{2}{r}\frac{dV_\theta}{dr}\right)B-\left\{-\frac{1}{r}\left[1-iNp\left(\omega-\frac{nV_\theta}{r}\right)\right]-iNp\frac{n}{r}\frac{dV_\theta}{dr}\right\}\frac{dD}{dr}-$$

$$-\left\{\frac{n^2}{r^2}\left[1-iNp\left(\omega-\frac{nV_\theta}{r}\right)\right]-inNp\left(-\frac{1}{r^2}\frac{dV_\theta}{dr}-\frac{V_\theta}{r^3}\right)\right\}D$$

$$-e^{i(\omega t-n\theta)}\left\{iNp\left[\frac{2n}{r^2}B\frac{dD}{dr}-\frac{n}{r^2}D\frac{dB}{dr}-\left(\frac{n}{r^3}-\frac{2n^3}{r^3}\right)BD-\frac{2n^2}{r^2}A\frac{dD}{dr}-\frac{2n^2}{r^3}AD\right]\right\}$$

$$\left.\left.-e^{i(\omega t-n\theta)}\left\{\left(\frac{dA}{dr}\right)^2-\frac{n^2}{r^2}B^2-\frac{n}{r^2}AB-\frac{A}{r}\frac{dA}{dr}-\frac{2n}{r}A\frac{dB}{dr}-\frac{2}{r}B\frac{dB}{dr}\right\}\right\rangle\right| \quad (4.23)$$

And the imaginary part of Equation (4.21) is the governing equation for χ_{11},

$$\frac{d\chi_{11}}{dr} = imag\left\{\frac{1}{\left[1 - iNp\left(\omega - \frac{nV_\theta}{r}\right)\right]}\left\langle iNp\frac{d^2\bar{P}}{dr^2}\frac{dA}{dr} - \left[\frac{2n}{r}\frac{dV_\theta}{dr} - iNp\left(\frac{d^3\bar{P}}{dr^3} - \frac{1}{r}\frac{d^2\bar{P}}{dr^2}\right)\right]A - \frac{2V_\theta}{r}\frac{dB}{\partial r} -\right.\right.$$

$$-\left(iNp\frac{n}{r^2}\frac{d\bar{P}}{dr} - \frac{2}{r}\frac{dV_\theta}{dr}\right)B - \left\{-\frac{1}{r}\left[1 - iNp\left(\omega - \frac{nV_\theta}{r}\right)\right] - iNp\frac{n}{r}\frac{dV_\theta}{dr}\right\}\frac{dD}{dr} -$$

$$-\left\{\frac{n^2}{r^2}\left[1 - iNp\left(\omega - \frac{nV_\theta}{r}\right)\right] - inNp\left(-\frac{1}{r^2}\frac{dV_\theta}{dr} - \frac{V_\theta}{r^3}\right)\right\}D$$

$$- e^{i\cdot\omega t - n\theta}\left\{\left(\frac{dA}{dr}\right)^2 - \frac{n^2}{r^2}B^2 - \frac{n}{r^2}AB - \frac{A}{r}\frac{dA}{dr} - \frac{2n}{r}A\frac{dB}{dr} - \frac{2}{r}B\frac{dB}{dr}\right\}$$

$$\left.\left. - e^{i\cdot\omega t - n\theta}\left\{iNp\left[\frac{2n}{r^2}B\frac{dD}{dr} - \frac{n}{r^2}D\frac{dB}{dr} - \left(\frac{n}{r^3} - \frac{2n^3}{r^3}\right)BD - \frac{2n^2}{r^2}A\frac{dD}{dr} - \frac{2n^2}{r^3}AD\right]\right\}\right\rangle\right| \quad (4.24)$$

The next steps in solving the state variable model for this non-linear system follow the same procedure employed for the previous linear system.

4.3 Summary

In this chapter (4) the state variable governing equations model was developed for both the linear and the non-linear systems of an unsteady axial vortex flow. A discussion of the model parameters and their evaluation process were outlined.

CHAPTER 5

FINDINGS AND DISCUSSION

The state variable model for a perturbed vortical flow is a new method to study its stability. The twelve state variables in Table 4.1 are employed to model the flow at each spatial location, at a given instant of time, then the state equations were integrated using a fourth order Runge-Kutta method to advance the solution radially to the next spatial location. The four control parameters were the non-equilibrium swirl parameter, *Np*, Reynolds number, *Re*, the perturbation frequency, ω_R, and the azimuthal orientation mode number, n, with values guided by the physical range investigated in the low speed wind tunnel at Old Dominion University. The parametric value range also revealed different kinds of modes of instability. In this chapter, different levels of each of these parameters will be investigated to draw conclusions about their effects on the instability growth in the flow. The stability analysis will follow the discussion of results in order to validate the existence of the instabilities revealed in this study and determine the stability status of the flow.

Matlab® was employed to produce the state-variable simulations. Program scripts were written to examine perturbation behavior for Reynolds numbers between 6,000 and 14,000 (Appendix C), utilizing maximum azimuthal velocity and core radius as the velocity and length scales. The steady-state velocity profiles and pressure distributions employed in this study were based on the axial vortex solution-Equation (3.1) by Ash, Zardadkhan, and Zuckerwar (2011) and the fundamental interpretation of the state variable model discussed in Section 4.1.2. Wind tunnel experiments performed in the low speed wind tunnel at Old Dominion University helped in defining the physical range of Reynolds numbers

investigated so that the results presented here can be verified employing hotwire anemometer measurements in the low speed wind tunnel.

Four perturbation amplitude variables were utilized to describe the evolution of perturbations in the flow, the radial velocity amplitude, v_r', the azimuthal velocity amplitude v_θ', the perturbation Reynolds stress $\langle v_r' v_\theta' \rangle$, and the radial perturbation pressure gradient amplitude $\left(dp'/dr \right)$.

The amplitude of radial perturbation pressure gradient was included in this discussion instead of pressure amplitude because the pressure gradient is the mechanism by which non-equilibrium forces are sustained. On the other hand, the pressure differential equations are many orders higher than the velocity ones, since the pressure equations were firstly composed by taking the divergence of the conservation of the momentum, taking the equations to a higher differential order. Solving the pressure equation for the pressure function requires two integration steps, which necessitates a numerical solution at mid-points before marching to the next step, hence the pressure gradient is the first integration output and is considered to have a stable numerical solution. Stability analysis of the state variable model is discussed in chapter six of this study and detailed description of the pressure solution is outlined.

The state variable filter used in this study provides a useful integration representation of the perturbation amplitudes since any instantaneous distribution will contain noise. The Matlab® *butter* function was utilized to plot the output perturbation amplitudes. These functions generate a low-pass digital filter with a specific order and cutoff frequency. The filter can cutoff up to half the maximum sample rate. The order of the filter determines how extreme the high frequencies will be removed from the sample

and affects the phase shift of the waves only when it is too high (5^{th} order and more), the filter order used here was third order. Please refer to Butterworth filter design page http://www.mathworks.com/help/signal/ref/butter.html.

5.1 Influence of *Np* on velocity, pressure and Reynolds stresses

The non-equilibrium swirl parameter (*Np*) is a ratio of the time during which the non-equilibrium pressure gradient forces act on fluid particles, with respect to the characteristic swirl convective time. As *Np* increases, the time during which non-equilibrium pressure gradient forces can be exerted by external perturbations increases. During that time, the viscous stresses required to balance the non-equilibrium pressure gradient forces interact with the externally imposed perturbations. Those viscous stresses may suppress the perturbations, or in some cases, enhance the instability caused by the presence of the disturbances within the vortex flow.

The physical range of *Np* for the vortex flow under investigation was determined using the basic flow properties from wind tunnel experiment (Ely, 2013) that is, in those experiments the pressure relaxation coefficients for air varied between (0.2 and 0.5) microseconds, the angular rotation rate varied between (500 and 1500) rad/sec, and using equation (3·8) the resulting range for swirl parameter was $10^{-4} < Np < 10^{-3}$.

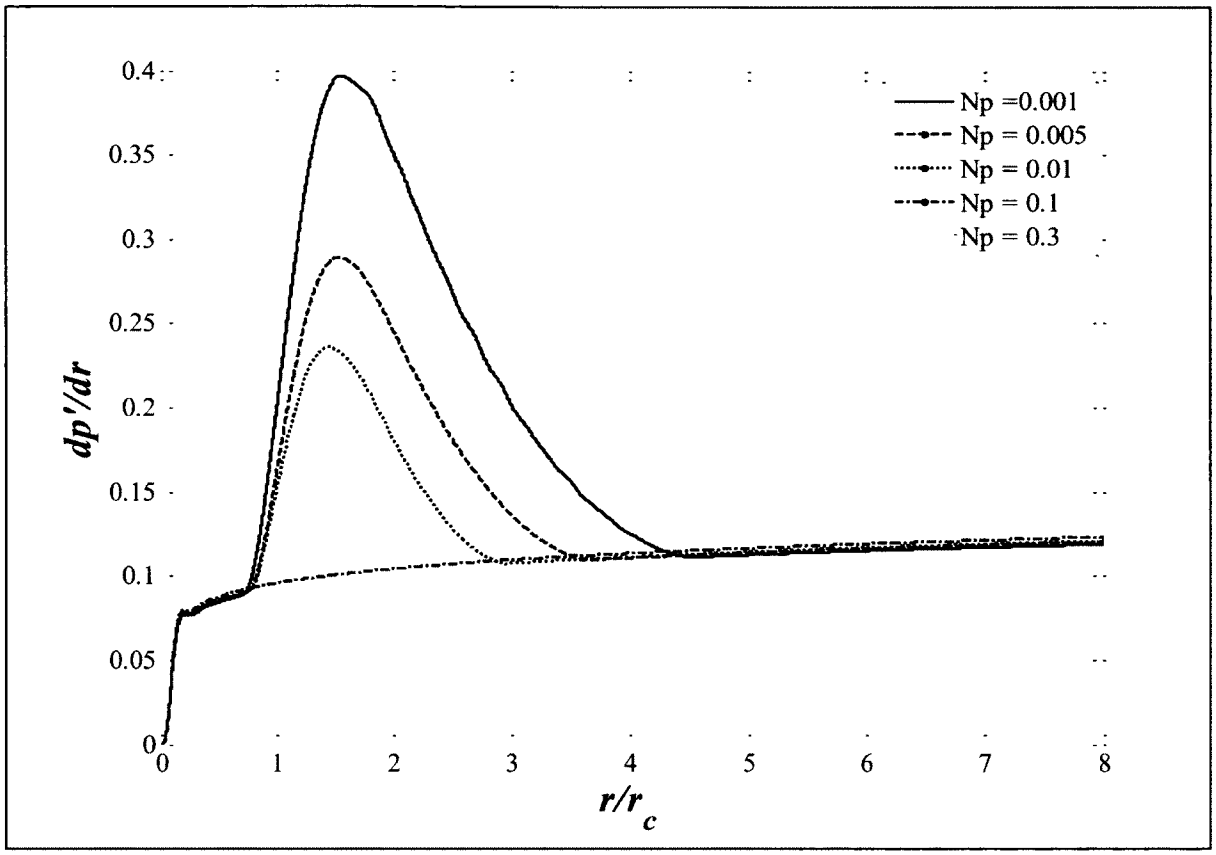

Figure 5.1 The radial pressure gradient amplitude variation with radius at different *Np* (ω_R = *0.4, n = 1/2 Re = 8,000*)

The influence of the non-equilibrium swirl parameter on the amplitude of the radial pressure gradient perturbation is displayed in Figure 5.1. Near the core radius, the radial pressure gradient oscillation amplitudes are very large at the smallest values of the non-equilibrium swirl parameter, but that maximum amplitude "bulge" vanishes by the time *Np* is equal to 0.3. Interestingly, the large-amplitude bulge does not occur inside the core, and the overall radial pressure gradient oscillation amplitudes remain below 0.1 dimensionless pressure units over the core region of the vortex. Within the non-equilibrium pressure zone, the amplitude profile reached a maximum value that was dependent on *Np*. This location of maximum amplitude growth is referred to as the *critical radius*. Then the

pressure gradient amplitude decreased rapidly back to a value between 0.1 and 0.15. However, as can be seen in Figure 5.1, the amplitude of the perturbation pressure gradient does not go to zero, even for very large radii, raising a question of how to interpret it.

There are two main reasons why the pressure gradient did not go to zero before the outer boundaries of the flow were reached. The first reason would be the interaction between the vortex trying to rotate the fluid particles around the center and the surrounding environment which kept the particles at rest for ambient conditions. The other important reason would be the possibility of a sound source associated with this kind of vortex flow as mentioned in the introduction section 1.2. That sound propagation from inside to outside the vortex flow would be due to the residual pressure perturbations exhibited in Figure 5.1. The theory behind this assertion could be extracted from equation 1.7 of section 1.2,

$$\rho\frac{Dv_i}{Dt} = -\frac{\partial P}{\partial x_i} - \eta_p\frac{D}{Dt}\left(\frac{\partial P}{\partial x_i}\right) - \eta_p\left[\frac{\partial v_k}{\partial x_i}\frac{\partial P}{\partial x_k} - \frac{\eta_V - \frac{1}{3}\mu}{\eta_P}\frac{\partial}{\partial x_i}\left(\frac{1}{\rho}\frac{D\rho}{Dt}\right)\right] + \mu\frac{\partial^2 v_i}{\partial x_k^2},$$

As noted in Chapter 1, the first terms in the square bracket represent the contracted velocity-tensor-pressure gradient term that resulted when considering the material derivative of the pressure gradient instead of the gradient of the material derivative of pressure in forming the non-equilibrium pressure term in the momentum equation; it was postulated that this contracted velocity-pressure gradient term balanced the fluctuation in the density of the fluid due to the generated sound within the non-equilibrium pressure zone. This assumption of cancelling the square bracketed term is going to be reflected as a change in the gradient of the pressure of the flow within the non-equilibrium pressure zone (the core region just prior to the potential flow zone), and that is the "bulges" seen in Figure

5.1. Thus, sound is generated in the vortical flow inside the non-equilibrium pressure zone and the gradient of pressure will increase to balance the sound disturbance.

The variation in the amplitude of the azimuthal velocity perturbation with radius is shown in Figure 5.2, for values of *Np* between 0.0001 and 0.3. For small values of *Np,* the perturbation amplitudes are rather large out to 10 or 15 core radii, but in all cases the amplitude peaks within the non-equilibrium pressure zone and decreases to negligibly small amplitudes at large radii. For $Np = 0.3$, the large perturbation amplitude band was much narrower. It should also be noted that as *Np* increased, the maximum amplitude of the azimuthal velocity perturbation decreased and the critical radius migrated toward the core radius within the non-equilibrium pressure zone.

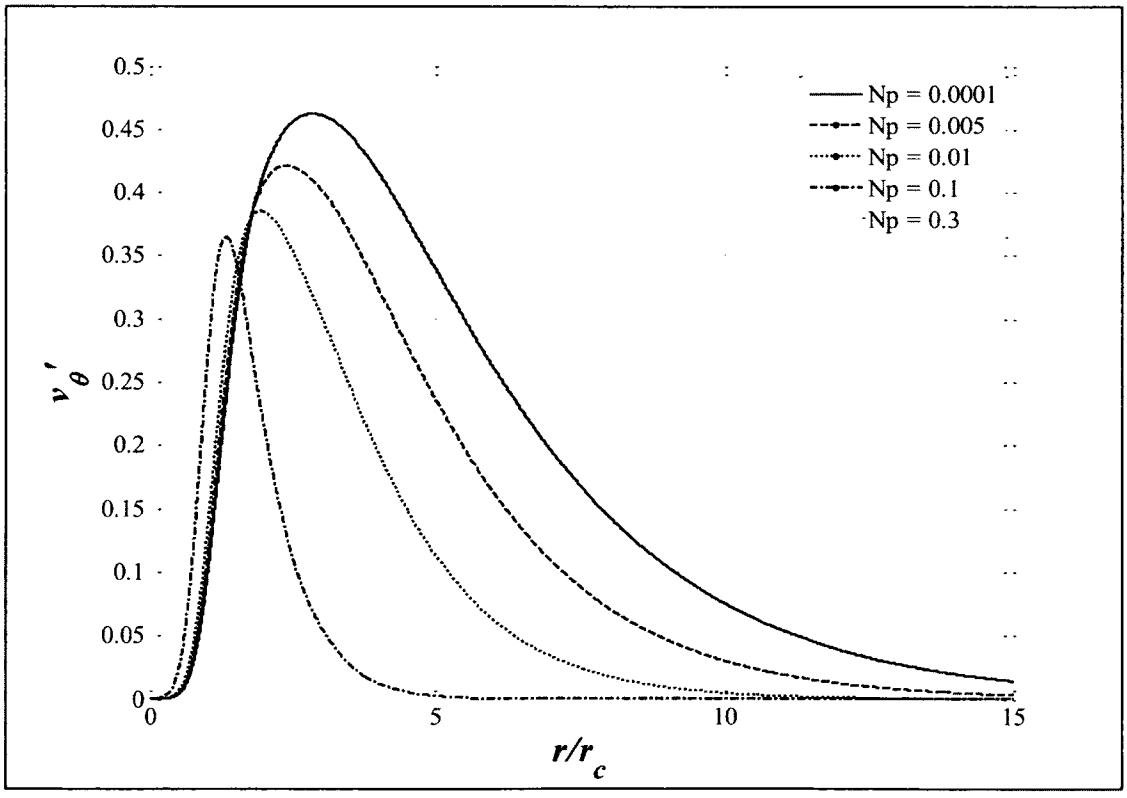

Figure 5.2 The azimuthal velocity perturbation amplitude variation with radius at different *Np* ($\omega_R = 0.4$, $n = 1/2$ *Re = 8,000*)

Figure 5.3 shows how different values of *Np* (between 0.0001 and 0.3) influence the growth and decay of the radial velocity perturbations at *Re* = 8,000. For all values of *Np*, the radial velocity perturbation was necessarily zero at the centerline, and the figure shows that the magnitude of the radial perturbation velocity amplitude increased with radius until a maximum instability magnitude was reached, before decaying back to zero at the outer radial limit. Note that the magnitude of the radial velocity perturbation reaches a maximum value at distances greater than one core radius. The figure also shows that as the non-equilibrium swirl parameter was increased from an extremely small value of 0.0001 to 0.3, the radial perturbation velocity magnitude at the critical radius was hardly affected. In this case, it was noted that inclusion of the relaxation stresses didn't influence the maximum growth of perturbations but the critical radius moved slightly closer to the core radius with increasing *Np*. More discussion of the maximum growth along with the migration of the critical radius will follow.

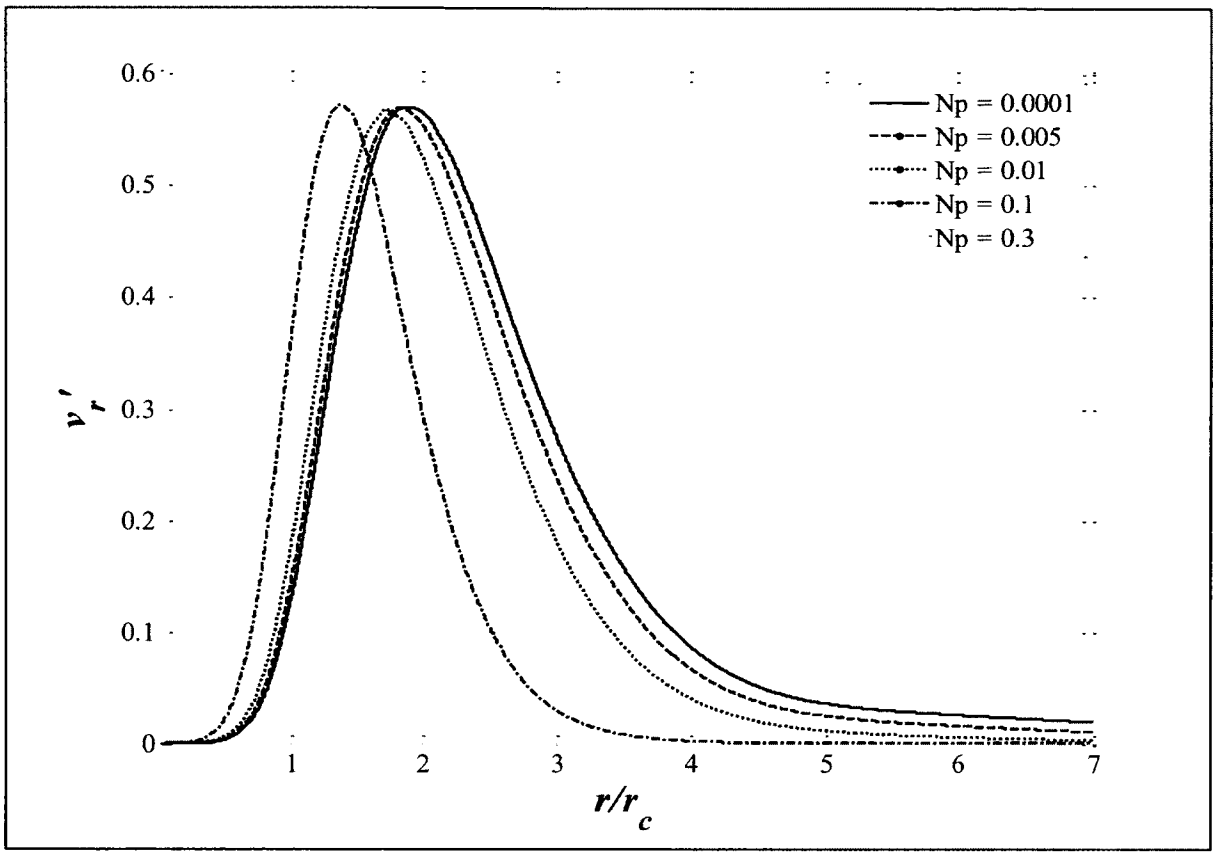

Figure 5.3 The radial velocity perturbation amplitude variation with radius at different *Np* (ω_R = *0.4, n = 1/2 Re = 8,000*)

The $\rho\langle v_r' v_\theta' \rangle$ perturbation Reynolds stress variation with radius is shown in Figure 5.4. The distribution follows the same trend as the velocity perturbations with a peak in the non-equilibrium pressure zone and equal to zero at the center of the vortex and at the far-field boundary. This "turbulent zone" is located in the non-equilibrium pressure region, where the relaxation stresses exerted by the perturbations in the flow work to grow instabilities to varying degrees, depending on the value of *Np*. Significant levels of this component of Reynolds stress were produced over a wide interval within the non-equilibrium pressure zone, especially for the lower values of *Np* (0.0001, 0.005 and 0.01);

as *Np* increased further, the Reynolds stresses were concentrated in a narrower band located closer to the core radius.

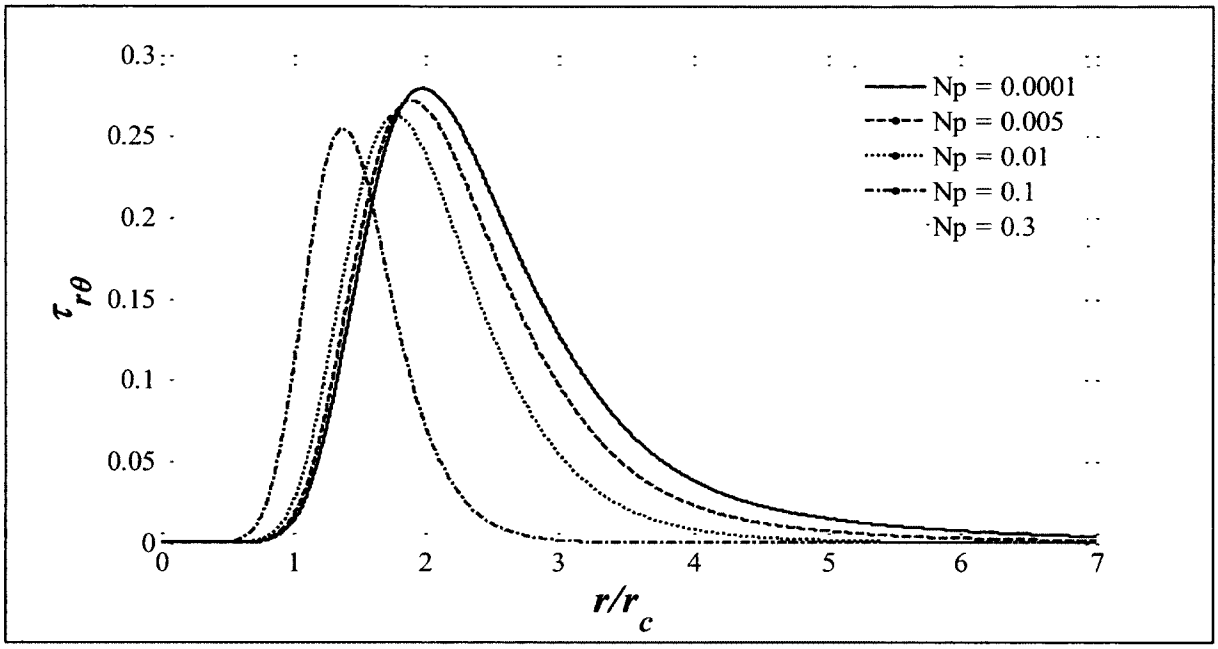

Figure 5.4 Variation of $\rho\langle v_r' v_\theta' \rangle$ Reynolds Stress with radius for different *Np* ($\omega_R = 0.4$, $n = 1/2$ $Re = 8{,}000$)

It was concluded that the relaxation process enhanced the growth of perturbed radial pressure gradient inside the non-equilibrium pressure zone over the range of values of *Np*.

5.2 Effect of Np on maximum perturbation growth and critical radii

To study the effect of *Np* on maximum perturbation growth, a simple *max function* in Matlab® was used to extract both maximum amplitude and critical radius. Perturbations in velocity, radial pressure gradient, and Reynolds stresses are the parameters used here to describe the growth quantitatively. Figure 5.5 shows the influence of the swirl parameter *Np* on the maximum perturbation amplitudes. There were general trends of decreasing amplitudes as the swirl parameter was increased to higher levels, indicating that the relaxation stresses, when allowed more time on a relative basis, tended to break down the instability, diminishing its magnitude and thus helping stabilize the vortex.

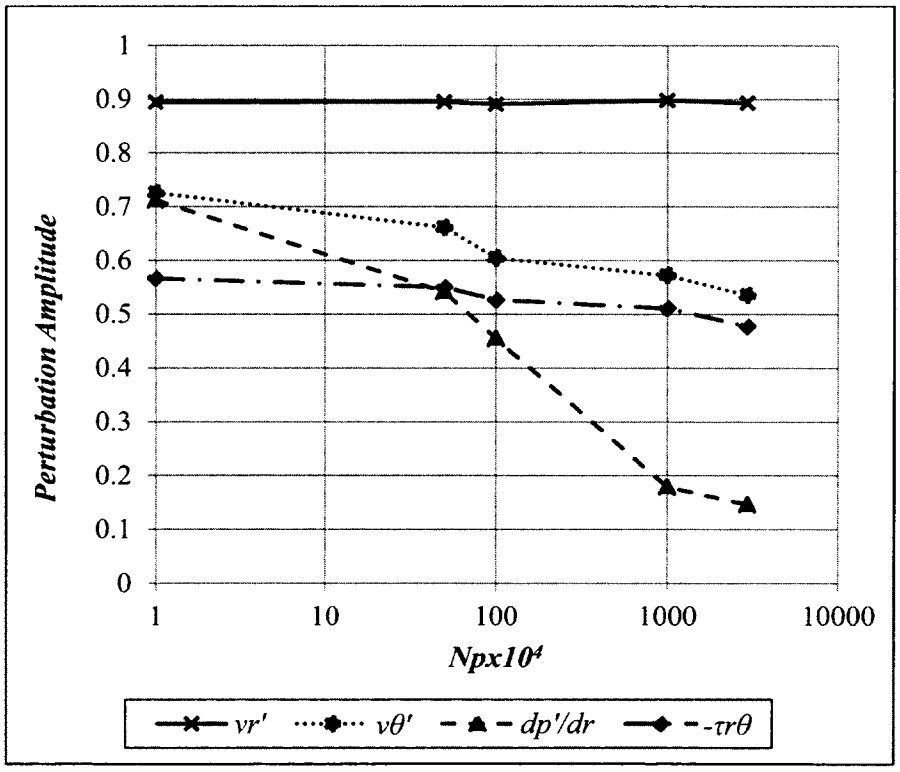

Figure 5.5 Influence of *Np* on the maximum perturbation amplitudes (ω_R = *0.4, n = 1/2 Re = 8,000*)

Effects like this can be significant when considering actual variations in the environmental humidity levels. Since the pressure relaxation coefficient increases with decreasing humidity (Figure 1.2), the swirl parameter increases as well (Equation 3·8), as a result, the perturbations in the flow are damped (Figure 5.5). The perturbations pressure gradient is significantly damped in this process.

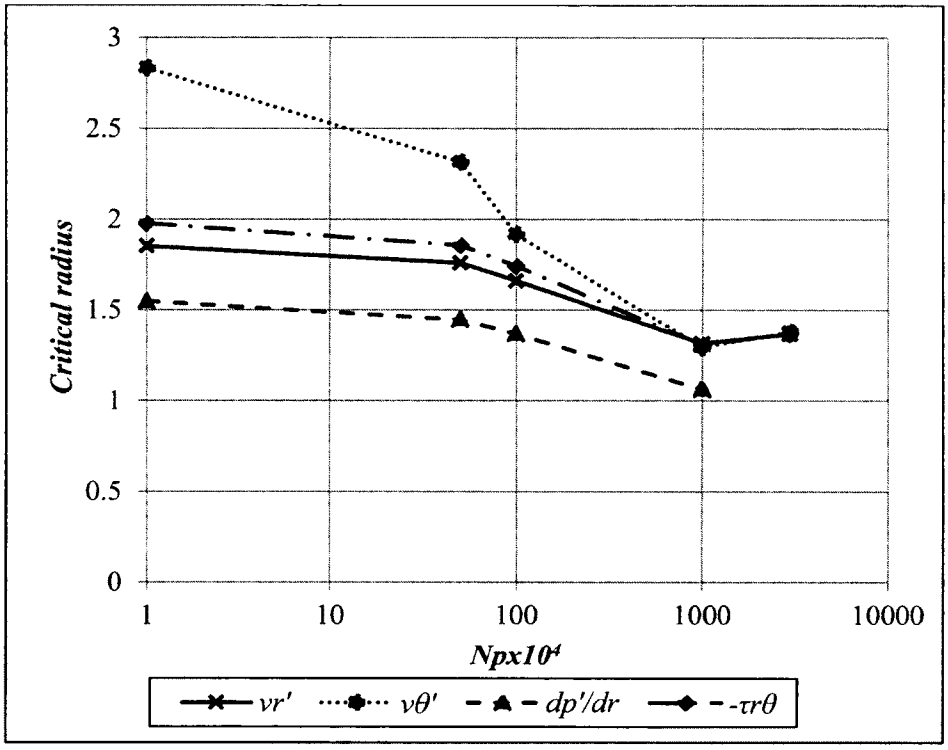

Figure 5.6 Influence of *Np* on the critical radius of perturbations (ω_R = *0.4, n = 1/2 Re = 8,000*)

Figure 5.6 shows how variation in the non-equilibrium swirl parameter influences the critical radius location of maximum perturbation growth (based on the maximum radial perturbations obtained in Figure 5.5). The figure shows that the critical radius resides in

the outer portion of the non-equilibrium pressure zone, but migrates gradually toward the core radius.

In concluding this section, the non-equilibrium swirl parameter, *Np*, has a significant influence on the maximum amplitude growth and location for the perturbation velocity, pressure and Reynolds stress fields. For the most part, perturbation amplitudes decreased with increasing *Np*. The effect of *Np* on the radial pressure gradient was more significant than for the other perturbations. These general trends of decreasing amplitudes as the swirl parameter was increased to higher levels, elevates the importance of relative humidity in considering the unsteady behavior of axial vortices since higher relative humidity corresponds with smaller values of the non-equilibrium swirl parameter and relatively dry air results in increased levels.

5.3 Effect of Reynolds number on perturbation behavior

The Reynolds number affects the velocity perturbation growth, and generally, the velocity perturbations grow with increasing Reynolds number (see Figures 5.7-10). It should be noted that a number of numerical simulations were run for different Reynolds numbers, employing different values of *Np* and the results exhibited the same trends as those exhibited for Re = 8,000, with no noticeable effects on the pressure perturbations (by varying the Reynolds number at fixed *Np*).

Figure 5.7. shows how the radial velocity perturbation amplitude is affected by Reynolds number in the range of 6,000 to 14,000. This is the typical range of the experimental data summarized in Table 1.1. It is very important here to state that at the lower Reynolds numbers, the perturbations were found to be damped and the perturbed

flow was thus more stable. The perturbation amplitudes are completely damped by inertial forces in the vicinity of the rotational axis, and the amplitude profiles have maxima in the the non-equilibrium pressure region. The growth of perturbations was mostly in the non-equilibrium pressure region.

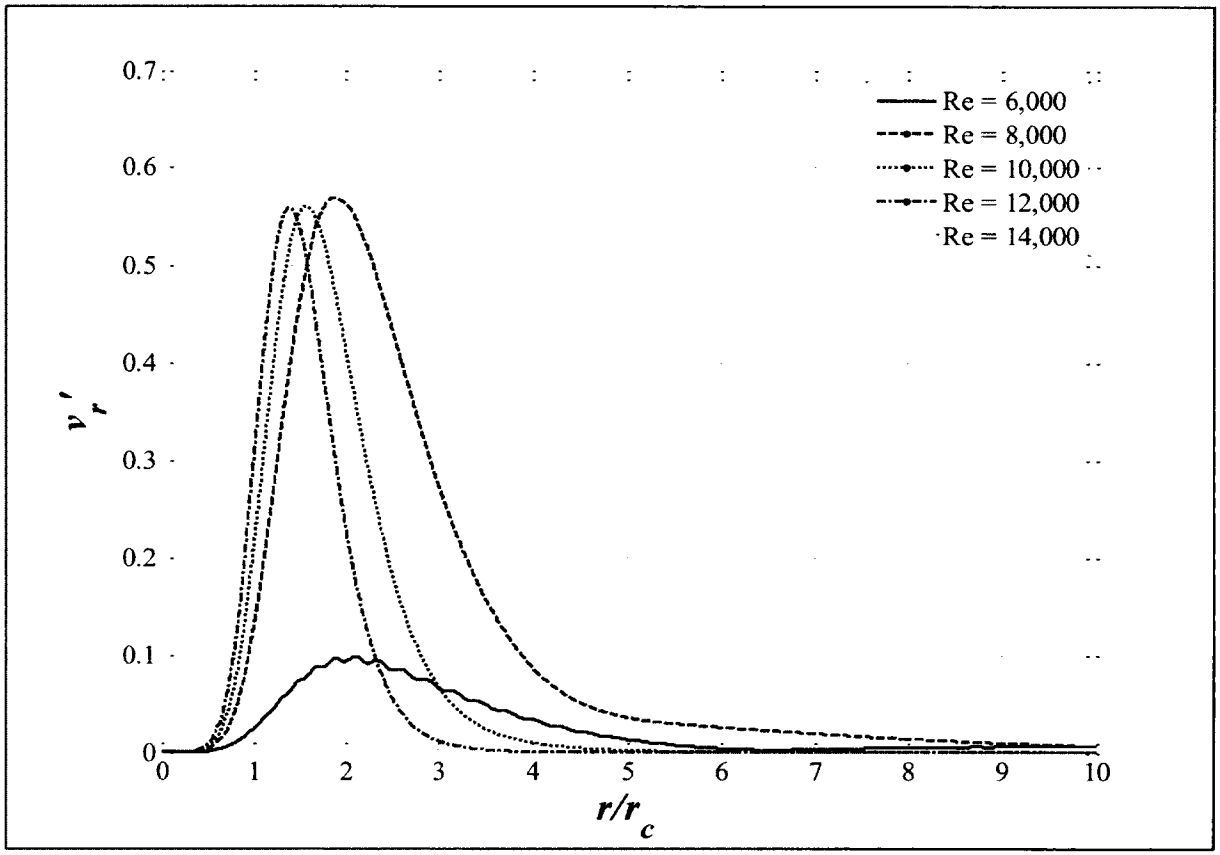

Figure 5.7 The radial velocity perturbation amplitude variation with radius at different Re (ω_R = *0.4, n = 1/2 Np= 2x10^{-4}*)

The azimuthal velocity amplitude profiles were distinctly different below Re=8,000. As shown in Figure 5.8, at Re = 6,000, the amplitude peaked at 0.1, at a location approximately five core radii from the axis, and measurable, low-intensity perturbations spanned the entire radial region. At Re = 8,000, the maximum azimuthal

velocity amplitude was larger than any other Reynolds number and detectable amplitudes were observed over nearly the entire region. The simulations at higher Reynolds numbers (Re of 10,000, 12,000, and 14,000) exhibited peak maximum amplitudes of 0.35 and detectable perturbations only occupied a narrow part of the non-equilibrium pressure zone.

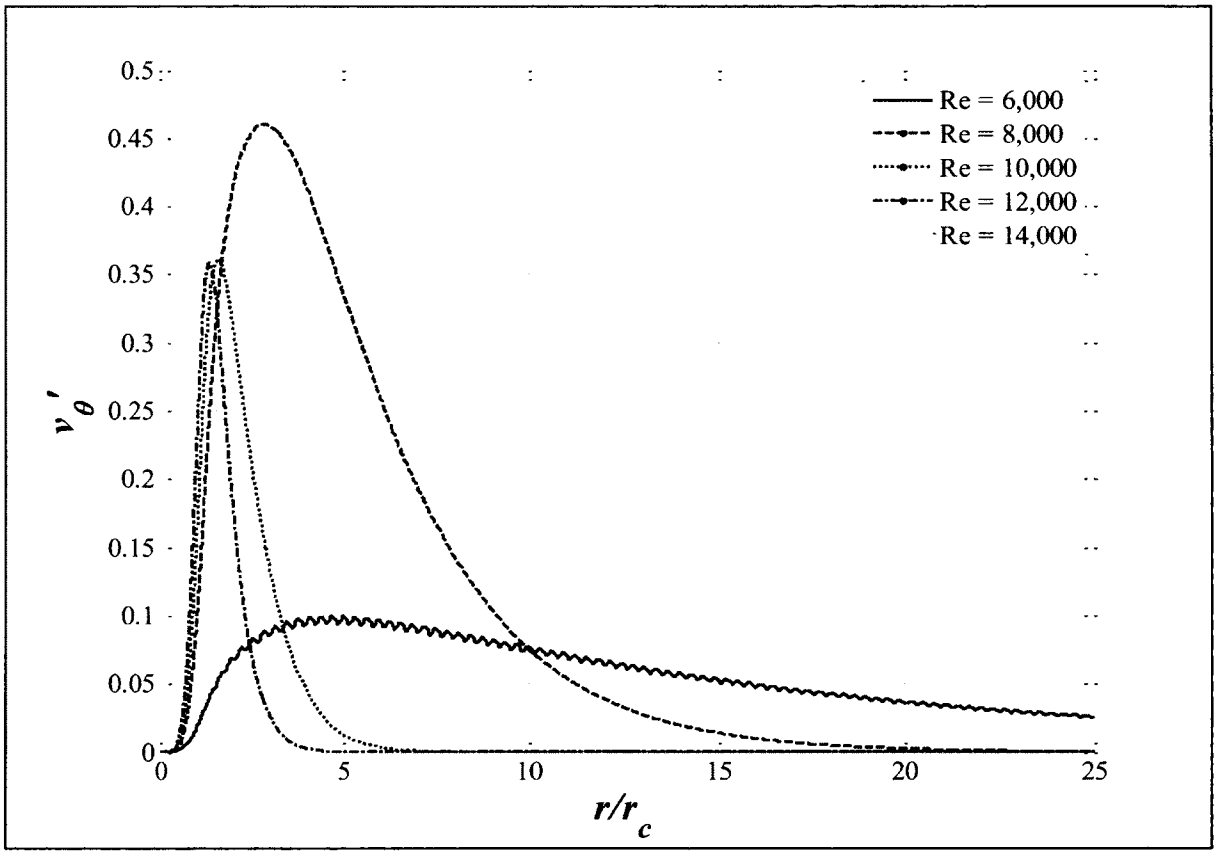

Figure 5.8 The azimuthal velocity perturbation amplitude variation with radius at different Re ($\omega_R = 0.4$, $n = 1/2$ $Np = 2x10^{-4}$)

The influence of Reynolds number on the amplitude of the radial perturbation pressure gradient is displayed in Figure 5.9. At Reynolds numbers above 6,000, there is a pronounced amplitude bulge in the primary non-equilibrium pressure gradient zone. The

perturbation pressure gradient bulge became narrower and steeper as the Reynolds was increased. Outside of the primary non-equilibrium pressure gradient region, the perturbation pressure gradient amplitudes coalesced into a single smooth curve that increased monotonically with radius out to the integration limit. As can be seen in the figure, the amplitude profiles for the different Reynolds number are "universal" from the rotational axis out to just beyond one-half the core radius and the curves coalesce again beyond five core radii. The amplitude bulge could be a driving mechanism linking these small fluid mechanical pressure perturbations being generated in the primary non-equilibrium pressure zone with sound radiation, a possible theory behind this sound wave propagation was outlined in section 1.2 and revisited in section 5.1.

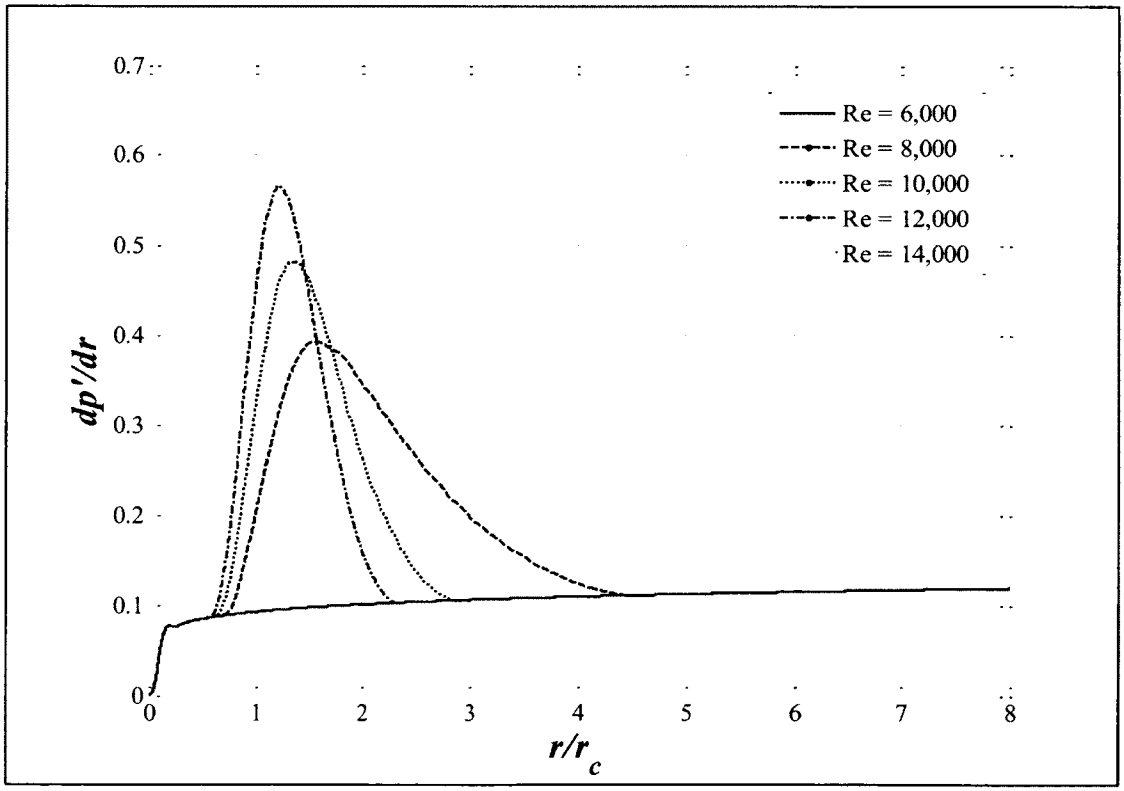

Figure 5.9 The radial pressure gradient amplitude variation with radius at different Re (ω_R = *0.4, n = 1/2 Np=* $2x10^{-4}$)

The influence of Reynolds number on the radial variation of perturbation Reynolds stresses $\langle v_r' v_\theta' \rangle$ is shown in Figure 5.10. Clearly, that component of the Reynolds stress is highly-damped at Re = 6,000, and at higher Reynolds numbers, that Reynolds stress reaches its maximum within the primary non-equilibrium pressure zone, then decreases rapidly to zero at larger radii. The plot shows that the large-amplitude Reynolds stress band narrowed, while the peak amplitude diminished gradually and moved toward the core radius as the Reynolds number was increased.

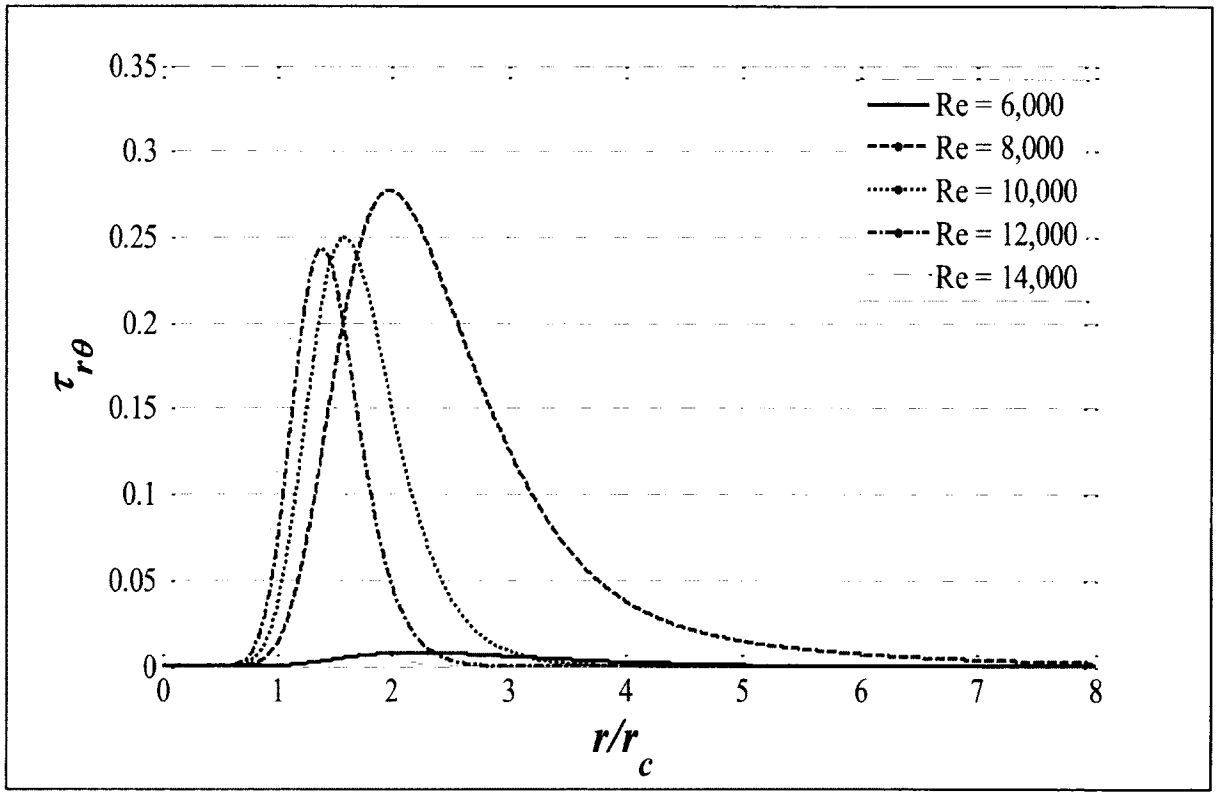

Figure 5.10 Reynolds stresses radial distribution at different Re (ω_R = *0.4, n = 1/2 Np= 2x10^{-4}*)

When the flow becomes unstable; the small turbulent structures travel at high relative speeds and cause the flow region to become chaotic at the same pressure perturbation levels.

5.4 Effect of Reynolds number on maximum perturbation growth and critical radii

The maximum growth of different perturbations as functions of Reynolds number is plotted in Figure 5.11, suggesting a linear increase in maximum radial pressure gradient amplitude with Reynolds number. The azimuthal velocity component and the Reynolds stresses had amplitude peaks at Re = 8,000 and then exhibited virtually no change for the higher Re, whereas the amplitudes at 6,000 had very low intensity compared to other cases. The radial velocity component was hardly affected by Re.

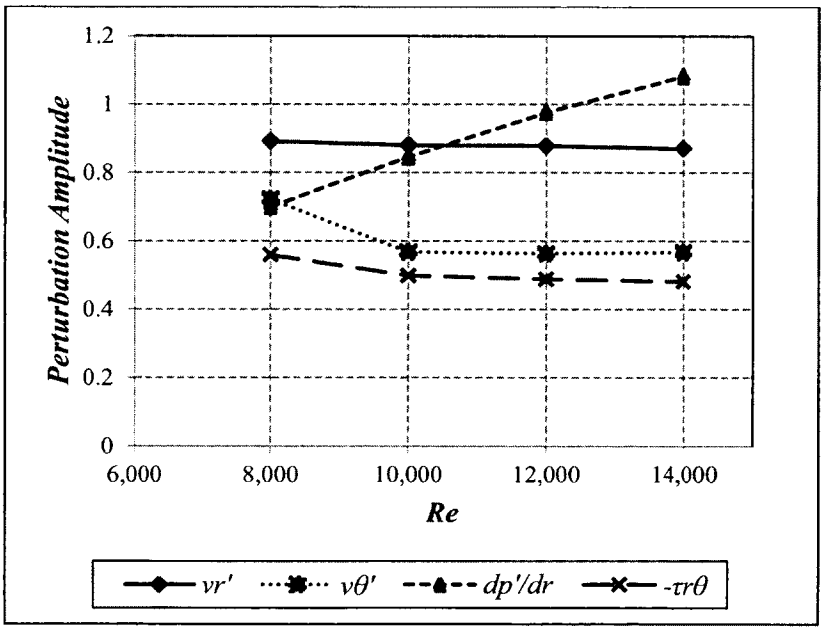

Figure 5.11 Influence of *Re* on the maximum amplitudes of perturbations (ω_R = *0.4, n = 1/2 Np= 2x10*$^{-4}$)

The critical radius for the different perturbation variables is plotted in Figure 5.12, showing that as the Re increased, the critical radius moved farther inside the non-equilibrium pressure zone, approaching the core radius at the highest Reynolds number.

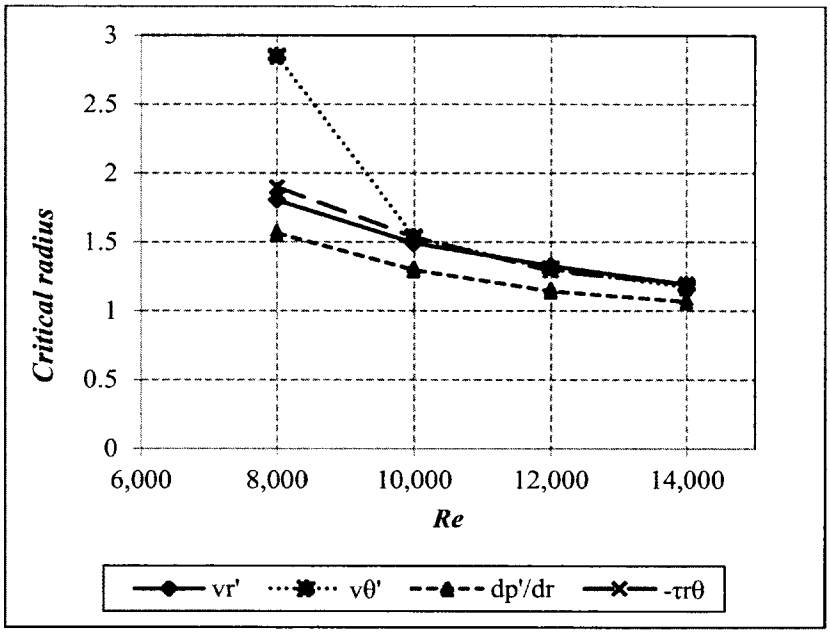

Figure 5.12 Influence of Re on critical radius of perturbations (ω_R = *0.4, n = 1/2 Np= 2x10^{-4}*)

5.5 Effect of perturbation frequency on velocity, pressure and Reynolds stresses

The dimensionless frequency of the imposed perturbations affected the evolution of the perturbation disturbances as demonstrated in Figures 5.13 to 5.16. The frequency of the imposed perturbations was varied between 0.01 and 0.4 at a fixed Reynolds number of 8,000, and an azimuthal mode number of 1/2. Imposed perturbation frequencies above this value are not expected to grow in the flow based on the theory of instability in fluid flows (Schlichting, 1968) the dimensionless form of which requires that,

$$\omega_R < n, \tag{4·15}$$

for instabilities to grow.

Figure 5.13 shows the amplitude variation of the radial velocity perturbations at various frequencies. As can be seen in the figure, the maximum amplitudes occurred in the non-equilibrium pressure zone, while diminishing to zero at both radial extremes. The perturbations in this case occupied a larger radial region as the frequency was increased.

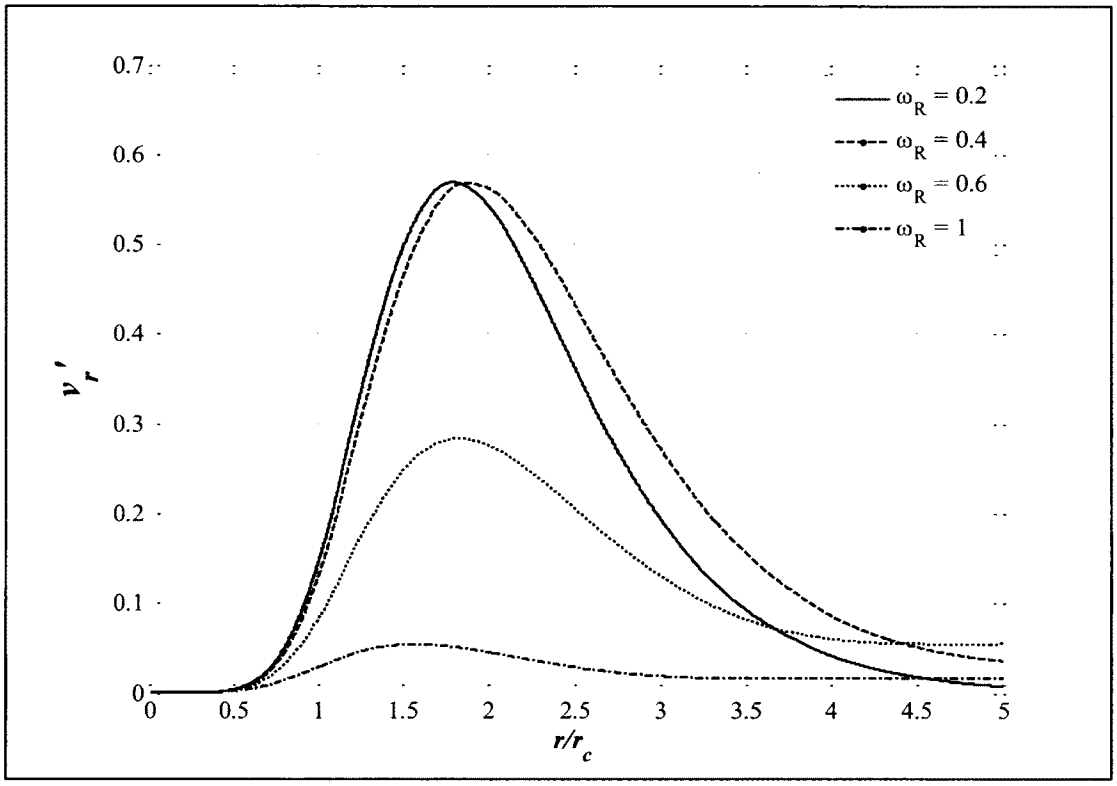

Figure 5.13 The radial velocity perturbation amplitude variation with radius at various frequencies (*n = 1/2 Re = 8,000*)

Figure 5.14 shows that the azimuthal velocity perturbation amplitude was more sensitive to perturbation frequency, increasing from a maximum amplitude slightly under 0.3 at $\omega_R = 0.01$, to just above 0.45 at $\omega_R = 0.4$. The width of the large amplitude zone increased as the frequency was increased.

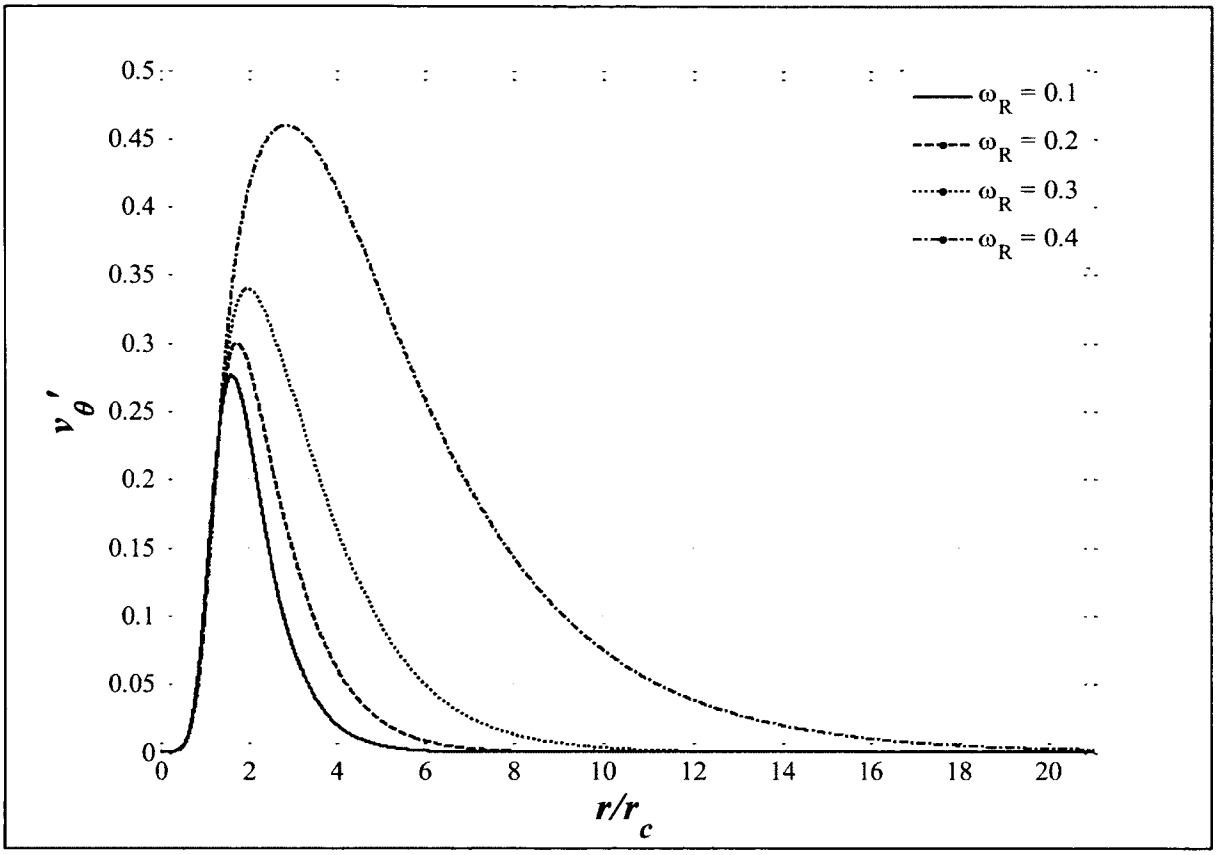

Figure 5.14 The azimuthal velocity perturbation amplitude variation with radius at various frequencies (*n = 1/2 Re = 8,000*)

The amplitude of the perturbed radial pressure gradient is plotted for selected frequencies in Figure 5.15, exhibiting amplitude growth out to the largest radius. Between one and two core radii, there is a jump in the pressure gradient amplitude; this local bulge departed from an otherwise simple curve, then reverted to the monotonically increasing amplitude profile. The local maxima were dependent on the imposed frequency, and the maxima increased with increasing frequency. An explanation of why the overall pressure gradient amplitude curve appears to trend toward a monotonically increasing function will follow in section 6.2.

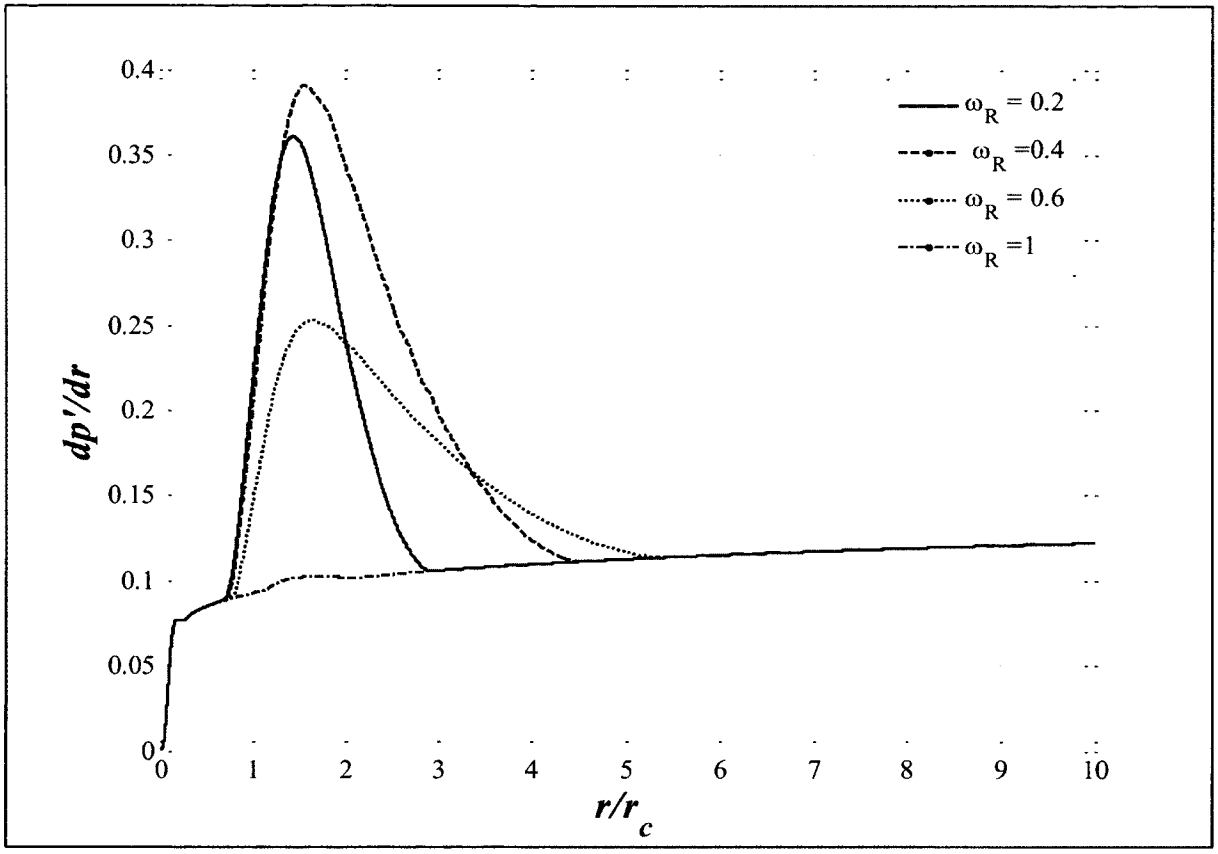

Figure 5.15 Variation of the amplitude of the radial pressure perturbation gradient with radius at various frequencies (*n = 1/2 Re = 8,000*)

The distribution of the $\rho\langle v_r' v_\theta' \rangle$ Reynolds stresses at various frequencies is shown in Figure 5.16, where the stress distributions follow the same trends as the individual velocity components in figures 5.13 and 5.14.

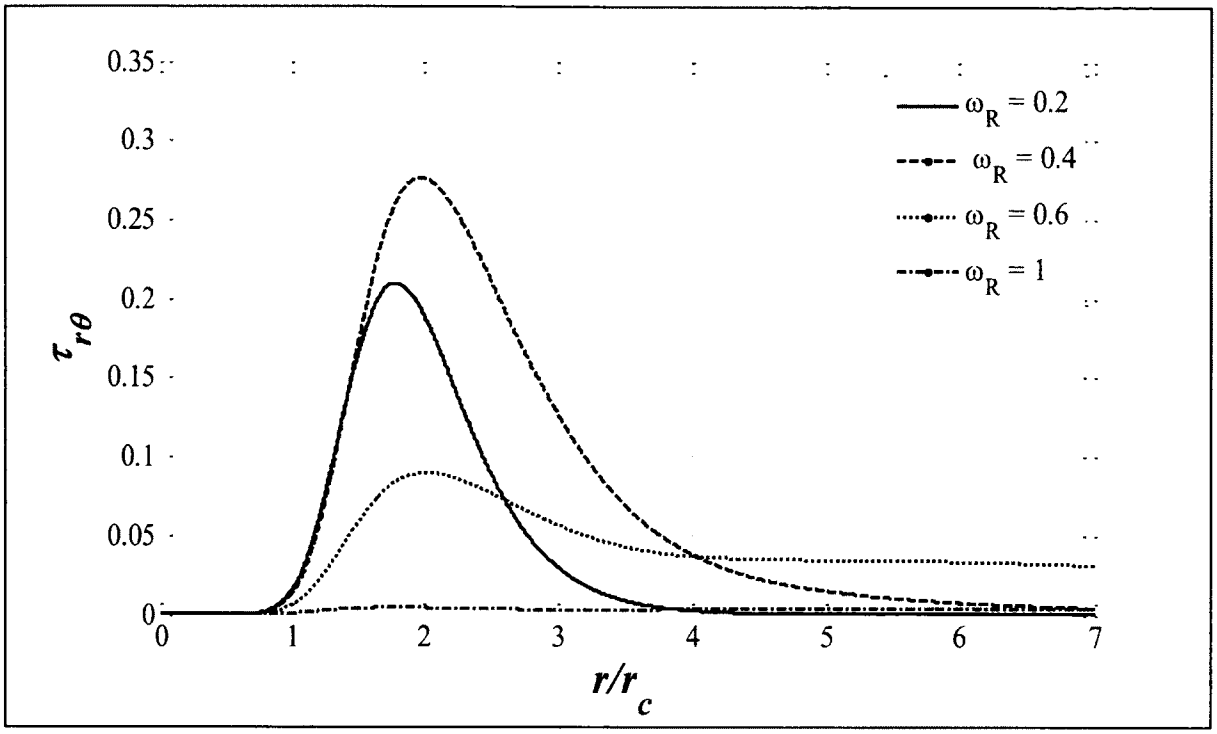

Figure 5.16 The Reynolds stresses variation with radius at various frequencies (*n = 1/2 Re = 8,000*)

5.6 Effect of perturbation frequency on maximum growth and critical radius of perturbations

Figures 5.17 and 5.18 represent the amplitude and location of maximum growth of velocity components, radial pressure gradient perturbation, and $-\rho\langle v_r' v_\theta' \rangle$ Reynolds stress profiles just discussed. In Figure 5.17, the azimuthal velocity component and the Reynolds stress component increased with frequency, while the maximum growth amplitude of the radial velocity component and pressure gradient remained almost unchanged over the range of imposed frequencies, up to a dimensionless frequency of 0.4. At frequencies above 0.4, the perturbed azimuthal velocity amplitude did not diminish, while the perturbations in radial velocity, radial gradient of pressure, and Reynolds stresses decayed rapidly. This decreasing trend indicated that the perturbations at frequencies above 0.4 were over-

damped and showed no growth for this type of flow, confirming to the Schlichting (1968) theory. An exception of this rule appeared to be the azimuthal velocity amplitude.

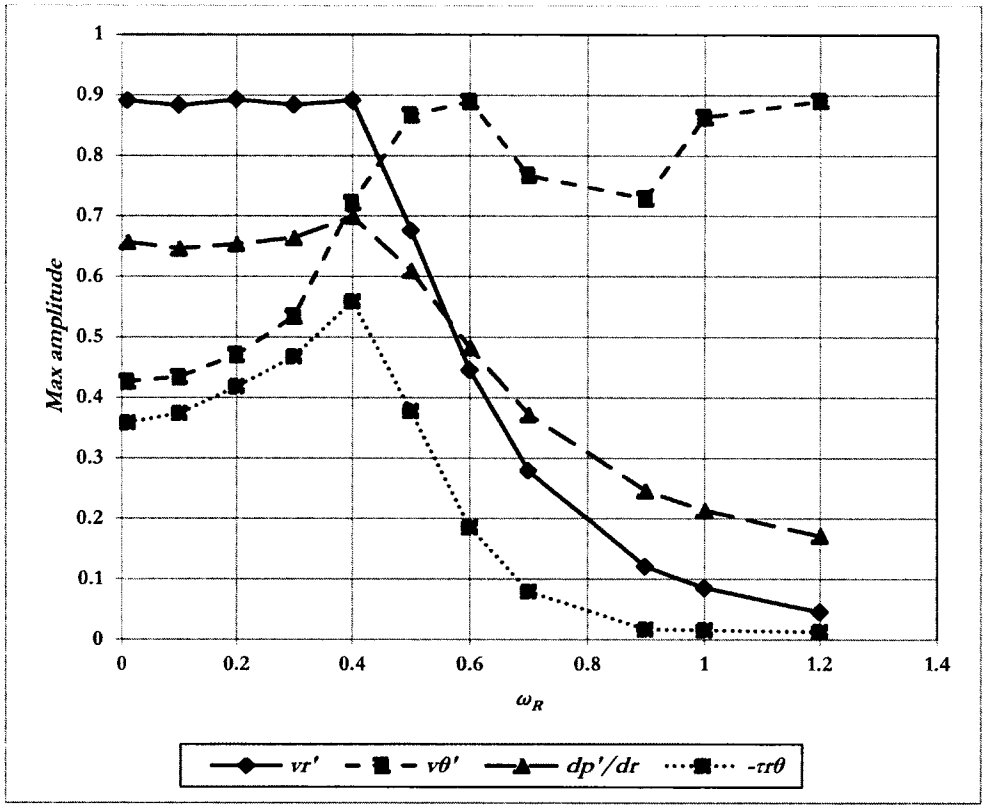

Figure 5.17 The maximum perturbation amplitudes at different frequencies (n = 1/2 Re = 8,000)

Figure 5.18 shows the influence of frequency on the critical radius of the various perturbations. The critical radii were in the non-equilibrium pressure zone, but the critical radius for the azimuthal velocity component migrated toward the outer portion of the non-equilibrium pressure zone for frequencies of 0.4 and above. The migration of the maximum azimuthal velocity amplitude to the outer non-equilibrium region is not necessarily from the physics of the flow. Rather, the instability of the state variable model,

due to the unstable modes associated with the azimuthal velocity component, could be the source. More discussion of this point follows in the stability analysis section 6.2.

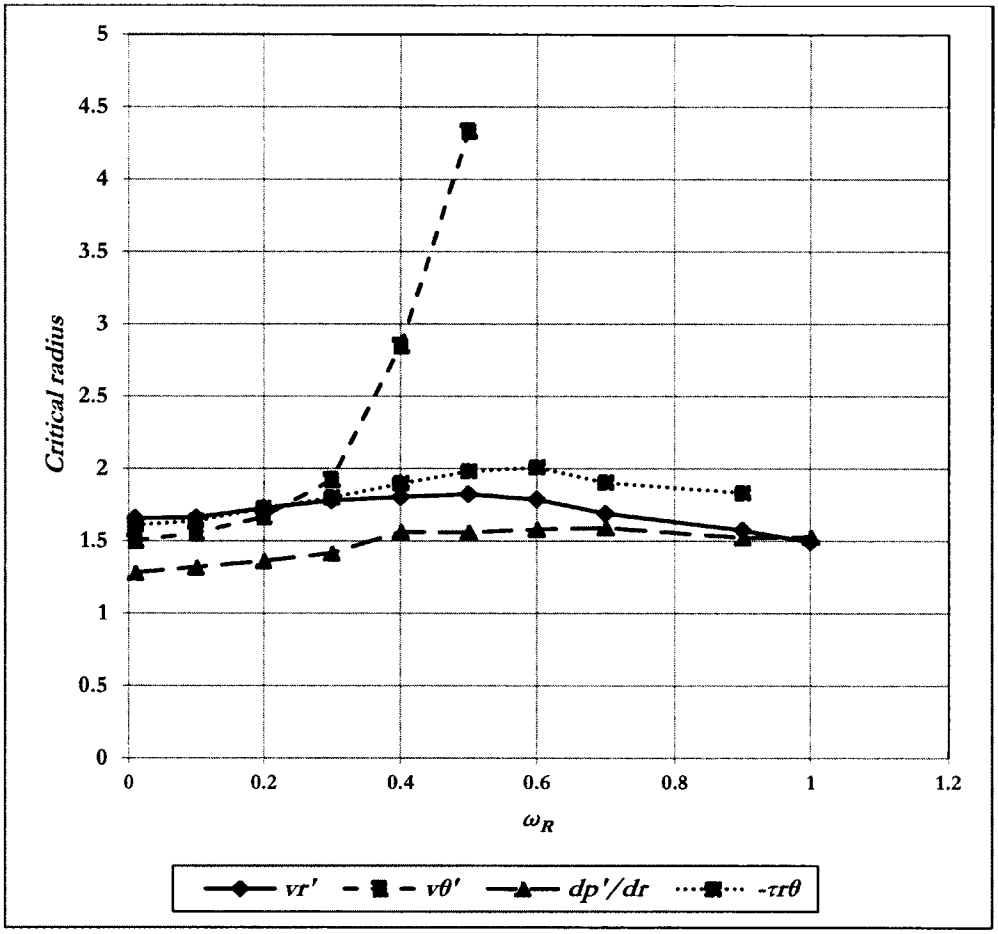

Figure 5.18 The critical radius of perturbation amplitudes at different frequencies (n = 1/2 Re = 8,000)

It was observed that perturbation frequencies between 0.01 and 0.4 had the strongest influence on the azimuthal perturbation velocity component and the $\rho\langle v_r' v_\theta' \rangle$ Reynolds stress. Increasing perturbation frequencies shifted the critical radii of perturbations outward from the core region.

5.7 Effect of imposing different perturbation modes on velocity, pressure and Reynolds stresses

Five azimuthal mode numbers were investigated in this study, the ± 1 modes, which represented helical perturbations waves in the flow; the half mode numbers of $\pm 1/2$ and the symmetric waves resulting from a zero mode number. The mode numbers altered the amplitude profiles, the maximum growth amplitudes and critical radii. In Figure 5.19, the radial velocity amplitude profiles are shown for the different mode numbers. In general, the positive mode number waves had larger amplitudes than the negative modes. The positive mode numbers, ½, and 1, in addition to the symmetric mode, exhibit profiles with singular maxima. The negative mode number profiles had different shapes compared to the positive mode number profiles; there is an inflection point for the -1 mode number, then the profile grew in the outer non-equilibrium pressure zone with an amplitude maximum followed by a decrease in perturbation amplitudes out to five core radii. Unlike other mode numbers, the - ½ and -1 had two amplitude peaks before decaying with increasing radius.

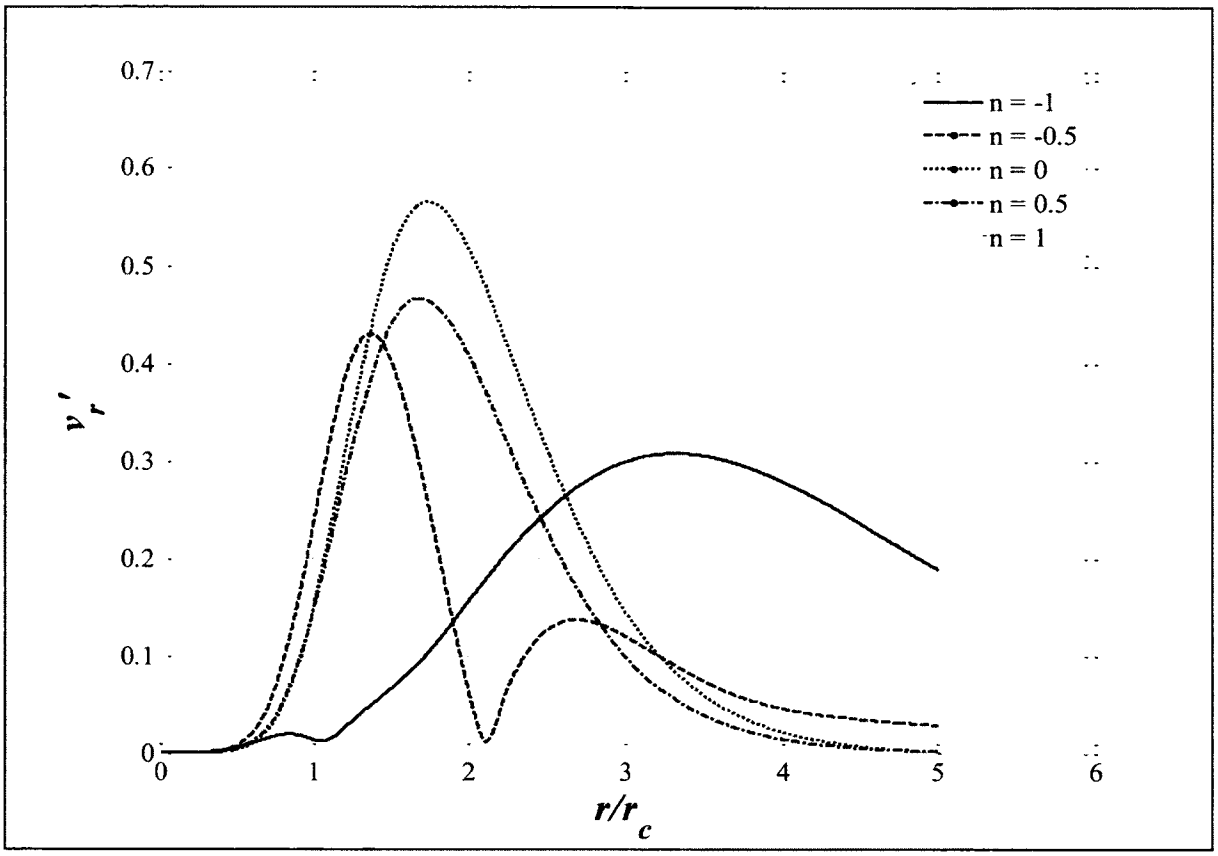

Figure 5.19 The radial velocity amplitude variation with radius at different mode numbers (Re = 8,000 and ω_R = 0.01)

The amplitude variation of the azimuthal velocity for the selected mode numbers are displayed in Figure 5.20. Here, the perturbations for the negative mode numbers had higher amplitudes than the positive ones, in contrast with the radial velocity amplitudes. There is one inflection point for each of the negative mode number profiles (-1 and -1/2). The inflection in the azimuthal velocity profile for the -1 mode number indicated the shift in the amplitude to the outer non-equilibrium pressure zone while the other inflection point for the - ½ mode number exhibited slower velocity amplitude decay rates in the outer non-equilibrium pressure zone.

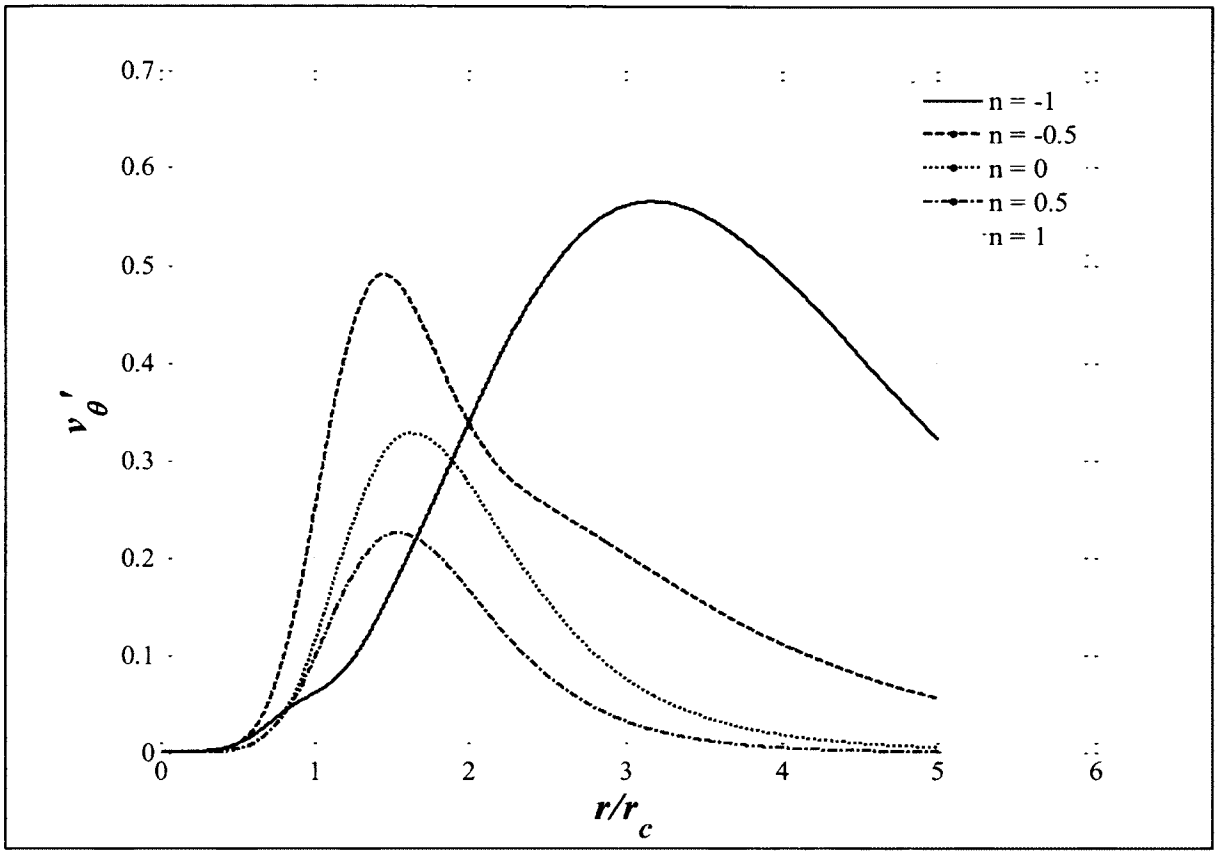

Figure 5.20 The azimuthal velocity profile at different mode numbers (Re = 8,000 and $\omega_R = 0.01$)

The influence of mode number on the radial pressure gradient variation is shown in Figure 5.21. Interestingly, the pressure gradient fell below a value of 0.1 as the outer region was approached for mode numbers -½ , 0, and 1/2. Figure 5.21 showed also that the values of ± 1 could be near a singularity in the numerical formulation, causing the state variable solution to grow unboundedly and it could also be sensitive to the numerical solution technique for those values. Away from the ± 1 mode numbers, the pressure gradient profile exhibited maximum growth inside the non-equilibrium pressure zone followed by rapid decay toward the outer radius. The pressure gradient didn't approach

zero, after five core radii and that could be the surrounding environment effect or a residual solution from the state variable model.

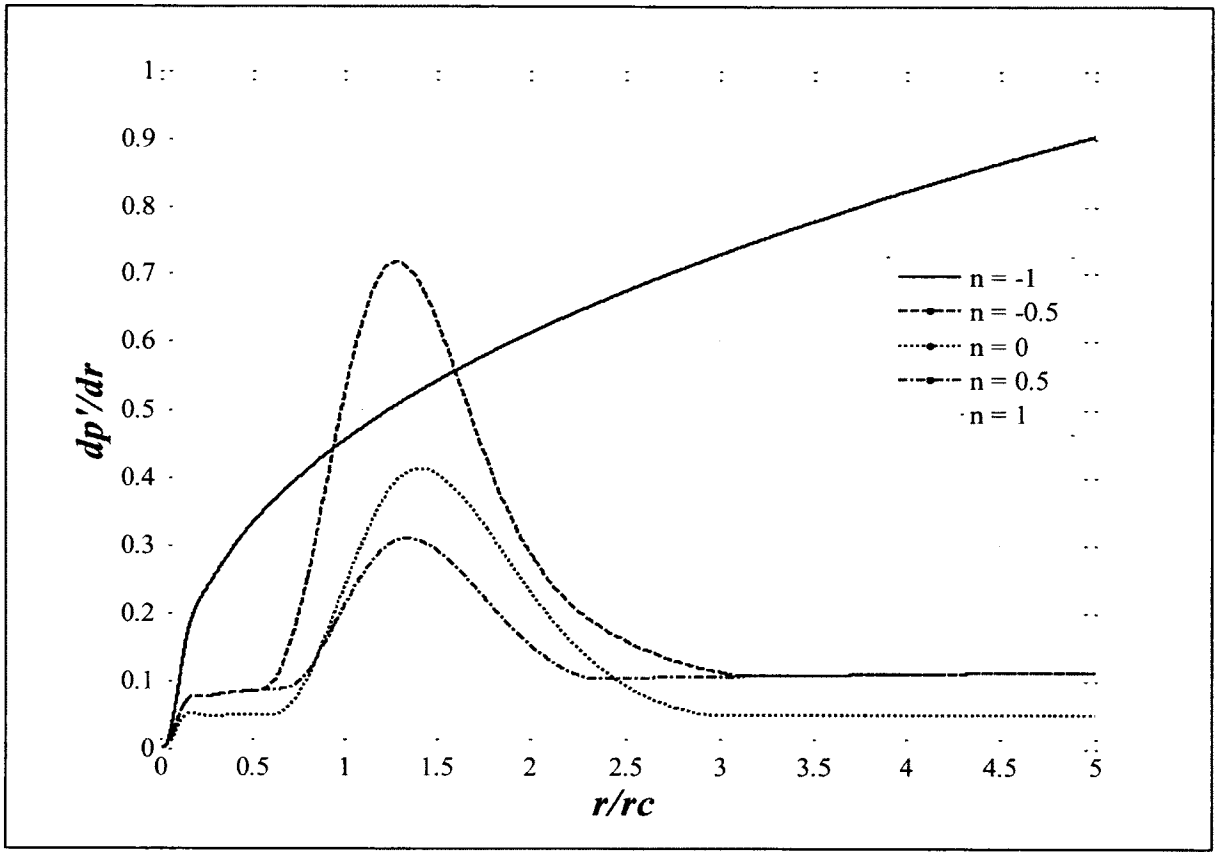

Figure 5.21 The radial pressure gradient at different mode numbers (Re = 8,000 and $\omega_R = 0.01$)

The $\rho\langle v_r' v_\theta' \rangle$ Reynolds stresses profiles at different mode numbers is shown in Figure 5.22. The profiles of mode numbers 0, ½, and 1, had maximum Reynolds stresses at radial locations between one and two core radii. The profile at mode number of – ½ had two peaks and at -1 had one peak outside the non-equilibrium pressure zone.

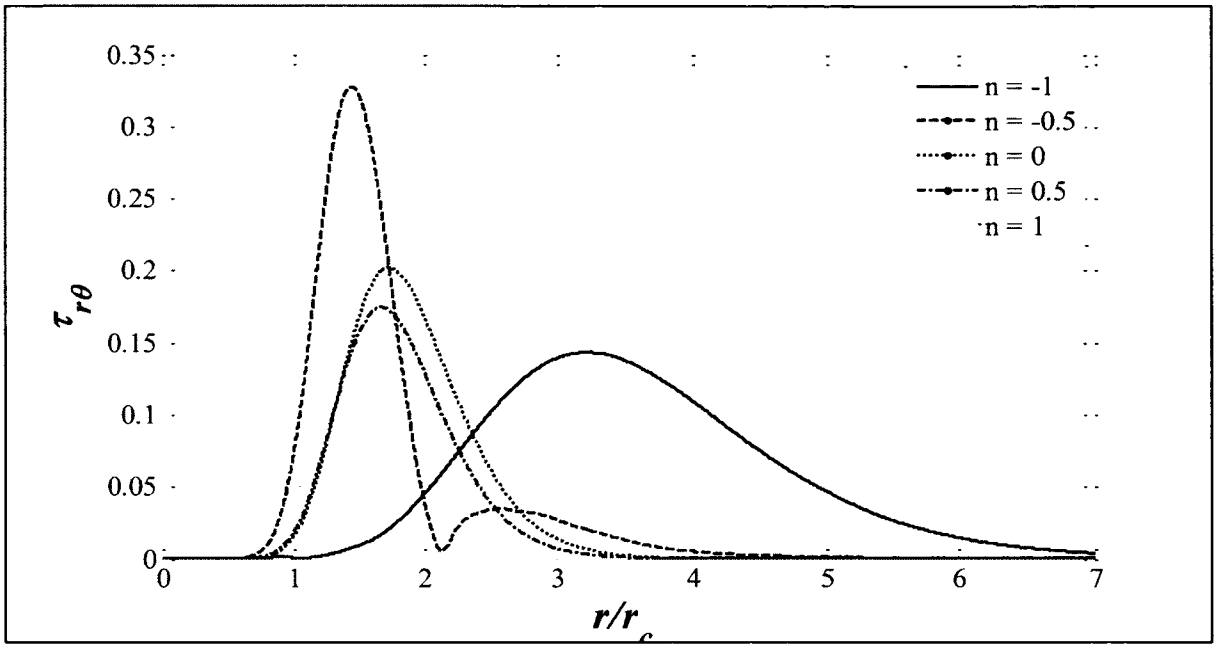

Figure 5.22 The Reynolds stresses variation with radius at different azimuthal modes (Re = 8,000 and ω_R = 0.01)

Hence, the azimuthal mode number of the perturbation changed the shape of the profiles, and three distinct profiles were identified: (1) a simple profile with one maximum within in the non-equilibrium pressure zone and this was the most common profile;(2) a double-peaked profile associated with the -1/2 mode of the radial velocity amplitude and the Reynolds stress component; and (3) a monotonic growth trend for the radial pressure gradient perturbations at ± 1 mode numbers.

5.8 Effect of changing azimuthal number on maximum growth and critical radius of perturbations

The maximum amplitudes and critical radii of the velocity components, radial pressure and Reynolds stress are tabulated for different mode numbers in Table 5.1. The

negative mode numbers in Table 5.1 had azimuthal velocity components and pressure gradient amplitudes that were higher than the corresponding positive modes, while the verse happened for the radial velocity component. The Reynolds stresses didn't follow a specific trend, depending on the radial and azimuthal velocity components, the Reynolds stresses of the negative modes could be higher or lower than the corresponding positive modes. The symmetric (0) mode had maximum amplitudes in the range between the higher and lower values of both the negative and positive modes.

n	v_r'	v_θ'	dp'/dr	$-\tau_{r\theta}$
-1	0.49 (3.2)	0.90 (3)	1.77 (∞)	0.27 (3.1)
-1/2	0.80 (1.3)	0.89 (1.4)	1.39 (1.2)	0.67 (1.37)
0	0.89 (1.7)	0.51 (1.6)	0.68 (1.3)	0.42 (1.7)
1/2	0.89 (1.7)	0.43 (1.5)	0.66 (1.3)	0.36 (1.6)
1	0.90 (1.5)	0.53 (1.5)	1.76 (∞)	0.47 (1.5)

Table 5.1 Maximum perturbation amplitudes at different azimuthal modes (associated critical radius between brackets

The velocity components and the main Reynolds stresses summarized in Table 5.1 had the same critical radii (noted in brackets) within ± 0.1 accuracy for each mode number. When the pressure gradient had a critical radius, the radii were closer to the core radius. zzThe perturbation pressure gradient did not converge for mode numbers of ± 1.

5.9 Summary

The evolution of perturbations in unsteady two-dimensional vortical flow was studied employing the state variable model parameters, varying *Np*, *Re*, ω_R and n. The maximum growth amplitude and location of the associated critical radius were identified for each of the velocity components, the radial pressure gradient and the main Reynolds stress.

In concluding this chapter, the non-equilibrium swirl parameter, *Np*, has a significant influence on the instability of vertical flow. Perturbation amplitudes mostly decreased with increasing *Np*, highlighting the importance of relative humidity in considering the unsteady behavior of axial. The maximum growth of different perturbations as functions of Reynolds number resulted in linear increases in maximum radial pressure amplitude gradient, and movement of critical radii towards the core radius. Also, there is a bulge in the pressure gradient amplitude inside non equilibrium pressure zone. The imposed frequency increases local perturbation maxima at a rate lower than Reynolds number effect. Frequencies above 0.4 were suppressed in the flow. The frequency shifted the critical radius outwards very slightly from the core region. Finally, changing the azimuthal orientation of the perturbations in the flow results three different types of profiles: a common single maximum, a double maximum for $\pm$ ½ modes, and a growing profile for the helical modes $\pm$ 1.

CHAPTER 6

STABILITY ANALYSIS OF THE STATE VARIABLE MODEL

The state variable model, like other numerical approaches for modeling dynamical systems, can be stable within certain limits, based on the parameters used to characterize this vortical flow. A stability analysis of the model based both on the flow physics and the numerics will be discussed in this chapter. At least five factors must be considered in order to assess the stability of the state variable model approach.

Firstly, the present state-variable model simulations have employed a fourth-order Runge-Kutta numerical integration method (RK4), which is the most stable of the integrators. Hence, using RK4 minimizes the possibility of instabilities resulting from numerical integration, but the cost of the numerical computations becomes higher since RK4 uses an intermediate iteration step to control the error coming from the lower order derivative terms in the integration.

Secondly, the highest differential order of the model occurs in the equations governing pressure, since the pressure equations were developed employing the divergence of the conservation of linear momentum, thus making derivatives in those equations higher order than the velocity equations. Solving for the pressure function requires two integration steps, each one with distinct accuracy limitations. In the absence of the non-equilibrium terms, pressure can be isolated from the governing velocity equations; then utilizing a separate state variable scheme to solve for the pressure and enforce constant density. That is not possible for the non-equilibrium pressure equations due to the existence of the coupled velocity-pressure gradient terms.

Thirdly, the pressure function computed using the state variable model exhibited monotonically growing profiles in the large-radius, potential vortex region for some of the cases. Ash and Khorrami (1995) addressed such phenomenon and found a singularity in the unsteady vortex solution because of the unstable modes embedded in the system of equations at the infinite radius limit. The unstable modes can be removed from the solution at the infinite radius limit and an asymptotically stable function results. Then the far field solution can be matched with the inner solution at some radius. This phenomenon was encountered when solving the state variable model for the perturbation pressure outside the non-equilibrium pressure zone, unstable modes of the pressure caused growing profiles. At that region the non-equilibrium pressure forces are small and the associated terms in the governing set of equations are not balanced.

Fourthly, the contracted velocity-pressure terms in the governing equations cannot be totally neglected in the potential vortex region since non-equilibrium pressure gradients are lower order and might not balance the sound production, represented by the model:

$$\eta_P \frac{\partial v_k}{\partial x_i} \frac{\partial P}{\partial x_k} = \left(\eta_V - \frac{1}{3} \mu \right) \frac{\partial}{\partial x_i} \left(\frac{1}{\rho} \frac{D\rho}{Dt} \right)$$

The physics of the flow in that region could be reconsidered by separating the acoustical and non-acoustical features of the flow, writing a closed form state variable for each of the acoustical and non-acoustical systems and then solving the two state variable models for the velocity and pressure fields. Alternatively, for spatial locations beyond five core radii, departures from a potential vortex velocity profile are negligibly small, possibly justifying the complete neglect of non-equilibrium contributions.

Finally, the non-linear characteristics of the original non-equilibrium pressure equations were removed by assuming that the governing equations could be linearized in

the vicinity of the steady-state solution, i.e. linear stability. The elimination of those terms promotes the stability of the state variable model. At the same time, excluding the nonlinear terms washes out part of the physical behavior of the perturbations in the flow. A good future research topic would be to consider the structure of the vortex flow in terms of streaks, rolls, and non-linear secondary structures, if they are present in the flow, and examine how a bifurcation cycle might be described.

6.1 Linear systems stability

The stability of linear systems when disturbed from equilibrium, due to inherent internal or external perturbation sources, can yield conclusions about the behavior of the system without the need to actually solve the system of governing equations. For this vortex system, the time variable is frozen and the state variable model has been advanced in the radial coordinate direction. Stability has been analyzed at each radial step until the assumed boundaries of the flow are reached. It was assumed that detectable vortex flow contributions were not present beyond 15 core radii. At that location the non-equilibrium velocity profile and the potential vortex velocity profile differ by less than 0.5%.

According to stability theory, the system can exhibit one of three possible behaviors: stable, asymptotically stable, or unstable. The stable system starts at the equilibrium point and remains within acceptable tolerances of the equilibrium point, as the integration radius is advanced; the asymptotically stable system departs initially from the equilibrium point but approaches stability at infinite time, and the unstable system never returns to equilibrium once it is disturbed.

There are two types of linear systems: autonomous and non-autonomous. While the coefficients of an autonomous system are not explicitly dependent on the independent integration variable (the radius), the non-autonomous system coefficients are explicitly dependent on radius. From these definitions, the base vortical flow is a non-autonomous system with coefficient matrix [**A**] defined as a function of radius.

6.2 Eigenvalues stability

Mircea Ivanescu (2001) has described an eigenvalue stability test for linear systems based on the position of the eigenvalues of matrix [A] in the complex domain. Linear systems are considered to be stable if all the eigenvalues are to the left of the imaginary axis, i.e. the real parts of the eigenvalues are negative. Otherwise, the systems are unstable. If the eigenvalues fall on the horizontal axis (real axis) then the system is asymptotically stable.

6.2.1 Eigenvalue stability results

An eigenvalue stability analysis of the present state variable model was applied to the state equations for different values of the state variable control parameters (*Re, Np,* ω_R, and n). The eigenvalues were plotted in the complex domain to determine the stability of the system for each parametric case.

The system behaved in different ways as the four vortex parameters were varied. In this section, different levels of the state parameters were chosen based on the results from Chapter 5, and the influence of each parameter on stability was studied separately. At

the end of the section the most important trends have been highlighted. Figures 6.1 through 6.12 permit a stability assessment utilizing the eigenvalue criterion.

6.2.1.1 Reynolds number cases

Reynolds numbers of 8000, 10000, and 12000 have been investigated. For convenience of graph layouts, the eigenvalues were plotted at intervals of one core radius moving outward from the center of the vortex, out to fifteen core radii. Finer radial steps were employed to demonstrate that no fine-scale eigenvalue fluctuations could be detected.

Figure 6.1 shows how the eigenvalues vary with radial location for the radial perturbation velocity amplitude at different Re. The plot shows that the real parts of the eigenvalues at each radial location had the same values for all three Re. At each Re, these positive real parts decreased moving outward from the center, indicating decreased damping of perturbations in the flow, hence the tendency to become unstable. The imaginary part of the eigenvalues increased with increasing Reynolds number at the prescribed locations, increasing the possibility of higher frequency perturbations.

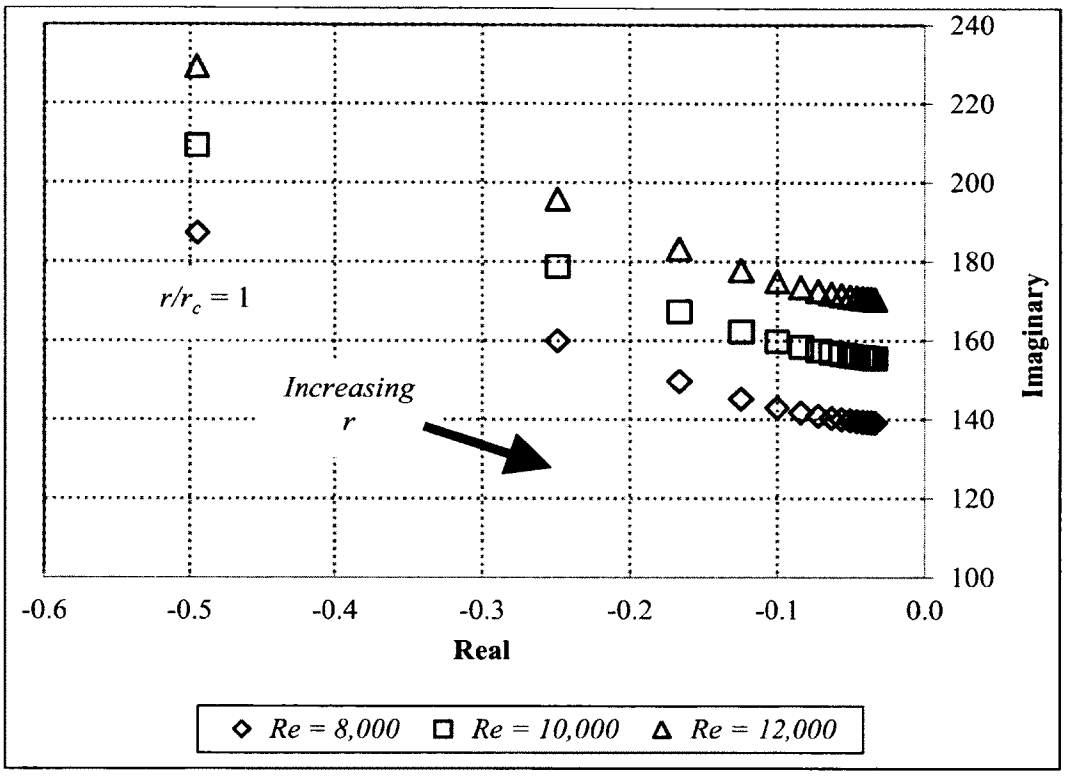

Figure 6.1 Representation of radial velocity eigenvalues in the complex domain at different Reynolds numbers

The azimuthal velocity eigenmode migration, shown in Figure 6.2, has stable modes within three radii of the core since the non-equilibrium and viscous forces are in balance. The stable eigenvalues have migrated toward the complex axis for increasing r, resulting in less damping at lower frequencies. Beyond three radii, unstable eigenmodes with positive real-parts are observed since the non-equilibrium forces are weak and the region is assumed to be a potential flow. The magnified view of those modes in Figure 6.2 shows migration of the eigenmodes towards the horizontal axis and being very close to that axis demonstrates that they are asymptotically stable.

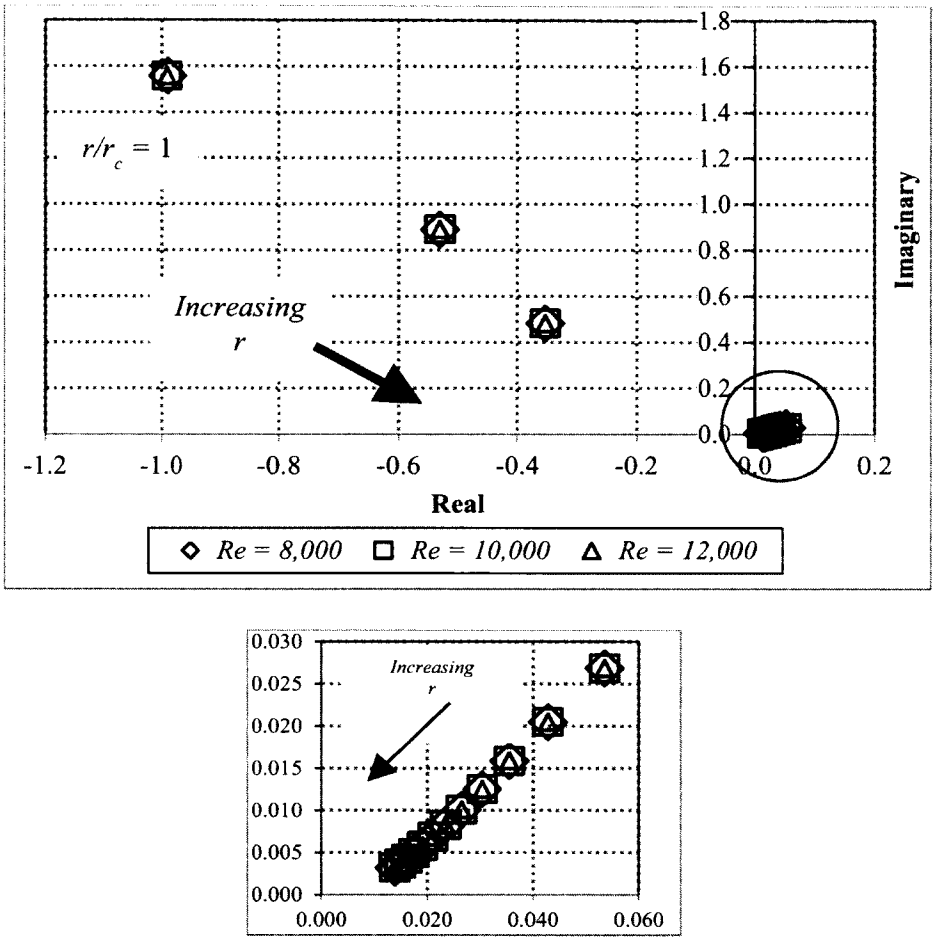

Figure 6.2 Representation of azimuthal velocity eigenvalues in the complex domain at different Re

Figure 6.3 indicates that the radial pressure gradient amplitudes have unstable modes at the first three radial locations. The pressure relaxation and viscous stresses are in balance within this region, but imposing perturbations in the flow will cause unstable pressure modes and bulges as seen in Figures 5.1, 5.9, and 5.15, in order to restore the stability of the vortex flow. For the outer region ($r_c > 3$), the pressure eigenmodes had negative real-parts, hence they are stable. The Reynolds number hardly affects the eigenvalues for the azimuthal velocity amplitude (Figure 6.2) and the radial pressure gradient amplitude (Figure 6.3).

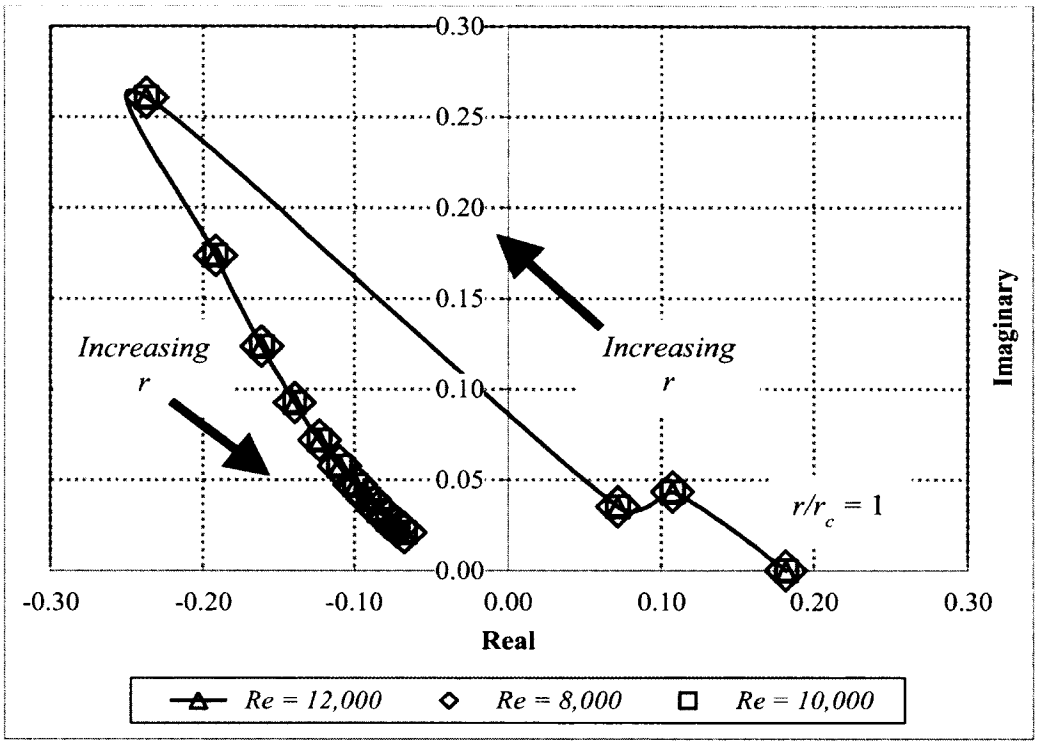

Figure 6.3 Representation of radial pressure gradient eigenvalues in the complex domain at different Reynolds numbers

6.2.1.2 Swirl parameter cases

Figure 6.4 through 6.6 represents the eigenmodes of the perturbations at four values of non-equilibrium swirl parameter (1, 2.5, 5, 10)x10^{-4} selected based on the experimental range of the swirl parameter $10^{-4} < Np < 10^{-3}$ (see section 5.1). Figure 6.4 shows the eigenmodes of the radial velocity amplitude for the four values of Np. The eigenvalues at each radial location have the same real-parts, while their imaginary parts change only by a small amount. Hence, the expected perturbation outputs were expected to be nominally at the same frequencies. The swirl parameter hardly influenced the eigenmodes for the experimentally verified range.

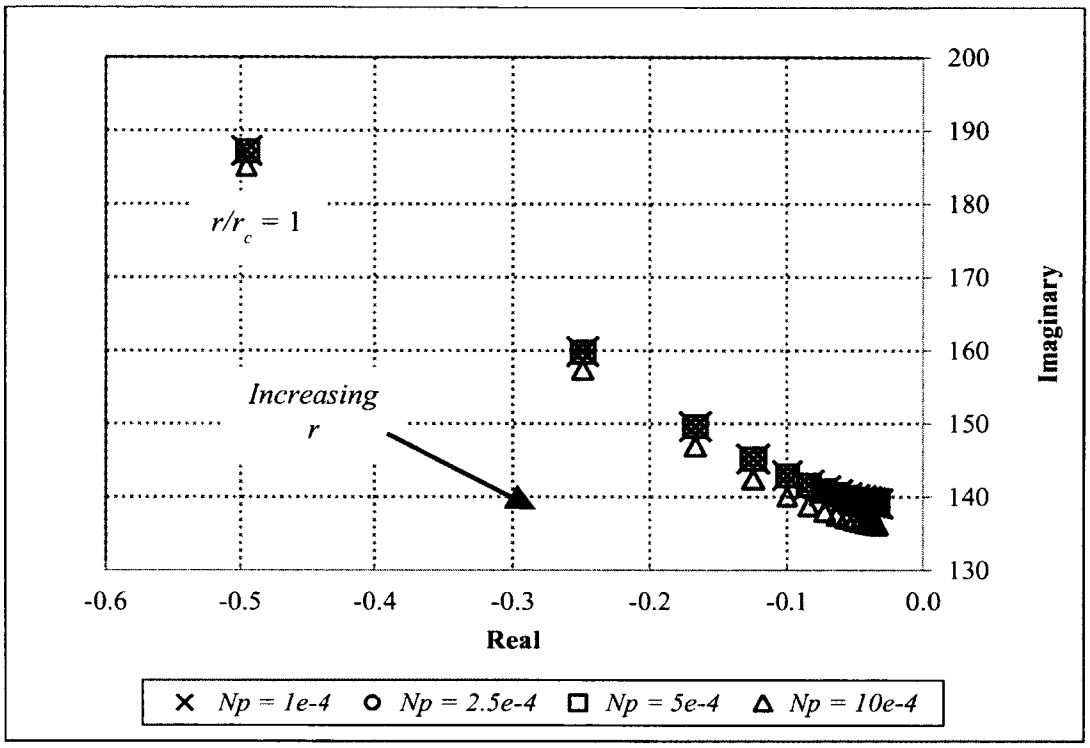

Figure 6.4 Representation of radial velocity eigenvalues in the complex domain fort different non-equilibrium swirl parameter *Np*

The number of stable modes in the azimuthal velocity amplitude in Figure 6.5 increased as *Np* increased, indicating stable behavior over a wider radial range. This indicates that the non-equilibrium pressure envelope becomes wider as *Np* increases. The width of the non-equilibrium envelope ranges between three and five core radii from the vortex centerline. Conversely, the number of stable modes of radial pressure gradient decreased as *Np* increased (Figure 6.6).

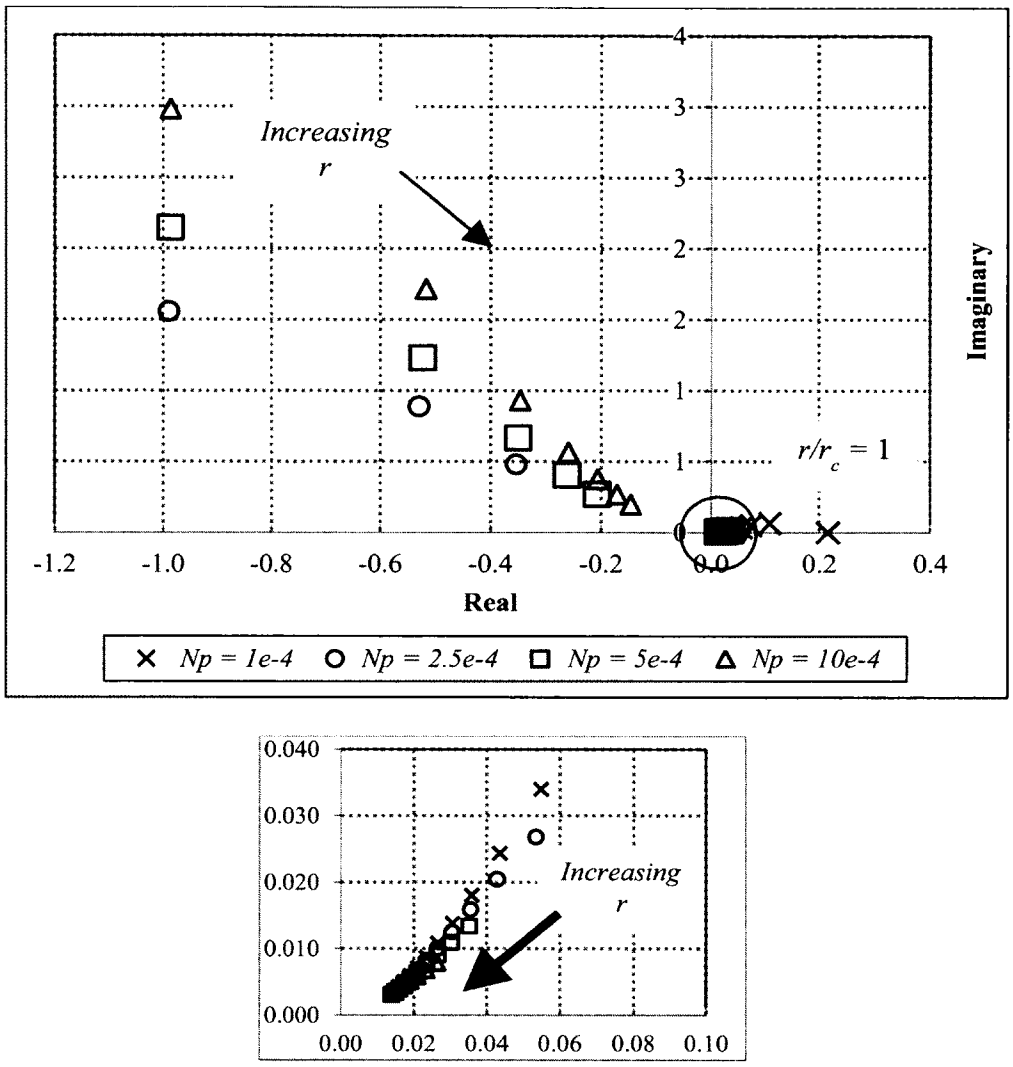

Figure 6.5 Representation of azimuthal velocity eigenvalues in the complex domain for different values of non-equilibrium swirl parameter *Np*

Figure 6.6 also shows that for higher *Np*, more unstable modes of radial pressure gradient amplitudes are created in the inner region of the flow so as to stabilize the velocity profiles. All the eigenmodes are stable for $Np = 1\text{x}10^{-4}$ indicating the stability of the flow. As *Np* increases, unstable modes are revealed within the inner region of the vortex flow, and at $Np = 1\text{x}10^{-3}$ the unstable modes span most of the flow region.

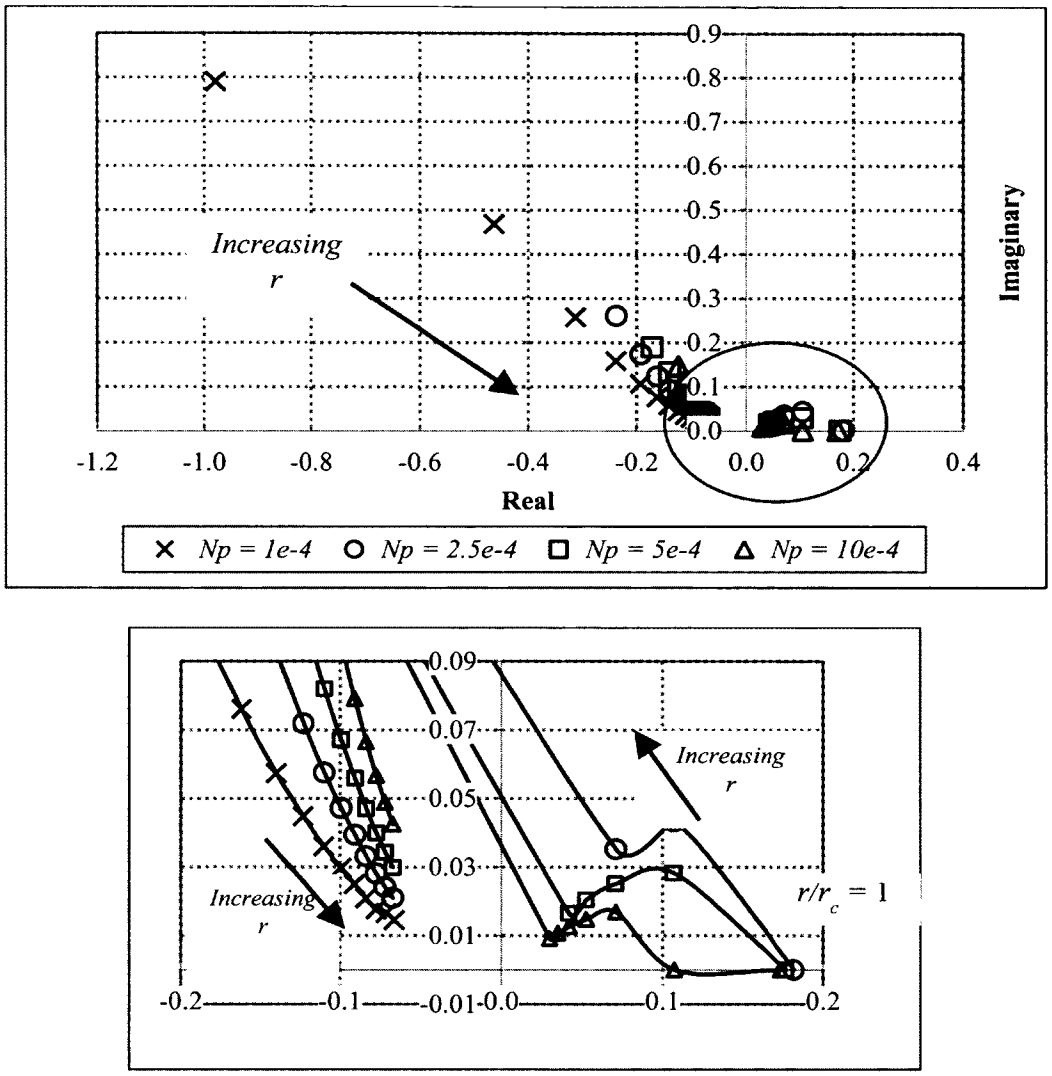

Figure 6.6 Representation of radial pressure gradient eigenvalues in the complex domain at different *non-equilibrium swirl parameter Np*

6.2.1.3 Perturbation frequency cases

State variable stability was investigated at five non-dimensional perturbation frequencies (0.1, 0.3, 0.5, 0.7, and 0.9). The eigenvalues characterizing the radial velocity are shown in Figure 6.7, where the real parts of these eigenvalues were globally the same, while the imaginary parts increased with frequency until a dimensionless frequency of 0.7 was reached, remaining constant thereafter.

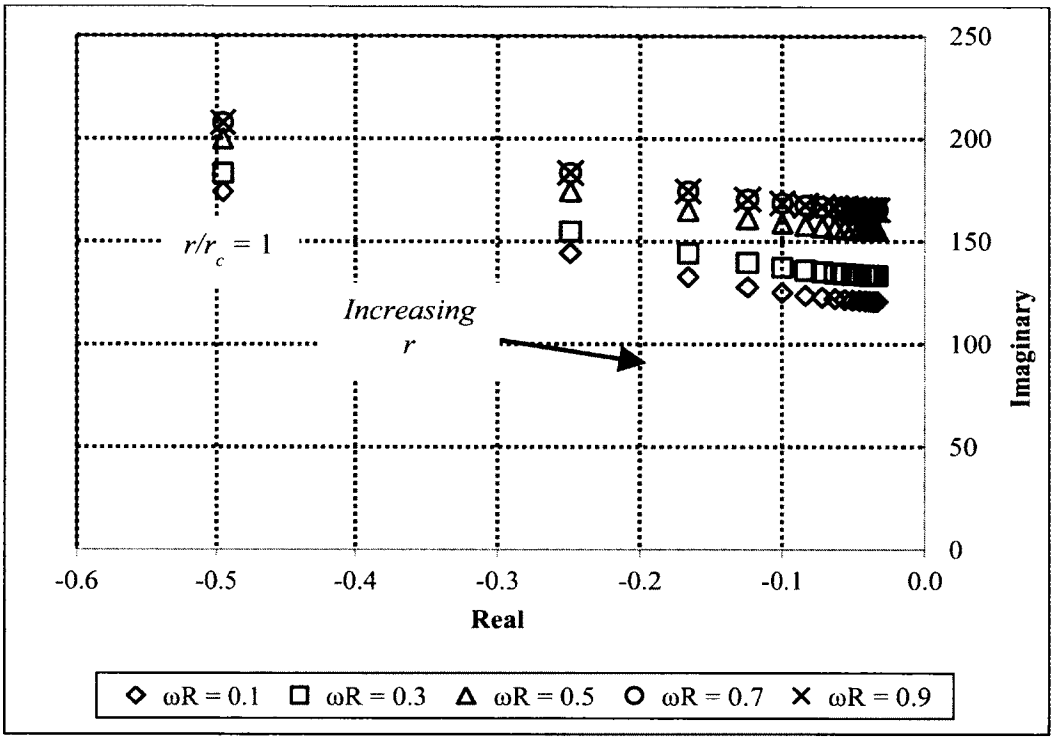

Figure 6.7 Representation of radial velocity eigenvalues in the complex domain at different ω_R

The azimuthal eigenmodes for the selected dimensionless frequencies are displayed in Figure 6.8. The azimuthal velocity had the same eigenmodes for all of the dimensionless frequencies. There are three stable modes in the inner region of the flow ($r_c \leq 3$) due to the non-equilibrium pressure envelope suppression of the instabilities, thereby causing the velocity profiles to be stable. Moving radially outward, the non-equilibrium pressure gradient forces diminish and unstable numerical modes are exposed because of the very small values of the determinant of matrix [A].

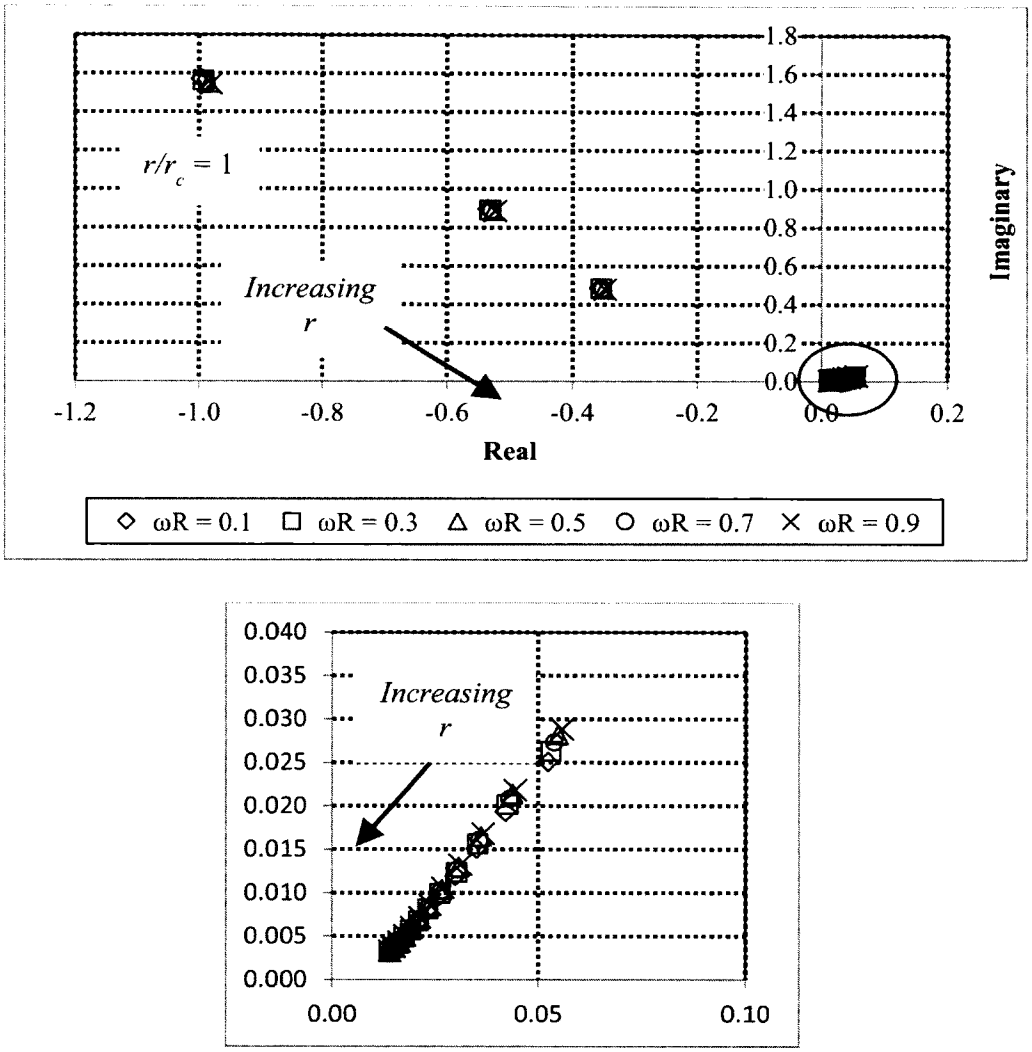

Figure 6.8 Representation of azimuthal velocity eigenvalues in the complex domain at different ω_R

Figure 6.9 shows that the pressure gradient amplitude has three unstable modes located in the inner region between one and three core radii, jumping to stable modes for larger r. The eigenmodes were not affected by the frequency. The unstable modes resulted in the local peaks in the pressure gradient amplitude profiles plotted in Figures 5.1, 5.9, and 5.15, in order to restore the stability of the vortex flow. The induced pressure gradient due to perturbations in the flow stabilized the velocity profile inside the non-equilibrium

pressure zone. Outside the non-equilibrium pressure zone, stable pressure gradient eigenmodes are dominant ,but their real parts decreased moving outward, indicating decreased damping in that region which produced the slowly-growing pressure amplitude profiles shown in Figures 5.1, 5.9, and 5.15.

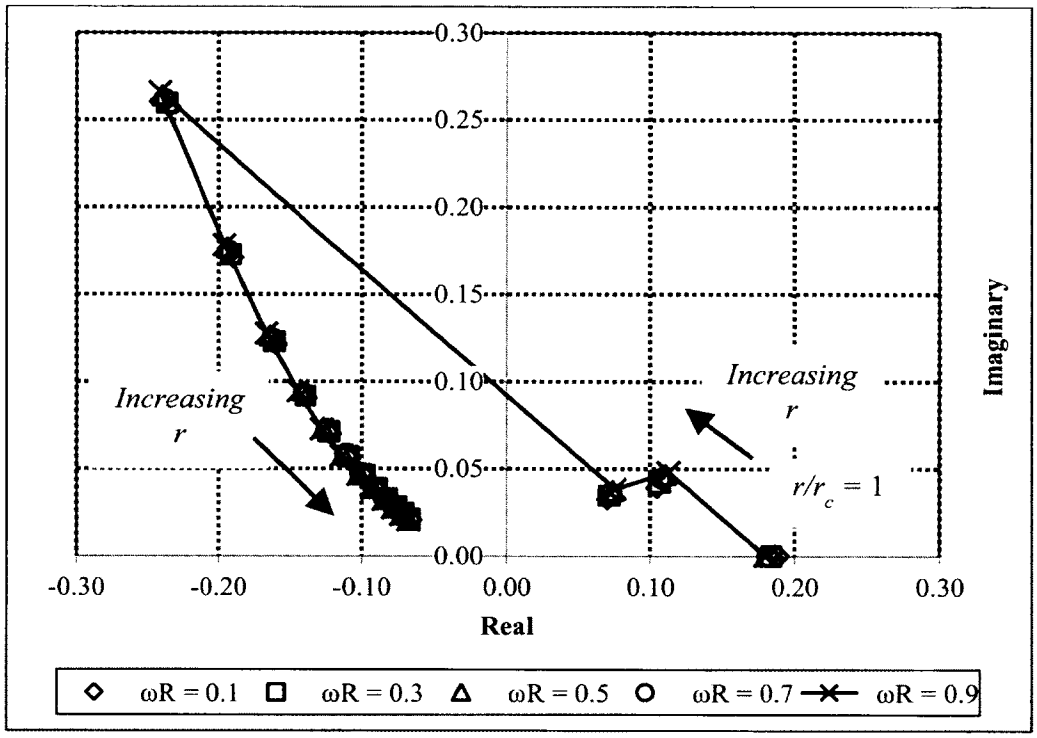

Figure 6.9 Representation of radial pressure gradient eigenvalues in the complex domain at different ω_R

6.2.1.4 Azimuthal mode cases

Five azimuthal mode numbers (-1, - ½, 0, +½, and +1) were investigated. The eigenvalues for the radial velocity are displayed in Figure 6.10, exhibiting the same real parts at each radial location. The imaginary parts varied depending on the mode number; the highest frequencies were found for the ± 1 modes, the lowest occurred for the

symmetric case n = 0, and the half modes were between the integer modes and the symmetry modes. Also, the positive azimuthal orientation of the perturbations in the flow resulted in higher frequencies than for the negative mode numbers.

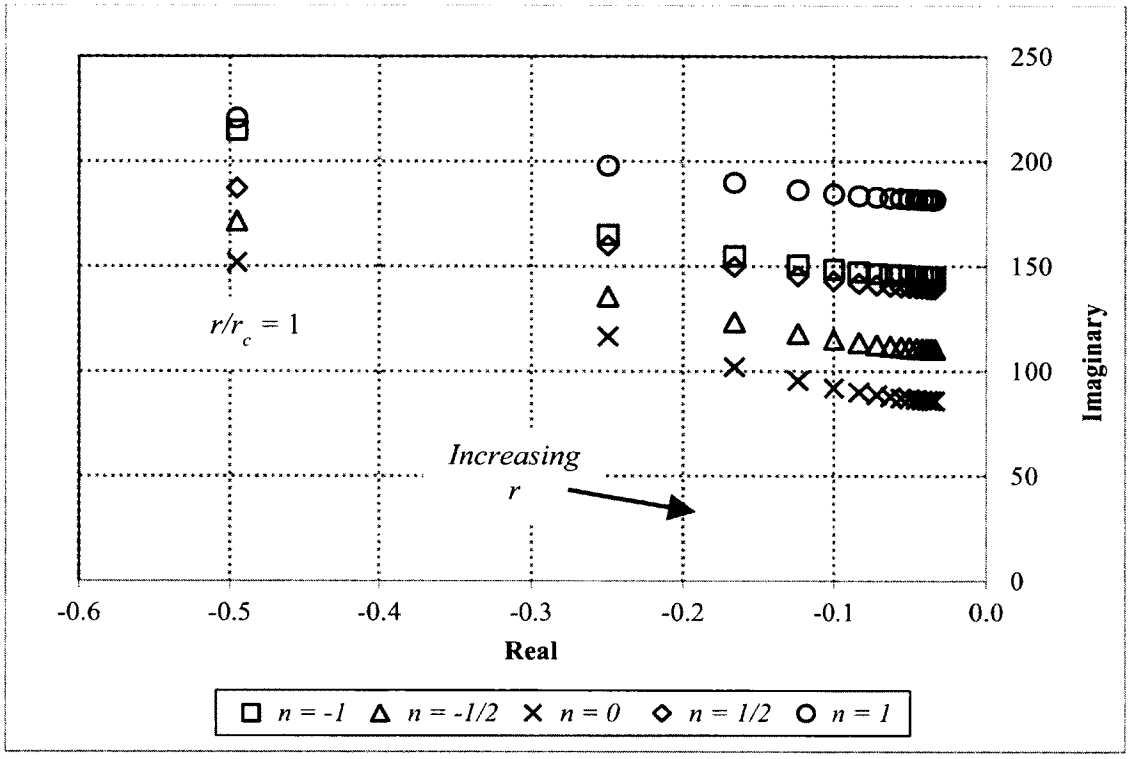

Figure 6.10 Representation of radial velocity eigenvalues in the complex domain at different mode numbers

Figure 6.11 represents the eigenvalues of the azimuthal velocity component at different mode numbers. The ± 1 modes were unstable throughout the whole flow field; those are helical modes causing instability in the vortical flow. The symmetrical modes (n = 0) had asymptotically stable modes with the least damped modes in the outer flow region. The 1/2 modes have stable eigenmodes in the inner region of the vortex, due to the non-equilibrium pressure gradient forces suppressing the instabilities. The unstable modes

appear outside the non-equilibrium region ($r_c \geq 3$), and had relatively small positive real parts, exhibiting virtually no growth (Figure 5.20). The unstable modes become asymptotically stable as the outer potential flow region is approached.

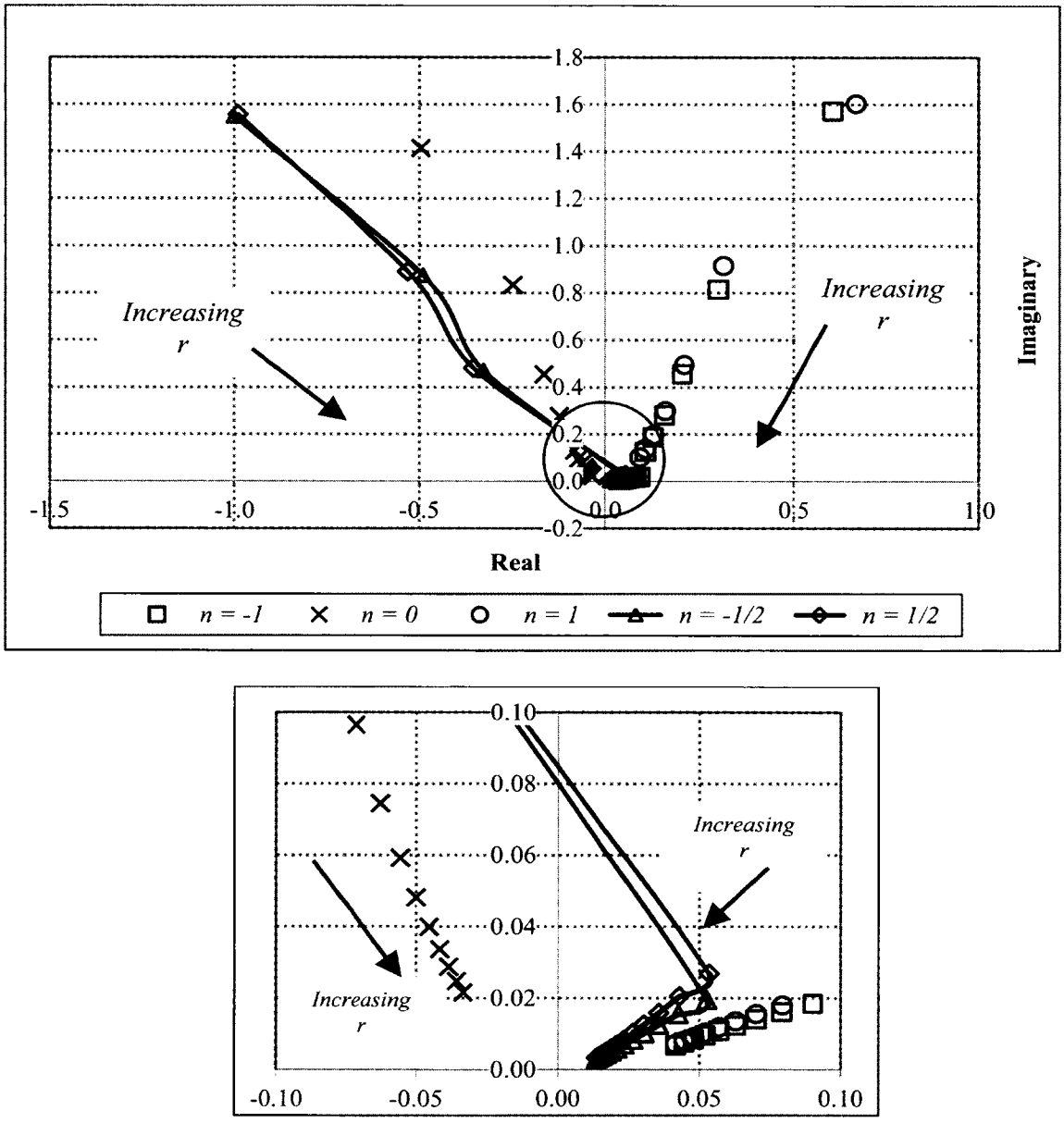

Figure 6.11 Representation of azimuthal velocity eigenvalues in the complex domain at different mode numbers

Figure 6.12 represents the radial pressure gradient amplitude eigenvalues for the different mode numbers. Unlike the azimuthal eigenvalues, the ± 1 modes were stable throughout the flow field, and the pressure profiles have no local bulges inside the non-equilibrium zone (Figure 5.15), suggesting that the unstable helical mode structures might be different from the structures characterizing the other modes, and evolution of those helical modes in the flow require further study employing different time and spatial scales. The symmetrical case, $n = 0$, has asymptotically stable modes with the least-damped modes in the outer flow region. The eigenmodes for $n = \pm ½$ were unstable in the inner core region, balancing the perturbation stresses in that region. Stable eigenmodes were observed in the outer region, with asymptotic stability at $n = -½$.

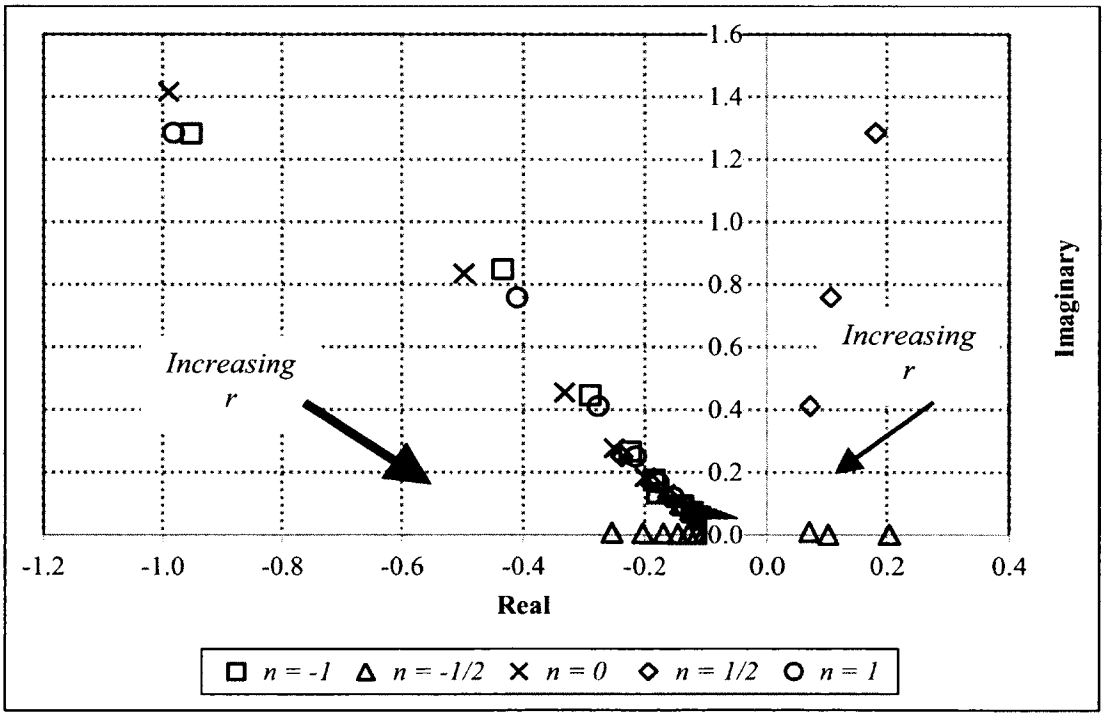

Figure 6.12 Representation of radial pressure gradient eigenvalues in the complex domain at different mode numbers

In conclusion, instabilities created by the imposed perturbations in the flow region for $r_c \leq 5$, appear to interact with the non-equilibrium pressure gradient forces, resulting in significant Reynolds stress components in the flow (Figure 5.4), which could be a new type of turbulent structure. The eigenvalue stability analysis predicted unstable eigenmodes associated with the pressure, within the non-equilibrium pressure zone, suppressing the perturbations and keeping the velocity profiles stable. Further investigation of non-equilibrium pressure-turbulent stress interactions at higher Re is strongly recommended.

6.3 Equilibrium points

An important linear system stability parameter is the equilibrium point, defined as the solution to state equations when the right hand side of its general form is zero. Recalling the general form of the state equations:

$$\frac{d\chi}{dr} = \mathbf{A}\chi + \mathbf{B}u = f(\chi, u, r) \tag{6.1}$$

where χ is the state variable vector, [**A**] is the Jacobian matrix, [B] =***I***, and u is the initialization input for the system. Setting the left hand side of this equation equal to zero,

$$\frac{d\chi}{dr} = f(\chi^*, u^*) = 0$$

where χ^* is the equilibrium state variable vector and u^* is a constant initial input.

The equilibrium points χ^* remain unchanged as radius is advanced for stable systems. The vortical flow system can have one-, multiple-, or no-equilibrium points.

6.4 Lyapunov stability

According to Lyapunov stability theory (Vidyasagar, 2002), the stability of linear systems around their equilibrium states can be assessed directly from the matrix of coefficients, [A]. Based on its properties, the system could be stable, asymptotically stable, or unstable. The linear system is stable around its equilibrium points if the following integration is bounded,

$$\int_{r_o}^{r} \lceil \mathbf{A}(r) \rceil dr \leq \rho$$

where ρ is some constant and $\lceil \ \rceil$ is a suitable *matrix measure*.

The equilibrium state becomes asymptotically stable if the integration,

$$\int_{r_o}^{r} \lceil \mathbf{A}(r) \rceil \cdot dr \to -\infty \text{ as } t \to \infty$$

and the equilibrium state is unstable if the integration is unbounded, i.e.

$$\int_{r_o}^{r} \lceil \mathbf{A}(r) \rceil \cdot dr \to \infty \text{ as } t \to \infty$$

The value of the constant, ρ, depends on the system domain of influence. For this vortical flow an integration limit of 15 core radii was chosen, since detectable traces of the non-equilibrium velocity contributions cease to exist beyond this limit.

6.4.1 Matrix measures

While the norms of matrices must be non-negative, the matrix measures can have negative as well as positive values. Table 6.1 (Vidyasagar, 2002) shows examples of three main types of vector norms and the corresponding matrix norms.

	Norm	Vector (x) norm	Matrix (**A**) norm	Matrix (**A**) measure
1	Norm ∞	$\|\mathbf{x}\|_\infty = \max_i \|x_i\|$	$\|\mathbf{A}\|_\infty = \max_i \sum_{j=1}^{n} \|a_{ij}\|$	$\lceil \mathbf{A} \rceil_\infty = \max_i \left(a_{ii} + \sum_{j \neq i}^{n} \|a_{ij}\| \right)$
2	Norm 1	$\|\mathbf{x}\|_1 = \sum_{i=1}^{n} \|x_i\|$	$\|\mathbf{A}\|_1 = \max_j \sum_{i=1}^{n} \|a_{ij}\|$	$\lceil \mathbf{A} \rceil_1 = \max_j \left(a_{jj} + \sum_{i \neq j}^{n} \|a_{ij}\| \right)$
3	Norm 2	$\sqrt{\sum_{i=1}^{n} \|x_i\|^2}$	$\|\mathbf{A}\|_2 = \sqrt{\lambda_{\max} [\mathbf{A} \times \mathbf{A}^*]}$	$\lceil \mathbf{A} \rceil_2 = \frac{\lambda_{\max} [\mathbf{A}^* + \mathbf{A}]}{2}$

* λ is the eigenvalue

Table 6.1 Vector and matrix norms

The relation between the matrix norm and the matrix measure is,

$$-\|\mathbf{A}\| \leq \lceil \mathbf{A} \rceil \leq \|\mathbf{A}\| \tag{6.2}$$

The upper and lower values of the real-parts of the eigenvalues can be estimated using matrix measures rather than norms, since eigenvalues have both negative and positive signs. The following property of matrix measures can be used for such estimation (Vidyasagar, 2002),

$$-\lceil -\mathbf{A} \rceil \leq \mathrm{Re}_\lambda \leq \lceil \mathbf{A} \rceil \tag{6.3}$$

6.4.2 The integration $\int_{r_o}^{r} \lceil \mathbf{A}(r) \rceil \cdot dr$

For the Lyapunov stability assesment of the present vortex state, the second matrix measure (Table 6.1) was computed at each radial step. The resulting matrix measure was a function of radius, and was integrated numerically out to 15 core radii using an RK4 solver.

6.4.3 Lyapunov stability results

The Lyapunov stability criterion was applied for different values of the flow parameters (*Re, Np, ω_R, n*). The second matrix measure $\lceil \mathbf{A} \rceil_2$ (Table 6.1) was used in the integration of the Lyapunov function $\int_{r_o}^{r} \lceil \mathbf{A}\bar{r} \rceil \cdot dr$. The second matrix measure was evaluated at integer radius steps, starting at $r_c = 0.01$ (because of the potential singularity of the flow at $r_c = 0$), out to $r_c = 15$. Random intermediate points (between the incremental radius steps) were also evaluated to ensure that the functional behavior was continuous. The derivative of the second measure was always negative, over the flow range studied. The second matrix measure at "infinite radius" (15 core radii), approached a constant value for each parameterized flow case, and that value was chosen as a zero reference, in order to interpret the matrix measure values in the inner region.

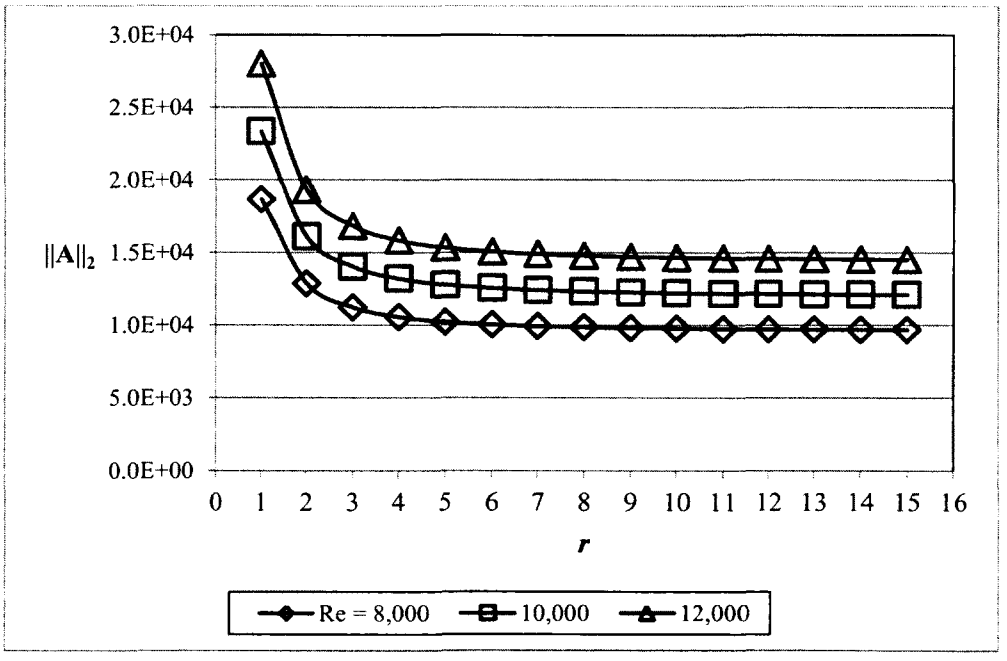

Figure 6.13 the second measure of matrix [A] variation with Re

Figure 6.13 shows the variation of the second measure of matrix [A] with Reynolds numbers of 8000, 10000, and 12000. The matrix measure decreases, moving outward radially, and approaches a constant value asymptotically, beyond approximately six core radii. The stability measure increased with increasing Reynolds number indicating that the flow moved toward instability.

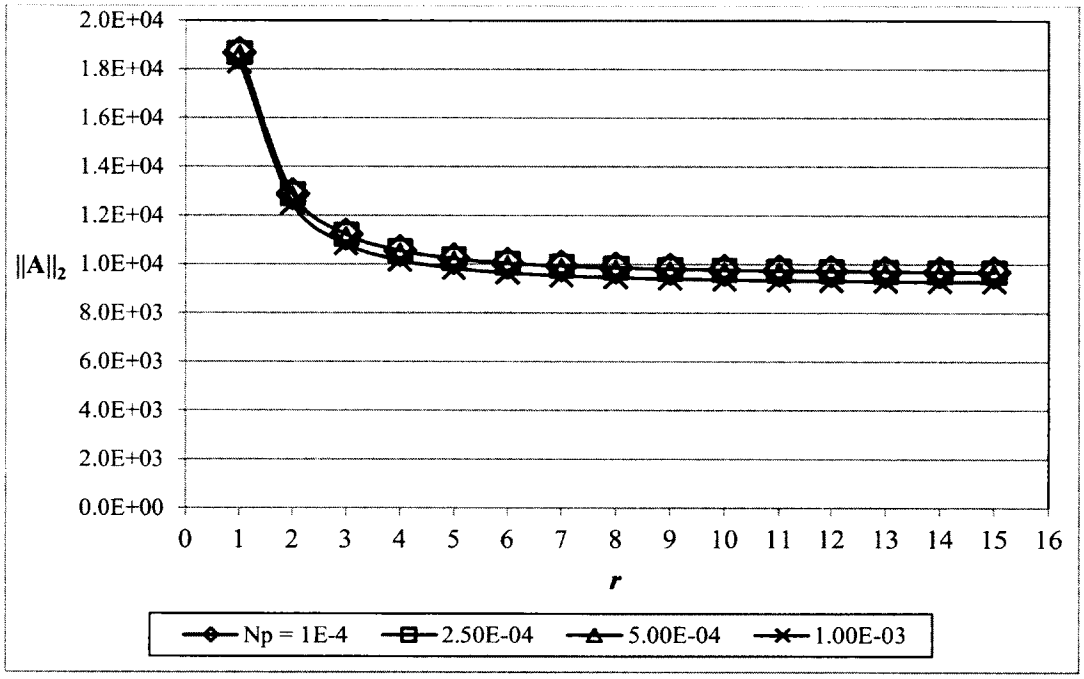

Figure 6.14 the second measure of matrix [A] variation with *Np*

Figure 6.14 shows that the swirl parameter, *Np*, hardly affects the stability of the flow over the range $1x10^{-4}<Np<1x10^{-3}$. The results shown in this figure were generated using the same Reynolds number, and with the stability measure been unchanged through *Np*; suggesting that

varying *Np* at the same Re would not affect the stability of the flow, only the width of the non-equilibrium pressure region will be affected as the eigenvalue criterion showed (Section 6.2.1.2).

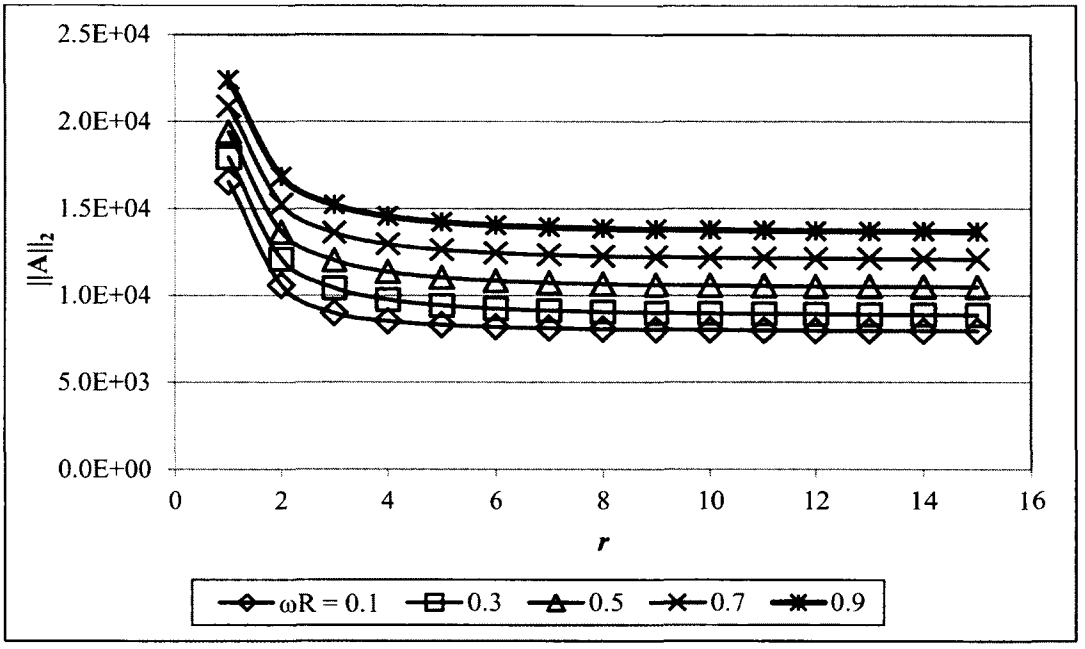

Figure 6.15 the second measure of matrix [A] variation with frequency

Figure 6.15 shows the variation of the stability measure with the frequency of the imposed perturbations. Increasing the frequency resulted in higher matrix measures for the flow. The higher frequencies therefore cause more instability in the flow.

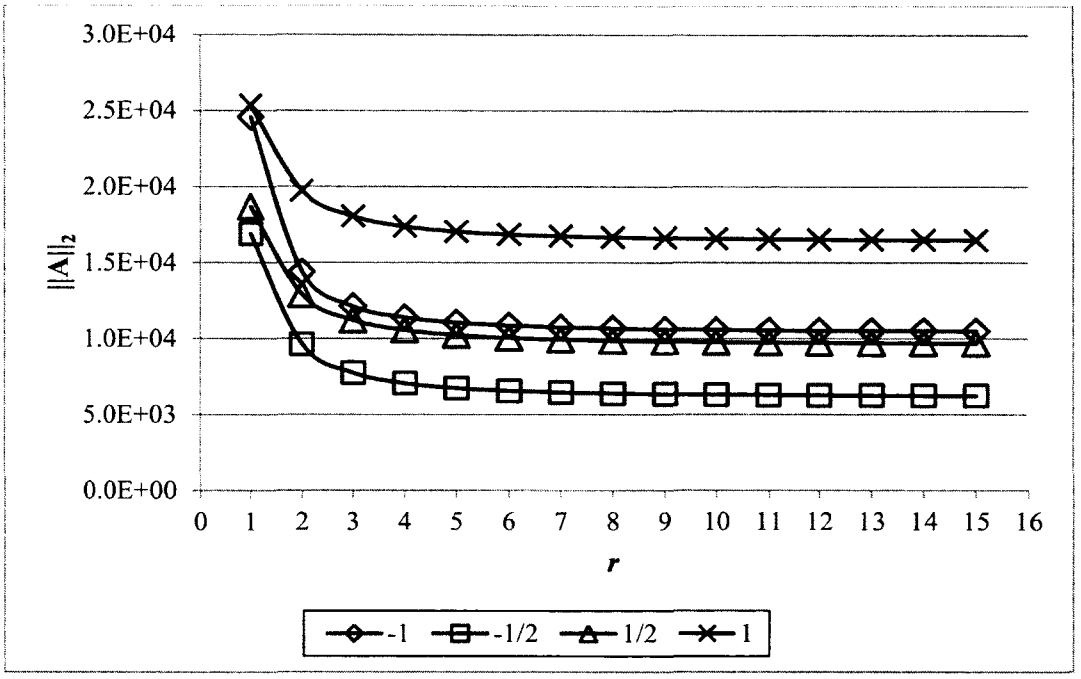

Figure 6.16 the second measure of matrix [A] at different mode numbers

Figure 6.16 shows the stability measure for the different mode numbers. The helical modes (± 1), had higher stability measures than the half modes $\pm$ ½. The physical reason for this can also be seen in the results Table 5.1, where the maximum growth of perturbations is always associated with the helical modes.

In Figure 6.17, a single stability measure is generated by integrating the second measure of coefficient matrix [A] along the radial coordinates and takes the limit at $r = \infty$. The second measure as function of radius is estimated at a fine step of 0.01, and then the integration $\int_{r_o}^{r} \lceil \mathbf{A}(r) \rceil \cdot dr$ is evaluated using a simple trapezoidal integration method. The levels of the state variable model parameters are: *Re* (8000, 10000, and 12,000); *Np* (1, 2.5, 5, and 10) x10^{-4}; ω_R (0.1, 0.3, 0.5, and 0.7).

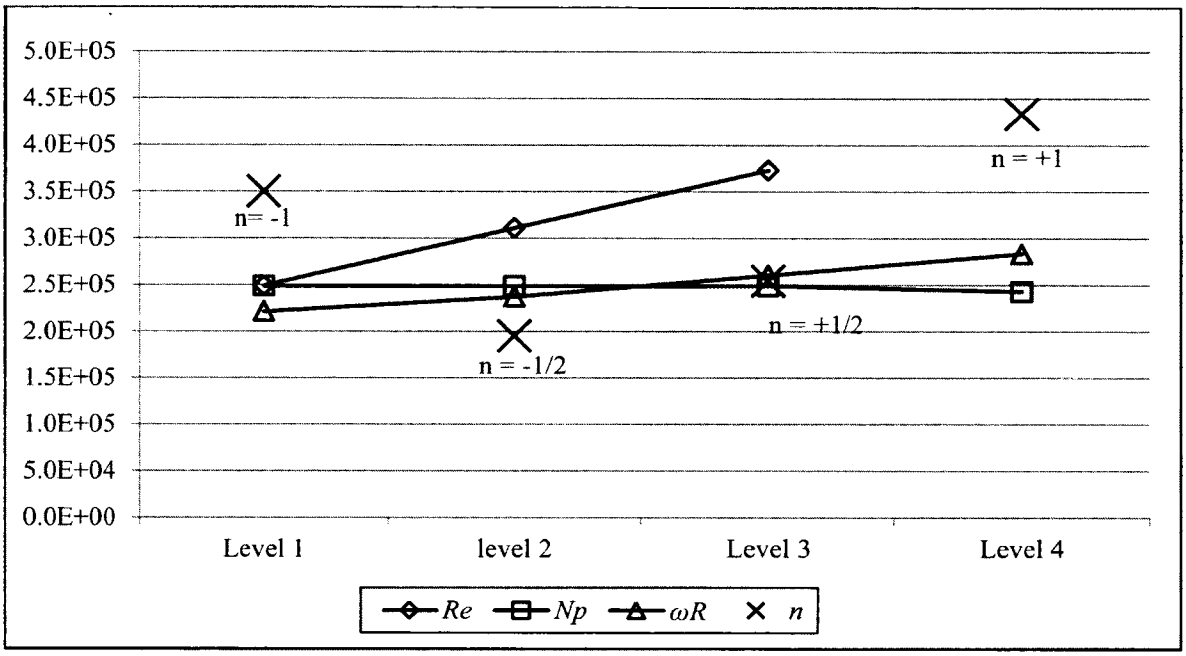

Figure 6.17 Variation of the Integration $\int_{r_o}^{r} \lceil \mathbf{A}(r) \rceil \cdot dr$ with different flow parameters

Integration of the Lyapunov function $\int_{r_o}^{r} \lceil \mathbf{A}(r) \rceil \cdot dr$ was always bounded. Positive definite values for both the matrix measure and the integration resulted, with a negative derivative of the second measure, supporting the conclusion that the flow is stable. The value of both stability parameters varied significantly with the Reynolds number and the mode number, with only slight changes associated with perturbation frequency, and no change in the stability of the system when varying the swirl parameter up to $Np = 1\text{x}10^{-3}$. Also, there was no solid proof of an existing asymptotically stable region since the integration was always bounded.

6.5 Summary

The stability analysis produced the following trends:

- Since non-equilibrium pressure and viscous forces are in balance inside the region of significant relaxation effects (within five core radii from the centerline), any instabilities observed beyond five core radii are coming from the numerical scheme due to the very small determinant of coefficient matrix [A]. This region of effective non-equilibrium forces was determined by plotting the radial variation of the effective pressure gradient term in the steady azimuthal conservation of momentum equation (3·5), showing that pressure relaxation effects were insignificant beyond five core radii and the flow could be assumed to be a potential flow only.
- The radial pressure amplitudes have unstable eigenmodes with significant positive real-parts in the region $r_c < 5$. The relaxation and viscous stresses are in balance in this region. The presence of perturbations in the flow causes the pressure profiles to increase locally in order to stabilize the flow via non-equilibrium pressure gradient forces.
- Increasing *Np* increases the width of the non-equilibrium pressure stability envelope, ranging between one and five core radii from the centerline,
- Radial perturbation velocity amplitudes were universally stable; all eigenvalues had negative real parts, and their imaginary parts (frequency) ranged between 50 and 250.
- The azimuthal perturbation velocity and radial perturbation pressure gradient amplitudes exhibited opposing instability behavior, i.e. if the azimuthal velocity amplitude was stable then the pressure gradient amplitude was not and vice versa, this is true inside the non-equilibrium pressure envelope,

- The eigenvalues migrated toward the complex axis as the radial distance increased, corresponding with increased phase angles and hence the system was more likely to become unstable,
- The unstable eigenmodes migrated toward the complex axis as the radial distance increased, hence their positive real parts were decreased,
- Helical perturbation waves $n = \pm 1$ were the most unstable azimuthal velocity perturbation modes; the coefficient matrix measures are also the highest.
- The symmetric mode $n = 0$ is stable for all values of the control parameters, deriving from the continuity constraint of zero perturbations for that mode,
- The stability analysis suggests future work to investigate the interaction between the non-equilibrium pressure and turbulent stresses of the flow inside the non-equilibrium pressure envelope $r_c \leq 5$ at higher Re.
- Lyapunov stability analysis showed that the state variable is stable for the range of Re selected between 8,000 and 12,000, since the integration of the matrix measure was always bounded and the derivative of the Lyapunov function was negative. The influence of Re and frequency of the perturbation is noticeable while *Np* doesn't affect the stability of the system. The helical modes have stability measures that were higher than the one half modes, suggesting that the unsteady structures of the helical modes are different from the half modes.

CHAPTER 7

CONCLUSIONS AND RECOMMENDATIONS

7.1 Conclusion

This study has utilized state-variable modeling methods in the scientific study of fluid dynamics, by utilizing small-amplitude velocity and pressure fluctuations and their respective derivatives as independent states in an unsteady two-dimensional vortical flow. The state-space representation not only made easier the numerical solution of the Navier-Stokes equations, but demonstrated the stability and consistency of the output fields for velocity and pressure when non-equilibrium pressure gradient forces were considered. Multiple inputs were enabled in the formulation and also a variety of outputs were allowed including: turbulence intensity, maximum amplitudes of velocity and pressure perturbations and critical radii marking the location of maximum growth of perturbations.

The axial vortex model of Ash, Zardadkhan and Zuckerwar (2011) was perturbed and the state variable simulations illuminated the following zones: (1) a laminar flow region encompassing the rotational axis, (2) an unsteady, fluctuating region near the radius of maximum steady-state azimuthal velocity that is considered here to be a non-equilibrium pressure inner region and (3) an outer, potential-vortex-like region.

The state-variable model utilized two dimensionless parameters to characterize the baseline reference flow fields; one of the parameters is a new non-equilibrium swirl parameter, Np, which related the non-equilibrium relaxation time to the axial vortex rotational time and hence the time allowed for the non-equilibrium pressure to contribute

to the evolution of the perturbations in the flow. The other parameter was the Reynolds number, Re, based on the maximum swirl velocity and core radius.

The interaction between the non-equilibrium pressure and the initiation of instabilities in the flow was investigated in this study. The non-equilibrium pressure forces, while acting on the fluid particles, affect the perturbation growth in the vortex non-equilibrium pressure zone. The relaxation process associated with non-equilibrium pressure returned the fluid particles to their equilibrium states; this process also affected the perturbations. It was found that the non-equilibrium pressure gradient forces could either suppress or enhance the fluctuations, depending on the value of the non-equilibrium swirl parameter, *Np*, acting as the controlling factor for this new phenomenon.

The maximum amplitudes of the radial pressure gradient were very large at the smallest values of the non-equilibrium swirl parameter, but that maximum amplitude "bulge" vanished by the time *Np* was equal to 0.3. As *Np* increased, the amplitude of the azimuthal velocity decreased but the critical radius moved farther inside the non-equilibrium pressure zone towards the core of the vortex. It was noted that inclusion of the relaxation stresses didn't influence the maximum growth of the radial perturbation velocity component but moved the (critical radius) location slightly closer to the core. As *Np* increased from 0.001 to 0.3, discernible perturbation Reynolds stresses became concentrated in a narrowing band located closer to the vortex core. There were general trends of decreasing amplitudes as the swirl parameter was increased to higher levels, elevating the importance of relative humidity in considering the unsteady behavior of axial

vortices since higher relative humidity corresponds with smaller values of the non-equilibrium swirl parameter and relatively dry air results in increased values.

Increasing the characteristic vortex Reynolds number increased the perturbation growth. At lower Reynolds numbers, the perturbations were found to be damped and the flow was thus more stable. The perturbation amplitudes were suppressed by inertial forces in the vicinity of the rotational axis, and the perturbation amplitude profiles have maxima within the non-equilibrium pressure region.

At Re = 8,000, the maximum azimuthal velocity amplitude was larger than any other Re, occupying the entire non-equilibrium pressure region, and at higher Reynolds numbers (Re of 10,000, 12,000, and 14,000) it exhibited smaller amplitude peaks that only occupied a narrow region. For the radial pressure gradient, the amplitude profile for different Reynolds numbers were "universal" in the inner rotational region and outer non-equilibrium portion of the flow, and it exhibited a bulge in the non-equilibrium pressure zone due to the mechanical pressure, and was likely needed to balance the propagation of sound in that region. The effect of Reynolds numbers above 8,000 on the radial perturbed velocity component was insignificant.

The critical radius of all perturbations in the flow, as the Re increased, remained inside the non-equilibrium pressure zone and became very close to the core radius at 14,000, for the enhancement of instability with existing relaxation stresses

The imposed perturbation frequencies ranged between 0.01 and 1, and the specific values were found to affect the evolution of the velocity and pressure profiles. The azimuthal velocity and pressure gradient perturbations were found to increase steadily as the frequency increased, up to a frequency of 0.4; thereafter, no change was noticed in

their amplitude growth. Concurrently, the radial velocity perturbations were unchanged as frequency increased up to 0.4, and then decreased linearly as the frequency was increased to 1. Higher damping factors for frequencies above 0.4 were found to be the reason for suppression of velocity and pressure perturbations in the range from 0.4 to 1, thus confirming with Schlichting (1968) theory of instability. Perturbation frequencies between 0.01 and 0.4 had the strongest influence on the azimuthal perturbation velocity component and the $\rho\langle v_r' v_\theta' \rangle$ Reynolds stresses. Increasing perturbation frequencies shifted the critical radii of perturbations outward from the core region.

The variation of the velocity and pressure perturbations was investigated with respect to the pitch prescribed by the non-zero azimuthal modes. Three types of profiles were identified: (1) a simple profile with a maximum located in the non-equilibrium pressure zone, which was the most common perturbation profile, (2) a double-peaked profile observed for the radial perturbation velocity amplitude and the Reynolds stress component with a mode number of -1/2, and (3) a growing trend for the radial pressure gradient perturbations at ± 1 mode numbers. The -1/2 mode showed the maximum growth for most of the perturbations except the radial velocity amplitude. At the mode number of -1/2, the critical radii of perturbations were closer to the core region than for the other modes. The radial gradient of the perturbation pressure was growing beyond the limit of 15 core radii due to the numerical scheme sensitivity.

The stability of the state variable model was discussed using two stability approaches: the eigenmodes and Lyapunov integration of a second matrix measure. The first approach of eigenmodes revealed unstable modes for the pressure function inside the non-equilibrium pressure zone ($1 \le r_c \le 5$). The non-equilibrium swirl parameter

determined the width of the non-equilibrium pressure zone. The azimuthal velocity is kept stable through interaction of non-equilibrium forces with perturbation stresses while the radial velocity had globally stable modes. The expected frequencies of perturbation evolution in the vortex flow varied significantly with *Re* and ω_R. Investigation of the effect of azimuthal orientation of perturbations in the flow showed the symmetrical waves to be universally stable, the $\pm$ ½ modes exhibited non-equilibrium pressure-perturbation stress interactions inside the effective zone, and the helical ± 1 modes yielded different perturbation structures that deserve future investigation.

Lyapunov stability functions of the vortex flow have bounded integrations between the near-centerline and approximate infinite radius, along with negative derivatives of the function, demonstrating that the state variable model and hence the flow was stable. The level of stability proved significant difference with Re and ω_R, but there was almost no change with *Np*. For the azimuthal orientation of the perturbations in the flow, the helical modes produced higher stability measures than the half-modes.

7.2 Recommendations

The successful implementation of state variable models for slightly perturbed two dimensional vortex flows suggests future work to consider the perturbation evolution to a fully developed turbulent flow. A bifurcation cycle can be described in which different flow structures can be identified. In this study, short waves were recognized at the one half azimuthal modes which interacted with non-equilibrium pressure and caused bulges in the pressure gradient profile. Also, larger-scale helical waves caused higher stability measures of the flow, along with exponentially growing profiles outside the non-equilibrium pressure

zone. Future hotwire anemometer experiments can help identify different aspects of the state variable outputs through precise measurement of the velocity perturbations (amplitudes and frequencies). The state variable parameters can also be adjusted using data from hotwires, the 2/Re relation for Np can be experimentally verified. This relation could also be a method of calculating the pressure relaxation coefficient experimentally,

The profiles showing the radial pressure gradient growing monotonically outside the non-equilibrium pressure zone indicate a possible source of sound generation that needs to either be corrected or validated. It is recommended from this point that sound propagation be studied and a model can be developed to predict this side effect of the vortical flows using separate state variable models for the inner and outer flow regions.

It is suggested to extend the useful new state variable for other Markovian property flows. The selected flows should have regions of high pressure gradient so that non-equilibrium pressure forces are significant. The non-equilibrium phenomenon has been studied for rotating flows and wakes behind spheres and cylinders (Ash and Zuckerwar, 2009, 2011).

Finally, the non-linear scheme outlined in this study is a new field of research, a step forward is recommended to numerically implement the developed model.

REFERENCES

Ash R. L. and Khorrami M. R. (1995). Vortex stability. edited by S.I. Green, In *Fluid Vortices*, 317-372. Dordrecht: Kluwer Academic publishers.

Ash, R. L. and Zuckerwar A. J. (2006). Variational approach to the volume viscosity of fluids. *Physics of Fluids* 18, 047101.

Ash, R. L. and Zuckerwar A. J. (2009). Volume viscosity in fluids with multiple dissipative processes. *Physics of Fluids* 21, 033105.

Ash, R. L., Zardadkhan I. R., and Zuckerwar A. J. (2011). The influence of pressure relaxation on the structure of an axial vortex. *Physics of Fluids* 23, 073101.

Bandyopadhyay P. R., Stead D. J. and Ash R. L. (1991). Organized Nature of a Turbulent Trailing Vortex, *AIAA Journal*, 29(10), 1627-1633.

Blais, J.A.R. 1988 *Estimation and Spectral Analysis*. Calgary: The University of Calgary Press.

Bourlès, Henri, and Kwan, G. K. (2013). System Theory (II). *In Linear Systems*. Boston: Wiley.

Brunton S. L., Rowley C. W. (2013). Empirical state-space representations for Theodorsen's lift model. *Journal of Fluids and Structures* 38, 174-186.

Bryson, A. E. Jr and Ho, Y. C. (1975). *Applied optimal control. optimization, estimation, and control*. New York: John Wiley and Sons.

Burgers, J.M. (1948). A Mathematical model illustrating the theory of turbulence. *Advance Applied Mechanics* 1, 197-1199.

Burnham, D. C, and J.N. Hallock (2013). Decay Characteristics of Wake Vortices from Jet Transport Aircraft. *Journal of Aircraft* 50(1), 82-87.

Butterworth Filter Design (2014) http://www.mathworks.com/help/signal/ref/butter.html, Documentation center.

Devenport, W.J., Zoldos, J.S., and Vogel, C.M. (1997). The structure and development of a counter-rotating wing-tip vortex pair. *Journal of Fluid Mechanics,* 332, 71-104.

Drazin, P.G. and Reid, W.H. (2004). *Hydrodynamic stability*. New York: Cambridge University Press.

Taha, H. E., Hajj, M. R., and Beran P. S. (2014) State-space representation of the unsteady aerodynamics of flapping flight. *Aerospace Science and Technology*.

Hussain F., Pradeep D. S. and Stout E. (2011). Nonlinear transient growth in a vortex column. *Journal of Fluid Mechanics,* 682, 304-331.

Jaarsveld, J. P. J., Holten A. P. C., Elsenaar, A., Trieling, R. R., and Heijst, G. J. F. (2011). An experimental study of the effect of external turbulence on the decay of a single vortex and a vortex pair, *Journal of Fluid Mechanics,* 670, 214-239.

Lacaze L., Ryan K., and Le Dizes S. (2007). Elliptic instability in a strained Batchelor vortex. *Journal of Fluid Mechanics,* 577, 341–361.

Liang Y. C., Lee H. P., Lim S. P. and Wu C. G. (2002). Proper Orthogonal Decomposition and Its Applications—Part I: Theory. *Journal of Sound and Vibration* 252(3), 527-544.

Lighthill, M.J. (1952). On sound generated aerodynamically. I. General Theory. *Proceedings of the Royal Society of London, Series A, Math. . Phys. Sci.* 211 (1107), 564-587.

Lighthill, M.J. (1954). On sound generated aerodynamically. II. Turbulence as a source of sound. *Proceedings of the Royal Society of London, Series A, Math. Phys. Sci.* 222 (1148), 1-32.

Marshall, J.S. and Beninati, M.L. (2005). An experimental study of the effect of free-stream turbulence on a trailing vortex, *Exp. In Fluids,* 38, 244-257.

Marshall, J.S. and Beninati, M.L. (2000). Turbulence evolution in vortex-dominated flows, *In Advances in Fluid Mechanics, (Nonlinear Instability, Chaos and Turbulence II, edited by L. Debnath and D.N. Riahi)* 25, 1-40, Southampton, England: WIT Press.

Meyer M. and Matthies H. G. (2004). State-space representation of instationary two-dimensional airfoil aerodynamics. *Journal of Wind Engineering and Industrial Aerodynamics*, 92 , 263–274.

Palm, W. J. III (2010). *System Dynamics (2nd ed.).* New York: Mc Grow Hill, 225.

Pradeep, D. S. and Hussain, F. (2004). Effects of boundary condition in numerical simulations of vortex dynamics. *Journal of Fluid Mechanics,* 516, 115-124.

Pradeep, D. S. and Hussain, F. (2006). Transient growth of perturbations in a vortex column. *Journal of Fluid Mechanics,* 550, 251–288.

Pradeep, D. S. and Hussain, F. (2010). Vortex dynamics of turbulence–coherent structure interaction. *Theoretical Computational Fluid Dynamics,* 24, 265-282.

Rankine, W. J. M. (1882) *A Manual of Applied Physics 10th ed.* 663. London: Charles Griff and Co.

Rennich S. C. and Lele S. K. (1997). Numerical Method for Incompressible Vortical Flows with Two Unbounded Directions. *Journal of computational physics,* 137, 101-129.

Rott, N. (1958). On the viscous core of a line vortex. Z. *Angew. Math. Phys.* 9, 543-553.

Rowell, D. (2002). *State-space representation of LTI systems.* http://web. mit. edu/2.14/www/Handouts/StateSpace. pdf

Roy, C., Leweke, T., Thompson, M.C., and Hourigan, K. (2011). Experiments on the elliptic instability in vortex pairs with axial core flow, *Journal of Fluid Mechanics,* 677, 383-416.

Saffman, S. P. and Govindaraju P. G. (1971). Flow in a turbulent trailing Vortex. *Physics of Fluids,* 14, 2074-2080.

Schlichting H., Gersten K. (2003). *Boundary-layer theory 8th ed.* New York: Springer-Verlag LLC.

Serrin, J. (1959). Mathematical principles of classical fluid mechanics. *Handbook Der Phys. VIII (1)*, 144 - 150.

Shan H., Zhang Z., and Nieuwstadt F.T.M. (1998). Direct numerical simulation of transition in pipe flow under the influence of wall disturbances. *International Journal of Heat and Fluid Flow* 19, 320-325.

Smith, E. H. (1998). *Mechanical Engineer's Reference Book* 12th ed. Oxford: Elsevier.

Stokes, G.G. (1845). On the theories of the internal friction of fluids in motion and of the equilibrium and motion of elastic solids. *Transactions of Cambridge Philosophical Society,* 8, 287-319.

Trefethen, L. N., Trefethen, A. E., Reddy S. C. and Driscoll, Tobin A. (1993). Hydrodynamic Stability without Eigenvalues. *Science* 261, 578-584.

Vatistas, G. H., Kozel, V. and Mih, W. C. (1991). A simpler model for concentrated vortices. *Experimental Fluids* 11(1), 73-76.

Vidyasagar, M., (2002). Nonlinear Systems Analysis 2^{nd} *ed.* Philadelphia: SIAM.

Witham, R. L. and Seliger, G. B. (1968). Variational principles in continuum mechanics. *Proceedings of the Royal society London, series* A.305, 1-25.

Wood, V. T. and White, L. W. (2011). A New Parametric Model of Vortex Tangential-Wind Profiles: Development, Testing, and Verification. *Journal of the Atmospheric Sciences,* 68 (5), 990-1006.

Zardadkhan, I., "The influence of non-equilibrium pressure on rotating flows," PhD Dissertation, Mechanical and Aerospace Engineering Department, Old Dominion University, August (2012).

APPENDIX A

GOVERNING EQUATIONS DERIVATION IN CYLINDRICAL COORDINATES

The Navier-Stokes equations with pressure relaxation are written in cylindrical coordinates (r,θ,z). The coordinate system is defined in Table 1.1 below.

Cartesian to Cylindrical	Cylindrical to Cartesian
$\xi_1 = r = \sqrt{x^2 + y^2}$	$x = r\ \cos\theta$
$\xi_2 = \theta = \tan^{-1}\left(\frac{y}{x}\right)$	$y = r\ \sin\theta$
$\xi_3 = z$	$z = z$

Table 1.1 The cylindrical coordinate definition

A.1 The covariant and contra-variant tangent vectors

In curvilinear coordinates, we can define tangent components associated with the Cartesian unit vectors as the covariant tangent vectors, given by:

$$g_i = \frac{\partial x_j}{\partial \xi_i} e_j, \tag{A·1}$$

and the vector components normal to it as the contravariant tangent vectors,

$$g^i = \frac{\partial \xi_i}{\partial x_j} e_j \tag{A·2}$$

It is worth noting that both the covariant and contravariant tangent vectors are associated with the curvilinear coordinates but they related to the Cartesian unit vectors which always possess the same direction.

For cylindrical coordinates:

$$\overrightarrow{g_1} = \frac{\partial x_j}{\partial \xi_1} e_j = cos\,\theta\ \overrightarrow{e_1} + sin\,\theta\ \overrightarrow{e_2}\ ;\ |\overrightarrow{g_1}| = 1 \qquad \overrightarrow{g^1} = \frac{\partial \xi_1}{\partial x_j} e_j$$

$$= cos\,\theta\ \overrightarrow{e_1} + sin\,\theta\ \overrightarrow{e_2}\ ;\ |\overrightarrow{g^1}| = 1$$

$$\overrightarrow{g_2} = \frac{\partial x_j}{\partial \xi_2} e_j = -r\,sin\,\theta\ \overrightarrow{e_1} + r\,cos\,\theta\ \overrightarrow{e_2}\ ;\ |\overrightarrow{g_2}| = r \qquad \overrightarrow{g^2} = \frac{\partial \xi_2}{\partial x_j} e_j$$

$$= -\frac{sin\,\theta}{r}\overrightarrow{e_1} + \frac{cos\,\theta}{r}\overrightarrow{e_2}\ ;\ |\overrightarrow{g^2}|$$

$$= \frac{1}{r}$$

$$\overrightarrow{g_3} = \frac{\partial x_j}{\partial \xi_3} e_j = \overrightarrow{e_3}\ ;\ |\overrightarrow{g_3}| = 1 \qquad \overrightarrow{g^3} = \frac{\partial \xi_3}{\partial x_j} e_j = \overrightarrow{e_3}\ ;\ |\overrightarrow{g^3}| = 1$$

(A·3)

Using the covariant and contravariant equations above we can write the displacement for both the curvilinear and Cartesian coordinates with respect to each other as :

$$\boldsymbol{d\xi_i} = \boldsymbol{g^i}\, dx_i \tag{A·4}$$

$$\boldsymbol{dx} = \boldsymbol{g_i}\, d\xi_i \tag{A·5}$$

The unit vectors of the covariant tangent vectors are also unit vectors for the curvilinear coordinates. For the cylindrical coordinates these unit vectors are:

$$\vec{e}_r = \frac{\overrightarrow{g_1}}{|\overrightarrow{g_1}|} = \cos\theta\ \overrightarrow{e_1} + \sin\theta\ \overrightarrow{e_2}$$

$$\vec{e}_\theta = \frac{\overrightarrow{g_2}}{|\overrightarrow{g_2}|} == -\frac{\sin\theta}{r}\overrightarrow{e_1} + \frac{\cos\theta}{r}\overrightarrow{e_2} \tag{A·6}$$

$$\vec{e}_x = \frac{\overrightarrow{g_3}}{|\overrightarrow{g_3}|} = \overrightarrow{e_3}$$

A.2 The velocity vector

Using the displacement equations A·4 and A·5 above, we can similarly write the velocity vector in terms of the covariant and contravariant components as:

$$\mathbf{v} = v_i \mathbf{g}^i = v^i \mathbf{g}_i = u_i e_i = v_r \vec{e}_r + v_\theta \vec{e}_\theta + v_z \vec{e}_z \tag{A·7}$$

The covariant and contravariant velocity expressions:

$$\mathbf{v} = v_r(\cos\theta\ \vec{e_1} + \sin\theta\,\vec{e_2}) + v_\theta\left(-\frac{\sin\theta}{r}\ \vec{e_1} + \frac{\cos\theta}{r}\ \vec{e_2}\right) + v_z\vec{e_3}$$

$$= v^1(\cos\theta\ \vec{e_1} + \sin\theta\ \vec{e_2}) + v^2(-r\sin\theta\ \vec{e_1} + r\cos\theta\ \vec{e_2}) + v^3\vec{e_3} \qquad \text{(A·8)}$$

The covariant and contravariant velocity components are given by:

$$v_i = \mathbf{v}\,.\,\mathbf{g}_i \qquad \text{(A·9)}$$
$$v^j = \mathbf{v}\,.\,\mathbf{g}^j$$

The covariant and contravariant velocity components in cylindrical coordinates are therefore,

$$v_1 = \mathbf{v}\,.\,\mathbf{g}_1 = \left[v_r(\cos\theta\ \vec{e_1} + \sin\theta\,\vec{e_2}) + v_\theta\left(-\frac{\sin\theta}{r}\ \vec{e_1} + \frac{\cos\theta}{r}\ \vec{e_2}\right) + v_z\vec{e_3}\right].(\cos\theta\ \vec{e_1} + \sin\theta\ \vec{e_2})$$

$$= v_r$$

$$v^1 = \mathbf{v}\,.\,\mathbf{g}^1 = \left[v_r(\cos\theta\ \vec{e_1} + \sin\theta\,\vec{e_2}) + v_\theta\left(-\frac{\sin\theta}{r}\ \vec{e_1} + \frac{\cos\theta}{r}\ \vec{e_2}\right) + v_z\vec{e_3}\right].(\cos\theta\ \vec{e_1} + \sin\theta\ \vec{e_2})$$

$$= v_r$$

$$v_2 = \left[v_r(\cos\theta\ \vec{e_1} + \sin\theta\,\vec{e_2}) + v_\theta\left(-\frac{\sin\theta}{r}\ \vec{e_1} + \frac{\cos\theta}{r}\ \vec{e_2}\right) + v_z\vec{e_3}\right].(-r\sin\theta\ \vec{e_1} + r\cos\theta\ \vec{e_2})$$

$$= r\,v_\theta$$

The resulting velocity components in cylindrical coordinates are summarized in Table 1.2 below.

Direction	Covariant velocity components	Contravariant velocity components
r	v_r	v_r
θ	$r\,v_\theta$	$v_\theta/_r$
z	v_z	v_z

Table 1·2 Velocity covariant and Contravariant components

A.3 The covariant and contravariant metric tensors

The dot products of the covariant or contravariant tangent vectors form the corresponding metric tensor.

$$g_{ij} = \mathbf{g}_i \cdot \mathbf{g}_j \ , g^{ij} = \mathbf{g}^i \cdot \mathbf{g}^j \tag{A·10}$$

For cylindrical coordinates if we estimate the metric tensors,

$$g_{ij} = \begin{bmatrix} 1 & 0 & 0 \\ 0 & r^2 & 0 \\ 0 & 0 & 1 \end{bmatrix}$$

$$g^{ij} = \begin{bmatrix} 1 & 0 & 0 \\ 0 & \frac{1}{r^2} & 0 \\ 0 & 0 & 1 \end{bmatrix}$$

Each one of the metric tensors is the inverse of the other.

A.4 The gradients of the covariant and contravariant tangent vectors –the Christopher symbols

The gradient of the covariant or the contravariant vectors in the curvilinear domains involves mixing derivatives with respect to curvilinear and Cartesian coordinates which is not desirable; instead the so-called Christoffel symbols are utilized to avoid this inconsistency. Using the Christoffel symbol, the gradient of the covariant tangent vector is:

$$\frac{\partial \mathbf{g}_i}{\partial \xi_j} = \frac{\partial}{\partial \xi_j}\left(\frac{\partial x_m}{\partial \xi_i}\,\overrightarrow{e_m}\right) = \frac{\partial^2 x_m}{\partial \xi_j \partial \xi_i}\left(\frac{\partial \xi_n}{\partial x_m}\,\mathbf{g}_n\right) = \frac{\partial^2 x_m}{\partial \xi_j \partial \xi_i}\frac{\partial \xi_n}{\partial x_m}\mathbf{g}_n = \Gamma_{ij}^n\,\mathbf{g}_n \tag{A·11}$$

Where the Christoffel symbol of the second kind is then defined by:

$$\Gamma_{ij}^n = \frac{\partial^2 x_m}{\partial \xi_i \partial \xi_j}\frac{\partial \xi_n}{\partial x_m} \tag{A·12}$$

Proceeding to the determination of the derivative of the contravariant tangent vector, utilizing these Christoffel symbols :

$$\frac{\partial}{\partial \xi_i}(\mathbf{g}^j \cdot \mathbf{g}_k) = \mathbf{g}_k \cdot \frac{\partial \mathbf{g}^j}{\partial \xi_i} + \mathbf{g}^j \cdot \frac{\partial \mathbf{g}_k}{\partial \xi_i} = 0 = \frac{\partial \delta_{jk}}{\partial \xi_i}$$

Then

$$\mathbf{g}_k \cdot \frac{\partial \mathbf{g}^j}{\partial \xi_i} = -\mathbf{g}^j \cdot \frac{\partial \mathbf{g}_k}{\partial \xi_i} = -\mathbf{g}^j \cdot \Gamma^n_{ki}\, \mathbf{g}_n = -\delta_{jn}\Gamma^n_{ki} = -\Gamma^j_{ki}$$

Then the contravariant tangent vector gradient is

$$\frac{\partial \mathbf{g}^j}{\partial \xi_i} = -\Gamma^j_{ki} \cdot \mathbf{g}^k \tag{A·13}$$

Alternatively we can define the covariant tangent gradient as:

$$\frac{\partial \mathbf{g}_i}{\partial \xi_j} = \frac{\partial}{\partial \xi_j}\left(\frac{\partial x_m}{\partial \xi_i} \cdot \overrightarrow{e_m}\right) = \frac{\partial^2 x_m}{\partial \xi_j \partial \xi_i} \cdot \frac{\partial x_m}{\partial \xi_k}\, \mathbf{g}^k = \Gamma_{ijk}\mathbf{g}^k \tag{A·14}$$

Here we have used the contravariant tangent vector to write the Cartesian unit vector, and the Christoffel symbol of the first kind is defined:

$$\Gamma_{ijk} = \frac{\partial^2 x_m}{\partial \xi_i \partial \xi_j}\frac{\partial x_m}{\partial \xi_k} \tag{A·15}$$

Christoffel symbols of the first and second kind are related as follows:

$$\Gamma^k_{ij} = \Gamma_{ijm}\, g^{mk} \tag{A·16}$$

In order to develop the expressions needed in the cylindrical coordinate representation of the modified Navier-Stokes equations, it is necessary to exploit the following properties of the Christoffel symbols, extracted from the derivatives of the covariant metric tensors with respect to generalized curvilinear coordinates:

$$\frac{\partial g_{ik}}{\partial \xi_j} = \frac{\partial}{\partial \xi_j}(\mathbf{g}_i \cdot \mathbf{g}_k) = \mathbf{g}_k \cdot \frac{\partial \mathbf{g}_i}{\partial \xi_j} + \mathbf{g}_i \cdot \frac{\partial \mathbf{g}_k}{\partial \xi_j} = \mathbf{g}_k \cdot \Gamma_{ijm}\mathbf{g}^m + \mathbf{g}_i \cdot \Gamma_{kjn}\mathbf{g}^n$$

$$= \delta_{km}\,\Gamma_{ijm} + \delta_{in}\,\Gamma_{kjn} = \Gamma_{ijk} + \Gamma_{kji}$$

Similarly

$$\frac{\partial g_{ik}}{\partial \xi_j} + \frac{\partial g_{jk}}{\partial \xi_i} - \frac{\partial g_{ij}}{\partial \xi_k} = \Gamma_{ijk} + \Gamma_{kji} + \Gamma_{jik} + \Gamma_{kij} - \Gamma_{ikj} - \Gamma_{jki}$$

$$= 2\Gamma_{ijk}$$

Or

$$\Gamma_{ijk} = \frac{1}{2}\left(\frac{\partial g_{ik}}{\partial \xi_j} + \frac{\partial g_{jk}}{\partial \xi_i} - \frac{\partial g_{ij}}{\partial \xi_k}\right) \tag{A·17}$$

Then using the relation between the Christoffel symbol types (Equation. A.13) we can write:

$\Gamma_{ij}^{k} = \Gamma_{ijm}\, g^{mk}$

$$\Gamma_{ij}^{k} = \frac{1}{2} g^{mk}\left(\frac{\partial g_{im}}{\partial \xi_j} + \frac{\partial g_{jm}}{\partial \xi_i} - \frac{\partial g_{ij}}{\partial \xi_m}\right) \tag{A·18}$$

In cylindrical coordinates, the only non-zero Christoffel symbols are

$\Gamma_{122} = \Gamma_{212} = r, \Gamma_{221} = -r$ and $\Gamma_{22}^{1} = -r, \Gamma_{21}^{2} = \Gamma_{12}^{2} = \frac{1}{r}$

A.5 The gradient operator

The gradient operator in curvilinear coordinates is defined as:

$$\vec{\nabla} = \mathbf{g}^{i} \frac{\partial}{\partial \xi_i}$$

A.6 Divergence of the velocity vector

Using the definition of the gradient operator, the divergence of the velocity vector can be written.

$$\vec{\nabla}.\mathbf{v} = \mathbf{g}^{i} \frac{\partial}{\partial \xi_i} . \left(v^{j}\, \mathbf{g}_j\right) = \delta_{ij} \frac{\partial v^{j}}{\partial \xi_i} + v^{j} \mathbf{g}^{i} \frac{\partial \mathbf{g}_j}{\partial \xi_i}$$

$$= \delta_{ij} \frac{\partial v^{j}}{\partial \xi_i} + v^{j} \Gamma_{ji}^{k} \delta_{ik}$$

$$\vec{\nabla}.\mathbf{v} = \frac{\partial v^{j}}{\partial \xi_j} + v^{j} \Gamma_{jk}^{k} \tag{A·19}$$

In cylindrical coordinates :

$$\vec{\nabla}.\mathbf{v} = \frac{\partial v^{j}}{\partial \xi_j} + v^{1} \Gamma_{12}^{2},$$

since this is the only non-zero Christoffel symbol.

$$\vec{\nabla}.\mathbf{v} = \frac{\partial v_r}{\partial r} + \frac{1}{r}\frac{\partial v_\theta}{\partial \theta} + \frac{\partial v_x}{\partial x} + \frac{v_r}{r} \tag{A·20}$$

A.7 The Laplacian operator

In the same manner the Laplacian operator in curvilinear coordinates can be written.

$$\nabla^2 = \left(\mathbf{g}^i \frac{\partial}{\partial \xi_i}\right).\left(\mathbf{g}^j \frac{\partial}{\partial \xi_j}\right) = \mathbf{g}^i.\mathbf{g}^j \frac{\partial^2}{\partial \xi_i \partial \xi_j} + \left(\mathbf{g}^i \frac{\partial \mathbf{g}^j}{\partial \xi_i}\right).\frac{\partial}{\partial \xi_j}$$

$$= \mathbf{g}^{ij} \frac{\partial^2}{\partial \xi_i \partial \xi_j} + \left(\mathbf{g}^i \frac{\partial \mathbf{g}^j}{\partial \xi_i}\right).\frac{\partial}{\partial \xi_j}$$

But $\mathbf{g}^{ik}\mathbf{g}_k = \mathbf{g}^i.\mathbf{g}^k\mathbf{g}_k = \mathbf{g}^i$

Then substituting back in the previous equation

$$\nabla^2 = g^{ij} \frac{\partial^2}{\partial \xi_i \partial \xi_j} + \left(g^i \frac{\partial g^{jk} g_k}{\partial \xi_i}\right).\frac{\partial}{\partial \xi_j} =$$

$$= g^{ij} \frac{\partial^2}{\partial \xi_i \partial \xi_j} + \left(g^i g^{jk} \frac{\partial g_k}{\partial \xi_i} + g^i g_k \frac{\partial g^{jk}}{\partial \xi_i}\right).\frac{\partial}{\partial \xi_j}$$

$$= g^{ij} \frac{\partial^2}{\partial \xi_i \partial \xi_j} + \left(g^i g^{jk} \frac{\partial g_k}{\partial \xi_i} + \delta_{ik} \frac{\partial g^{jk}}{\partial \xi_i}\right).\frac{\partial}{\partial \xi_j}$$

or
$$\nabla^2 = g^{ij} \frac{\partial^2}{\partial \xi_i \partial \xi_j} + \left(g^{jk}\Gamma^i_{ki} + \frac{\partial g^{ij}}{\partial \xi_i}\right).\frac{\partial}{\partial \xi_j} \tag{A·21}$$

In the cylindrical coordinates, this relationship becomes :

$$\nabla^2 = \frac{1}{r}\frac{\partial}{\partial r}\left(r\frac{\partial}{\partial r}\right) + \frac{1}{r^2}\frac{\partial^2}{\partial \theta^2} + \frac{\partial^2}{\partial x^2} \tag{A·22}$$

A.8 Conservation of mass

The conservation of mass equation in vector form is:

$$\frac{\partial \rho}{\partial t} + \nabla.(\rho v) = 0$$

In cylindrical coordinates (using equation 1.28):

$$\frac{\partial \rho}{\partial t}+\frac{\partial \rho v_r}{\partial r}+\frac{1}{r}\frac{\partial \rho v_\theta}{\partial \theta}+\frac{\partial \rho v_x}{\partial x}+\rho\frac{v_r}{r}=0 \tag{A·23}$$

A.9 Conservation of linear momentum for an incompressible fluid

The conservation of linear momentum in vector form:

$$\frac{\partial(\rho \mathbf{v})}{\partial t}+(\mathbf{v}.\vec{\nabla})\rho\mathbf{v}=-\vec{\nabla}P+\eta_P\frac{D}{Dt}\vec{\nabla}P+\mu\nabla^2\mathbf{v}$$

To write this equation in curvilinear coordinates, taking term by term; the first term on each side is obvious, then the convective term is:

$$(\mathbf{v}.\vec{\nabla})\mathbf{v}=\left(v^j\mathbf{g}_j\,.\,\mathbf{g}^k\frac{\partial}{\partial\xi_k}\right)v^i\mathbf{g}_i=\left(v^j\frac{\partial}{\partial\xi_j}\right)v^i\mathbf{g}_i=\left(v^j\frac{\partial v^n}{\partial\xi_j}+v^iv^j\Gamma^n_{ij}\right)\mathbf{g}_n \tag{A·24}$$

In cylindrical coordinates the components in three directions are

$$\begin{aligned}
&=\left(v^1\frac{\partial v^1}{\partial\xi_1}+v^2\frac{\partial v^1}{\partial\xi_2}+v^3\frac{\partial v^1}{\partial\xi_3}+v^2v^2\Gamma^1_{22}\right)g_1+\left(v^1\frac{\partial v^2}{\partial\xi_1}+v^2\frac{\partial v^2}{\partial\xi_2}+v^3\frac{\partial v^2}{\partial\xi_3}+v^1v^2\Gamma^2_{12}\right)g_2\\
&\quad+\left(v^1\frac{\partial v^3}{\partial\xi_1}+v^2\frac{\partial v^3}{\partial\xi_2}+v^3\frac{\partial v^3}{\partial\xi_3}\right)g_3\\
&=\left(v_r\frac{\partial v_r}{\partial r}+\frac{v_\theta}{r}\frac{\partial v_r}{\partial\theta}+v_x\frac{\partial v_r}{\partial x}-\frac{v_\theta^2}{r}\right)e_r+\left(v_r\frac{\partial v_\theta}{\partial r}+\frac{v_\theta}{r}\frac{\partial v_\theta}{\partial\theta}+v_x\frac{\partial v_\theta}{\partial x}+\frac{v_rv_\theta}{r}\right)e_\theta\\
&\quad+\left(v_r\frac{\partial v_x}{\partial r}+\frac{v_\theta}{r}\frac{\partial v_x}{\partial\theta}+v_x\frac{\partial v_x}{\partial x}\right)e_x
\end{aligned}$$

Next

$$\begin{aligned}
\nabla^2\mathbf{v}&=\left[g^{ij}\frac{\partial^2}{\partial\xi_i\partial\xi_j}+\left(g^{jk}\Gamma^i_{ki}+\frac{\partial g^{ij}}{\partial\xi_i}\right).\frac{\partial}{\partial\xi_j}\right]v^ng_n\\
&=g^{ij}\frac{\partial^2(v^ng_n)}{\partial\xi_i\partial\xi_j}+\left(g^{jk}\Gamma^i_{ki}+\frac{\partial g^{ij}}{\partial\xi_i}\right).\frac{\partial(v^ng_n)}{\partial\xi_j}
\end{aligned} \tag{A·25}$$

Now

$$\begin{aligned}
\frac{\partial^2(v^ng_n)}{\partial\xi_i\partial\xi_j}&=\frac{\partial}{\partial\xi_j}\left[\left(\frac{\partial v^n}{\partial\xi_i}+v^i\Gamma^n_{ij}\right)g_n\right]\\
&=g_n\left(\frac{\partial^2v^n}{\partial\xi_i\partial\xi_j}+v^i\frac{\partial\Gamma^n_{ij}}{\partial\xi_j}+\frac{\partial v^i}{\partial\xi_j}\Gamma^n_{ij}\right)+\left(\frac{\partial v^n}{\partial\xi_i}+v^i\Gamma^n_{ij}\right)\frac{\partial g_n}{\partial\xi_j}\\
&=g_n\left(\frac{\partial^2v^n}{\partial\xi_i\partial\xi_j}+v^i\frac{\partial\Gamma^n_{ij}}{\partial\xi_j}+\frac{\partial v^i}{\partial\xi_j}\Gamma^n_{ij}\right)+\left(\frac{\partial v^n}{\partial\xi_i}+v^i\Gamma^n_{ij}\right)\Gamma^m_{nj}g_m
\end{aligned}$$

$$= \left[\frac{\partial^2 v^n}{\partial\xi_i\partial\xi_j} + \Gamma^n_{ij}\frac{\partial v^i}{\partial\xi_j} + \Gamma^m_{mj}\frac{\partial v^m}{\partial\xi_i} + v^i\frac{\partial\Gamma^n_{ij}}{\partial\xi_j} + v^i\Gamma^m_{ij}\Gamma^m_{mj}\right]g_n$$

And the second term in Equation. (A·25) is:

$$\left(g^{jk}\Gamma^i_{ki} + \frac{\partial g^{ij}}{\partial\xi_i}\right).\frac{\partial\left(v^n g_n\right)}{\partial\xi_j} = \left[g^{jk}\Gamma^i_{ki} + \frac{\partial g^{ij}}{\partial\xi_i}\right]\left[\left[\left(\frac{\partial v^n}{\partial\xi_j} + v^i\Gamma^n_{ij}\right)g_n\right]\right]$$

The final expression for the Laplacian

$$\nabla^2\mathbf{v} = g^{ij}g_n\left(\frac{\partial^2 v^n}{\partial\xi_i\partial\xi_j} + \Gamma^n_{ij}\frac{\partial v^i}{\partial\xi_j} + \Gamma^m_{mj}\frac{\partial v^m}{\partial\xi_i} + v^i\frac{\partial\Gamma^n_{ij}}{\partial\xi_j} + v^i\Gamma^m_{ij}\Gamma^m_{mj}\right) + \left(g^{jk}\Gamma^i_{ki} + \frac{\partial g^{ij}}{\partial\xi_i}\right)\left(\frac{\partial v^n}{\partial\xi_j} + v^i\Gamma^n_{ij}\right)g_n \quad \text{(A·26)}$$

In cylindrical coordinates, the components of the viscous terms are

$$\left\{\frac{\partial}{\partial r}\left[\frac{1}{r}\frac{\partial}{\partial r}\left(rv_r\right)\right] + \frac{1}{r^2}\frac{\partial^2 v_r}{\partial\theta^2} - \frac{\partial^2 v_r}{\partial x^2} - \frac{2}{r^2}\frac{\partial v_\theta}{\partial\theta}\right\}\mathbf{e}_r + \left\{\frac{\partial}{\partial r}\left[\frac{1}{r}\frac{\partial}{\partial r}\left(rv_\theta\right)\right] + \frac{1}{r^2}\frac{\partial^2 v_\theta}{\partial\theta^2} - \frac{\partial^2 v_\theta}{\partial x^2} + \frac{2}{r^2}\frac{\partial v_r}{\partial\theta}\right\}\mathbf{e}_\theta +$$

$$\left\{\frac{\partial}{\partial r}\left[\frac{1}{r}\frac{\partial}{\partial r}\left(rv_x\right)\right] + \frac{1}{r^2}\frac{\partial^2 v_x}{\partial\theta^2} - \frac{\partial^2 v_x}{\partial x^2}\right\}\mathbf{e}_x$$

(A·27)

A.10 The pressure relaxation expressions

$$\frac{\mathrm{D}}{\mathrm{Dt}}\left(\vec{\nabla}\mathrm{P}\right) = \left[\frac{\partial}{\partial\mathrm{t}} + (v.\nabla)\right]\vec{\nabla}\mathrm{P} \quad \text{(A·28)}$$

Convective time derivative of the gradient of pressure:

$$\bar{\mathbf{v}}\cdot\bar{\nabla}\bar{\nabla}P = v^i\mathbf{g}_i\cdot\mathbf{g}^j\frac{\partial}{\partial\xi_j}\left(\mathbf{g}^k\frac{\partial P}{\partial\xi_k}\right) = v^j\left[\left(\frac{\partial\mathbf{g}^k}{\partial\xi_j}\right)\left(\frac{\partial P}{\partial\xi_k}\right) + \mathbf{g}^k\frac{\partial^2 P}{\partial\xi_j\partial\xi_k}\right].$$

Now:

$$\frac{\partial\mathbf{g}^k}{\partial\xi_j} = -\Gamma^k_{jn}\mathbf{g}^n \quad \text{and} \quad \mathbf{g}^n = g^{nm}\mathbf{g}_m$$

$$\vec{\mathbf{v}}\cdot\vec{\nabla}\vec{\nabla}P = v^j\left[\mathbf{g}^n\frac{\partial^2 P}{\partial\xi_j\partial\xi_n} - \Gamma^k_{jn}\mathbf{g}^n\left(\frac{\partial P}{\partial\xi_k}\right)\right] = \mathbf{g}^n\left[v^j\frac{\partial^2 P}{\partial\xi_j\partial\xi_n} - v^j\Gamma^k_{jn}\left(\frac{\partial P}{\partial\xi_k}\right)\right]. \qquad \text{(A·29)}$$

Also, $\Gamma^1_{22} = -r$, $\Gamma^2_{21} = \dfrac{1}{r} = \Gamma^2_{12}$, are the only non-zero Christoffel symbols of the second kind, in cylindrical coordinates.

Consequently,

$$\vec{\mathbf{v}}\cdot\vec{\nabla}\vec{\nabla}P = \mathbf{g}^n\left[v^j\frac{\partial^2 P}{\partial\xi_j\partial\xi_n} - v^j\Gamma^k_{jn}\left(\frac{\partial P}{\partial\xi_k}\right)\right] =$$

$$= \mathbf{g}^1\left[v^j\frac{\partial^2 P}{\partial\xi_j\partial r} - v^j\Gamma^k_{j1}\left(\frac{\partial P}{\partial\xi_k}\right)\right] - \mathbf{g}^2\left[v^j\frac{\partial^2 P}{\partial\xi_j\partial\theta} - v^j\Gamma^k_{j2}\left(\frac{\partial P}{\partial\xi_k}\right)\right] - \mathbf{g}^3\left[v^j\frac{\partial^2 P}{\partial\xi_j\partial z} - v^j\Gamma^k_{j3}\left(\frac{\partial P}{\partial\xi_k}\right)\right]$$

Now:

$$\mathbf{g}^1\left[v^j\frac{\partial^2 P}{\partial\xi_j\partial r} - v^j\Gamma^k_{j1}\left(\frac{\partial P}{\partial\xi_k}\right)\right] = \mathbf{g}^1\left[v^j\frac{\partial^2 P}{\partial\xi_j\partial r} - v^2\Gamma^2_{21}\left(\frac{\partial P}{\partial\theta}\right)\right] =$$

$$= \mathbf{e}_r\left[v^1\frac{\partial^2 P}{\partial r^2} - v^2\frac{\partial^2 P}{\partial\theta\partial r} - v^3\frac{\partial^2 P}{\partial z\partial r} - \frac{v^2}{r}\left(\frac{\partial P}{\partial\theta}\right)\right] = \mathbf{e}_r\left[v_r\frac{\partial^2 P}{\partial r^2} - \frac{v_\theta}{r}\frac{\partial^2 P}{\partial\theta\partial r} - v_z\frac{\partial^2 P}{\partial z\partial r} - \frac{v_\theta}{r^2}\left(\frac{\partial P}{\partial\theta}\right)\right]$$

$$\mathbf{g}^2\left[v^j\frac{\partial^2 P}{\partial\xi_j\partial\theta} - v^j\Gamma^k_{j2}\left(\frac{\partial P}{\partial\xi_k}\right)\right] = \mathbf{g}^2\left[v^j\frac{\partial^2 P}{\partial\xi_j\partial\theta} - v^2\Gamma^1_{22}\left(\frac{\partial P}{\partial r}\right) - v^1\Gamma^2_{12}\left(\frac{\partial P}{\partial\theta}\right)\right],$$

$$\mathbf{g}^2\left[v^j\frac{\partial^2 P}{\partial\xi_j\partial\theta} - v^2\Gamma^1_{22}\left(\frac{\partial P}{\partial r}\right) - v^1\Gamma^2_{12}\left(\frac{\partial P}{\partial\theta}\right)\right] = \frac{\mathbf{e}_\theta}{r}\left[v^1\frac{\partial^2 P}{\partial r\partial\theta} - v^2\frac{\partial^2 P}{\partial\theta^2} - v^3\frac{\partial^2 P}{\partial z\partial\theta} - rv^2\left(\frac{\partial P}{\partial r}\right) - \frac{v^1}{r}\left(\frac{\partial P}{\partial\theta}\right)\right]$$

$$= \mathbf{e}_\theta\left[\frac{v_r}{r}\frac{\partial^2 P}{\partial r\partial\theta} - \frac{v_\theta}{r^2}\frac{\partial^2 P}{\partial\theta^2} - \frac{v_z}{r}\frac{\partial^2 P}{\partial z\partial\theta} - \frac{v_\theta}{r}\left(\frac{\partial P}{\partial r}\right) - \frac{v_r}{r^2}\left(\frac{\partial P}{\partial\theta}\right)\right]$$

and

$$\mathbf{g}^3\left[v^j\frac{\partial^2 P}{\partial\xi_j\partial z}-v^j\Gamma^k_{j3}\left(\frac{\partial P}{\partial\xi_k}\right)\right]=\mathbf{e}_z\left[v^1\frac{\partial^2 P}{\partial r\partial z}-v^2\frac{\partial^2 P}{\partial\theta\partial z}-v^3\frac{\partial^2 P}{\partial z^2}\right]=\mathbf{e}_z\left[v_r\frac{\partial^2 P}{\partial r\partial z}-\frac{v_\theta}{r}\frac{\partial^2 P}{\partial\theta\partial z}-v_z\frac{\partial^2 P}{\partial z^2}\right]$$

.

Now the convective part of the pressure relaxation equation (A·26) is:

$$\mathbf{v}\cdot\vec{\nabla}\vec{\nabla}P=$$

$$(\mathbf{v}.\nabla)\vec{\nabla}P=\left[v_r\frac{\partial}{\partial r}+\frac{v_\theta}{r}\frac{\partial}{\partial\theta}+v_x\frac{\partial}{\partial x}\right]\left[\vec{e}_r\frac{\partial P}{\partial r}+\vec{e}_\theta\frac{1}{r}\frac{\partial P}{\partial\theta}+\vec{e}_x\frac{\partial P}{\partial x}\right]$$

$$=v_r\frac{\partial}{\partial r}\left[\vec{e}_r\frac{\partial P}{\partial r}+\vec{e}_\theta\frac{1}{r}\frac{\partial P}{\partial\theta}+\vec{e}_x\frac{\partial P}{\partial x}\right]+\frac{v_\theta}{r}\frac{\partial}{\partial\theta}\left[\vec{e}_r\frac{\partial P}{\partial r}+\vec{e}_\theta\frac{1}{r}\frac{\partial P}{\partial\theta}+\vec{e}_x\frac{\partial P}{\partial x}\right]+v_x\frac{\partial}{\partial x}\left[\vec{e}_r\frac{\partial P}{\partial r}+\vec{e}_\theta\frac{1}{r}\frac{\partial P}{\partial\theta}+\vec{e}_x\frac{\partial P}{\partial x}\right]$$

$$=v_r\left[\vec{e}_r\frac{\partial^2 P}{\partial r^2}+\vec{e}_\theta\left(\frac{1}{r}\frac{\partial^2 P}{\partial r\partial\theta}-\frac{1}{r^2}\frac{\partial P}{\partial\theta}\right)+\vec{e}_x\frac{\partial^2 P}{\partial r\partial x}\right]$$

$$+\frac{v_\theta}{r}\left[\vec{e}_r\frac{\partial^2 P}{\partial\theta\partial r}+\vec{e}_\theta\frac{\partial P}{\partial r}+\vec{e}_\theta\frac{1}{r}\frac{\partial^2 P}{\partial\theta^2}-\vec{e}_r\frac{1}{r}\frac{\partial P}{\partial\theta}+\vec{e}_x\frac{\partial^2 P}{\partial\theta\partial x}\right]$$

$$+v_x\left[\vec{e}_r\frac{\partial^2 P}{\partial x\partial r}+\vec{e}_\theta\left(\frac{1}{r}\frac{\partial^2 P}{\partial\theta\partial x}\right)+\vec{e}_x\frac{\partial^2 P}{\partial x^2}\right]$$

$$(\mathbf{v}.\nabla)\vec{\nabla}P=\vec{e}_r\left[v_r\frac{\partial^2 P}{\partial r^2}+\frac{v_\theta}{r}\frac{\partial^2 P}{\partial\theta\partial r}+v_x\frac{\partial^2 P}{\partial x\partial r}-\frac{v_\theta}{r^2}\frac{\partial P}{\partial\theta}\right]$$

$$+\vec{e}_\theta\left[\frac{v_r}{r}\frac{\partial^2 P}{\partial r\partial\theta}+\frac{v_\theta}{r^2}\frac{\partial^2 P}{\partial\theta^2}+\frac{v_x}{r}\frac{\partial^2 P}{\partial\theta\partial x}-\frac{v_r}{r^2}\frac{\partial P}{\partial\theta}+\frac{v_\theta}{r}\frac{\partial P}{\partial r}\right]+$$

$$\vec{e}_x\left[v_r\frac{\partial^2 P}{\partial r\partial x}+\frac{v_\theta}{r}\frac{\partial^2 P}{\partial\theta\partial x}+v_x\frac{\partial^2 P}{\partial x^2}\right] \qquad \text{(A·30)}$$

A.11 Conservation of mass and momentum for an incompressible fluid in cylindrical coordinates

Conservation of mass (continuity):

$$\frac{1}{r}\frac{\partial}{\partial r}(rv_r)+\frac{1}{r}\frac{\partial v_\theta}{\partial\theta}+\frac{\partial v_z}{\partial z}=0 \qquad \text{(A·31)}$$

Conservation of radial momentum:

$$\rho\left(\frac{\partial v_r}{\partial t}+v_r\frac{\partial v_r}{\partial r}+\frac{v_\theta}{r}\frac{\partial v_r}{\partial \theta}-\frac{v_\theta^2}{r}+v_z\frac{\partial v_r}{\partial z}\right)=\mu\left\{\frac{\partial}{\partial r}\left[\frac{1}{r}\frac{\partial}{\partial r}\left(rv_r\right)\right]+\frac{1}{r^2}\frac{\partial^2 v_r}{\partial \theta^2}+\frac{\partial^2 v_r}{\partial z^2}-\frac{2}{r^2}\frac{\partial v_\theta}{\partial \theta}\right\}+$$

$$+\eta_P\left[v_r\frac{\partial^2 P}{\partial r^2}+\frac{v_\theta}{r}\frac{\partial^2 P}{\partial \theta \partial r}+v_z\frac{\partial^2 P}{\partial z\partial r}+\frac{v_\theta}{r^2}\left(\frac{\partial P}{\partial \theta}\right)\right]+\frac{\partial P}{\partial r} \qquad \text{(A.32)}$$

Conservation of azimuthal momentum:

$$\rho\left(\frac{\partial v_\theta}{\partial t}+v_r\frac{\partial v_\theta}{\partial r}+\frac{v_\theta}{r}\frac{\partial v_\theta}{\partial \theta}+\frac{v_r v_\theta}{r}+v_z\frac{\partial v_\theta}{\partial z}\right)=\mu\left\{\frac{\partial}{\partial r}\left[\frac{1}{r}\frac{\partial}{\partial r}\left(rv_\theta\right)\right]+\frac{1}{r^2}\frac{\partial^2 v_\theta}{\partial \theta^2}+\frac{\partial^2 v_\theta}{\partial z^2}+\frac{2}{r^2}\frac{\partial v_r}{\partial \theta}\right\}+$$

$$+\eta_P\left[\frac{v_r}{r}\frac{\partial^2 P}{\partial r\partial \theta}+\frac{v_\theta}{r^2}\frac{\partial^2 P}{\partial \theta^2}+\frac{v_z}{r}\frac{\partial^2 P}{\partial z\partial \theta}+\frac{v_\theta}{r}\left(\frac{\partial P}{\partial r}\right)+\frac{v_r}{r^2}\left(\frac{\partial P}{\partial \theta}\right)\right]+\frac{1}{r}\frac{\partial P}{\partial \theta} \qquad \text{(A.33)}$$

Conservation of axial momentum:

$$\rho\left(\frac{\partial v_z}{\partial t}+v_r\frac{\partial v_z}{\partial r}+\frac{v_\theta}{r}\frac{\partial v_z}{\partial \theta}+v_z\frac{\partial v_z}{\partial z}\right)=\mu\left\{\frac{\partial}{\partial r}\left[\frac{1}{r}\frac{\partial}{\partial r}\left(rv_z\right)\right]+\frac{1}{r^2}\frac{\partial^2 v_z}{\partial \theta^2}+\frac{\partial^2 v_z}{\partial z^2}\right\}+\frac{\partial P}{\partial z}+$$

$$+\eta_P\left[v_r\frac{\partial^2 P}{\partial r\partial z}+\frac{v_\theta}{r}\frac{\partial^2 P}{\partial \theta \partial z}+v_z\frac{\partial^2 P}{\partial z^2}\right] \qquad \text{(A.34)}$$

APPENDIX B

PRESSURE POISSON'S EQUATION WITH PRESSURE RELXATION

The Poisson-like equation governing the pressure perturbations is new and has been employed for the first time in the present study. That derivation starts by taking the divergence of the conservation of momentum equation, after first recognizing from the continuity equation that

$$\nabla \cdot \left(\frac{\partial \mathbf{v}}{\partial t} \right) = \frac{\partial}{\partial t} \left[\nabla \cdot \mathbf{v} \right] = 0, \tag{B·1}$$

so that

$$\nabla \cdot \frac{D\mathbf{v}}{Dt} = \nabla \cdot \left[\mathbf{v} \cdot \nabla \mathbf{v} \right] = \left(-1 - Np \frac{\partial}{\partial t} \right) \nabla^2 P - Np \nabla \cdot \left[\mathbf{v} \cdot \nabla \left[\nabla P \right] \right]. \tag{B·2}$$

Employing the curvilinear coordinate methods described in Appendix A, equation (B.2) requires a term-by-term development:

Divergence of the convective term $\nabla \cdot \left[\mathbf{v} \cdot \nabla \mathbf{v} \right]$

From (A.24),

$$\mathbf{v} \cdot \vec{\nabla} \mathbf{v} = v^j \frac{\partial}{\partial \xi_j} v^n \mathbf{g}_n = v^j \left(v^n \frac{\partial g_n}{\partial \xi_j} + \frac{\partial v^n}{\partial \xi_j} g_n \right) = v^j \left(v^n \Gamma^k_{nj} g_k + \frac{\partial v^n}{\partial \xi_j} g_n \right) = v^j \left(v^n \Gamma^l_{nj} + \frac{\partial v^l}{\partial \xi_j} \right) g_l$$

Taking the gradient of this term,

$$\nabla\cdot\left[\mathbf{v}\cdot\nabla\mathbf{v}\right]=\mathbf{g}^s\frac{\partial}{\partial\xi_s}\cdot\left[v^j\left(v^n\Gamma^l_{nj}+\frac{\partial v^l}{\partial\xi_j}\right)\mathbf{g}_l\right]$$

$$=\mathbf{g}^s\cdot\mathbf{g}_l\frac{\partial}{\partial\xi_s}\cdot\left[v^j\left(v^n\Gamma^l_{nj}+\frac{\partial v^l}{\partial\xi_j}\right)\right]+\left[v^j\left(v^n\Gamma^l_{nj}+\frac{\partial v^l}{\partial\xi_j}\right)\mathbf{g}^s\cdot\frac{\partial\mathbf{g}_l}{\partial\xi_s}\cdot\right]$$

$$=\delta_{sl}\cdot\left[\frac{\partial v^j}{\partial\xi_s}\left(v^n\Gamma^l_{nj}+\frac{\partial v^l}{\partial\xi_j}\right)+v^j\left(\frac{\partial v^n}{\partial\xi_s}\Gamma^l_{nj}+\frac{\partial\Gamma^l_{nj}}{\partial\xi_s}v^n+\frac{\partial^2v^l}{\partial\xi_s\partial\xi_j}\right)\right]+\left[v^j\left(v^n\Gamma^l_{nj}+\frac{\partial v^l}{\partial\xi_j}\right)\Gamma^m_{ls}\mathbf{g}^s\cdot\mathbf{g}_m\right]$$

$$=\frac{\partial v^j}{\partial\xi_s}\left(v^n\Gamma^s_{nj}+\frac{\partial v^s}{\partial\xi_j}\right)+v^j\left(\frac{\partial v^n}{\partial\xi_s}\Gamma^s_{nj}+\frac{\partial\Gamma^s_{nj}}{\partial\xi_s}v^n+\frac{\partial^2v^s}{\partial\xi_s\partial\xi_j}\right)+v^j\left(v^n\Gamma^l_{nj}+\frac{\partial v^l}{\partial\xi_j}\right)\Gamma^s_{ls}$$

or,

$$\nabla\cdot\left[\mathbf{v}\cdot\nabla\mathbf{v}\right]=\underbrace{\frac{\partial v^s}{\partial\xi_l}\frac{\partial v^j}{\partial\xi_s}}_{1}+\underbrace{\Gamma^s_{nj}\left(v^n\frac{\partial v^j}{\partial\xi_s}+v^j\frac{\partial v^n}{\partial\xi_s}\right)}_{2}+\underbrace{v^j\frac{\partial^2v^s}{\partial\xi_s\partial\xi_j}}_{3}+\underbrace{v^jv^n\frac{\partial\Gamma^s_{nj}}{\partial\xi_s}}_{4}+\underbrace{v^j\Gamma^s_{ls}\frac{\partial v^l}{\partial\xi_j}}_{5}+\underbrace{v^jv^n\Gamma^l_{nj}\Gamma^s_{ls}}_{6} \tag{B·3}$$

In the two-dimensional cylindrical coordinate representation, the velocity derivatives are

$\frac{\partial v^1}{\partial\xi_1}=\frac{\partial v_r}{\partial r}$, $\frac{\partial v^1}{\partial\xi_2}=\frac{\partial v_r}{\partial\theta}$, $\frac{\partial v^2}{\partial\xi_1}=\frac{\partial}{\partial r}\left(\frac{v_\theta}{r}\right)$, and $\frac{\partial v^2}{\partial\xi_2}=\frac{1}{r}\frac{\partial v_\theta}{\partial\theta}$.

The only non-zero Christoffel symbols in cylindrical coordinates are $\Gamma^1_{22}=-r$ and $\Gamma^2_{12}=\frac{1}{r}=\Gamma^2_{21}$.

Expanding the numbered terms in equations (B.3),

term number (1) becomes,

$$\frac{\partial v^s}{\partial\xi_j}\frac{\partial v^j}{\partial\xi_s}=\left(\frac{\partial v^1}{\partial\xi_1}\right)^2+\left(\frac{\partial v^2}{\partial\xi_2}\right)^2+2\frac{\partial v^2}{\partial\xi_1}\frac{\partial v^1}{\partial\xi_2}=\left(\frac{\partial v_r}{\partial r}\right)^2+\left(\frac{1}{r}\frac{\partial v_\theta}{\partial\theta}\right)^2+2\frac{\partial}{\partial r}\left(\frac{v_\theta}{r}\right)\frac{\partial v_r}{\partial\theta},$$

term number (2),

$$\Gamma^s_{nj}\left(v^n\frac{\partial v^j}{\partial\xi_s}+v^j\frac{\partial v^n}{\partial\xi_s}\right)=\Gamma^1_{22}\left(v^2\frac{\partial v^2}{\partial\xi_1}+v^2\frac{\partial v^2}{\partial\xi_1}\right)+\Gamma^2_{12}\left(v^1\frac{\partial v^2}{\partial\xi_2}+v^2\frac{\partial v^1}{\partial\xi_2}\right)+\Gamma^2_{21}\left(v^2\frac{\partial v^1}{\partial\xi_2}+v^1\frac{\partial v^2}{\partial\xi_2}\right)$$

$$=-2v_\theta\frac{\partial}{\partial r}\left(\frac{v_\theta}{r}\right)+\frac{2}{r}\left(\frac{v_r}{r}\frac{\partial v_\theta}{\partial\theta}+\frac{v_\theta}{r}\frac{\partial v_r}{\partial\theta}\right),$$

term number (3),

$$v^j \frac{\partial^2 v^s}{\partial \xi_s \partial \xi_j} = v^1 \frac{\partial^2 v^1}{\partial \xi_1 \partial \xi_1} + v^1 \frac{\partial^2 v^2}{\partial \xi_2 \partial \xi_1} + v^2 \frac{\partial^2 v^1}{\partial \xi_1 \partial \xi_2} + v^2 \frac{\partial^2 v^2}{\partial \xi_2 \partial \xi_2}$$

$$= v_r \frac{\partial^2 v_r}{\partial r^2} + v_r \frac{\partial^2}{\partial \theta \partial r}\left(\frac{v_\theta}{r}\right) + \frac{v_\theta}{r}\frac{\partial^2 v_r}{\partial r \partial \theta} + \frac{v_\theta}{r^2}\frac{\partial^2 v_\theta}{\partial \theta^2},$$

term number (4),

$$v^j v^n \frac{\partial \Gamma^s_{nj}}{\partial \xi_s} = v^2 v^2 \frac{\partial \Gamma^1_{22}}{\partial \xi_1} = -\left(\frac{v_\theta}{r}\right)^2,$$

term number (5),

$$v^j \Gamma^s_{ls} \frac{\partial v^l}{\partial \xi_j} = v^j \Gamma^2_{12} \frac{\partial v^1}{\partial \xi_j} = v^1 \Gamma^2_{12} \frac{\partial v^1}{\partial \xi_1} + v^2 \Gamma^2_{12} \frac{\partial v^1}{\partial \xi_2} = \frac{v_r}{r}\frac{\partial v_r}{\partial r} + \frac{v_\theta}{r^2}\frac{\partial v_r}{\partial \theta},$$

Finally, term number (6) becomes,

$$v^j v^n \Gamma^l_{nj} \Gamma^s_{ls} = v^2 v^2 \Gamma^1_{22} \Gamma^2_{12} = -\left(\frac{v_\theta}{r}\right)^2.$$

Substituting these expressions into equation (B.3)

$$\nabla \cdot [\mathbf{v} \cdot \nabla \mathbf{v}] = \left(\frac{\partial v_r}{\partial r}\right)^2 + \frac{1}{r^2}\left(\frac{\partial v_\theta}{\partial \theta}\right)^2 + 2\frac{\partial v_r}{\partial \theta}\frac{\partial}{\partial r}\left(\frac{v_\theta}{r}\right) + 2v_\theta \frac{\partial}{\partial r}\left(\frac{v_\theta}{r}\right) + 2\frac{v_\theta}{r^2}\frac{\partial v_r}{\partial \theta} + 2\frac{v_\theta^2}{r^2}$$

$$- \frac{1}{r^2} v_r \frac{\partial v_\theta}{\partial \theta} - \frac{1}{r^2} v_\theta \frac{\partial v_r}{\partial \theta} + v_r \frac{\partial^2 v_r}{\partial r^2} + \frac{v_\theta}{r}\frac{\partial^2 v_r}{\partial r \partial \theta} + v_r \frac{\partial^2}{\partial \theta \partial r}\left(\frac{v_\theta}{r}\right) + \frac{v_\theta}{r^2}\frac{\partial^2 v_\theta}{\partial \theta^2} + \frac{v_r}{r^2}\frac{\partial v_\theta}{\partial \theta} + \frac{1}{r} v_r \frac{\partial v_r}{\partial r}.$$

(B·4)

The terms in the second line of this equation are similar to the continuity equation, and can be combined as follows:

$$\frac{1}{r^2}v_r\frac{\partial v_\theta}{\partial\theta}-\frac{1}{r^2}v_\theta\frac{\partial v_r}{\partial\theta}-v_r\frac{\partial^2 v_r}{\partial r^2}-\frac{v_\theta}{r}\frac{\partial^2 v_r}{\partial r\partial\theta}-v_r\frac{\partial^2}{\partial\theta\partial r}\left(\frac{v_\theta}{r}\right)-\frac{v_\theta}{r^2}\frac{\partial^2 v_\theta}{\partial\theta^2}-\frac{v_r}{r^2}\frac{\partial v_\theta}{\partial\theta}-\frac{1}{r}v_r\frac{\partial v_r}{\partial r}=$$

$$\frac{v_r}{r}\left(\frac{\partial v_r}{\partial r}-\frac{1}{r}\frac{\partial v_\theta}{\partial\theta}-\frac{v_r}{r}\right)-\frac{v_\theta}{r}\frac{\partial}{\partial\theta}\left(\frac{\partial v_r}{\partial r}-\frac{v_r}{r}-\frac{1}{r}\frac{\partial v_\theta}{\partial\theta}\right)-v_r\frac{\partial}{\partial r}\left(\frac{\partial v_r}{\partial r}-\frac{1}{r}\frac{\partial v_\theta}{\partial\theta}-\frac{v_r}{r}\right)-\frac{v_r}{r^2}\frac{\partial v_\theta}{\partial\theta}-v_r\frac{\partial}{\partial r}\left(\frac{v_r}{r}\right)-\left(\frac{v_r}{r}\right)^2$$

The three terms in parentheses are equal to zero from the continuity equation in two dimensions, leaving,

$$\frac{v_r}{r^2}\frac{\partial v_\theta}{\partial\theta}-\frac{v_r}{r}\frac{\partial v_r}{\partial r}-\left(\frac{v_r}{r}\right)^2-\left(\frac{v_r}{r}\right)^2=\frac{v_r}{r^2}\frac{\partial v_\theta}{\partial\theta}-\frac{v_r}{r}\frac{\partial v_r}{\partial r}$$

Substituting into equation (B.4),

$$\nabla\cdot\left[\mathbf{v}\cdot\nabla\mathbf{v}\right]=\left[\left(\frac{\partial v_r}{\partial r}\right)^2-\frac{1}{r^2}\left(\frac{\partial v_\theta}{\partial\theta}\right)^2-\frac{v_r}{r^2}\frac{\partial v_\theta}{\partial\theta}-\frac{v_r}{r}\frac{\partial v_r}{\partial r}\right]-2\frac{\partial v_r}{\partial\theta}\frac{\partial}{\partial r}\left(\frac{v_\theta}{r}\right)-2v_\theta\frac{\partial}{\partial r}\left(\frac{v_\theta}{r}\right)-2\frac{v_\theta}{r^2}\frac{\partial v_r}{\partial\theta}-2\frac{v_\theta^2}{r^2}$$

(B·5)

The terms in square brackets in equation (B.5) are quadratic and hence can be neglected from the perturbation assumptions. As a consequence, the resulting perturbation expression for the gradient of the steady-state particle acceleration expression is,

$$\nabla\cdot\left[\mathbf{v}\cdot\nabla\mathbf{v}\right]=2\frac{\partial v_r'}{\partial\theta}\frac{\partial}{\partial r}\left(\frac{V_\theta+v_\theta'}{r}\right)-2V_\theta v_\theta'-\frac{\partial}{\partial r}\left(\frac{V_\theta+v_\theta'}{r}\right)-2\frac{V_\theta+v_\theta'}{r^2}\frac{\partial v_r'}{\partial\theta}-2\frac{V_\theta+v_\theta'^2}{r^2}\qquad\text{(B.6)}$$

Excluding the steady-state solution and quadratic terms,

$$\nabla\cdot\left[\mathbf{v}\cdot\nabla\mathbf{v}\right]=2\frac{d}{dr}\left(\frac{V_\theta}{r}\right)\frac{\partial v_r'}{\partial\theta}-2V_\theta\frac{\partial}{\partial r}\left(\frac{v_\theta'}{r}\right)-2\frac{d}{dr}\left(\frac{V_\theta}{r}\right)v_\theta'-2\frac{V_\theta}{r^2}\frac{\partial v_r'}{\partial\theta}-\frac{4V_\theta}{r^2}v_\theta'\qquad\text{(B.7)}$$

Further simplifying, that equation can be written,

$$\nabla\cdot\left[\mathbf{v}\cdot\nabla\mathbf{v}\right]=\frac{2}{r}\frac{dV_\theta}{dr}\frac{\partial v_r'}{\partial\theta}-\frac{2V_\theta}{r}\frac{\partial v_\theta'}{\partial r}-\frac{2}{r}\frac{dV_\theta}{dr}v_\theta' \tag{B.8}$$

The divergence of the relaxation stress

Starting with the curvilinear formulation of the term,

$$\vec{\nabla}\cdot\left[\vec{\mathbf{y}}\cdot\vec{\nabla}\vec{\mathbf{y}}P\right]=\mathbf{g}^s\frac{\partial}{\partial\xi_s}\cdot\left\{\mathbf{g}^n\left[v^j\frac{\partial^2P}{\partial\xi_j\partial\xi_n}-v^j\Gamma^k_{jn}\left(\frac{\partial P}{\partial\xi_k}\right)\right]\right\}=$$

$$=\mathbf{g}^s\cdot\frac{\partial\mathbf{g}^n}{\partial\xi_s}\left[v^j\frac{\partial^2P}{\partial\xi_j\partial\xi_n}-v^j\Gamma^k_{jn}\left(\frac{\partial P}{\partial\xi_k}\right)\right]-g^{sn}\frac{\partial}{\partial\xi_s}\left[v^j\frac{\partial^2P}{\partial\xi_j\partial\xi_n}-v^j\Gamma^k_{jn}\left(\frac{\partial P}{\partial\xi_k}\right)\right]$$

Then,

$$\frac{\partial\mathbf{g}^n}{\partial\xi_s}=-\Gamma^n_{sr}\mathbf{g}^r,\ \text{and}\qquad \mathbf{g}^s\cdot\frac{\partial\mathbf{g}^n}{\partial\xi_s}=-\Gamma^n_{sr}\mathbf{g}^s\cdot\mathbf{g}^r=-g^{sr}\Gamma^n_{sr},\ \text{so that,}$$

$$\vec{\nabla}\cdot\left[\vec{\mathbf{y}}\cdot\vec{\nabla}\vec{\mathbf{y}}P\right]=-g^{sr}\Gamma^n_{sr}v^j\left[\frac{\partial^2P}{\partial\xi_j\partial\xi_n}-\Gamma^k_{jn}\left(\frac{\partial P}{\partial\xi_k}\right)\right]-g^{sn}\frac{\partial}{\partial\xi_s}\left[v^j\frac{\partial^2P}{\partial\xi_j\partial\xi_n}-v^j\Gamma^k_{jn}\left(\frac{\partial P}{\partial\xi_k}\right)\right] \tag{B.9}$$

In cylindrical coordinates the only non-zero terms in the contravariant metric tensor are;

$$g^{11}=1\ \text{and}\ g^{22}=\frac{1}{r^2},\ \text{so that}$$

$$\vec{\nabla}\cdot\left[\vec{\mathbf{y}}\cdot\vec{\nabla}\vec{\mathbf{y}}P\right]=-g^{ss}\Gamma^n_{ss}v^j\left[\frac{\partial^2P}{\partial\xi_j\partial\xi_n}-\Gamma^k_{jn}\left(\frac{\partial P}{\partial\xi_k}\right)\right]-g^{ss}\frac{\partial}{\partial\xi_s}\left[v^j\frac{\partial^2P}{\partial\xi_j\partial\xi_s}-v^j\Gamma^k_{js}\left(\frac{\partial P}{\partial\xi_k}\right)\right] \tag{B.10}$$

In cylindrical coordinates, then

$$\vec{\nabla}\cdot\left[\vec{\mathbf{y}}\cdot\vec{\nabla}\vec{\mathbf{y}}P\right]=$$

$$-g^{22}\Gamma^1_{22}v^j\left[\frac{\partial^2P}{\partial\xi_j\partial\xi_1}-\Gamma^k_{j1}\left(\frac{\partial P}{\partial\xi_k}\right)\right]-g^{11}\frac{\partial}{\partial\xi_1}\left[v^j\frac{\partial^2P}{\partial\xi_j\partial\xi_1}-v^j\Gamma^k_{j1}\left(\frac{\partial P}{\partial\xi_k}\right)\right]-g^{22}\frac{\partial}{\partial\xi_2}\left[v^j\frac{\partial^2P}{\partial\xi_j\partial\xi_2}-v^j\Gamma^k_{j2}\left(\frac{\partial P}{\partial\xi_k}\right)\right]$$

(B.11)

Expanding the curvilinear representation of equation (B.11) term-by-term

The first term can be represented

$$-g^{22}\Gamma^1_{22}\left[v^j\frac{\partial^2 P}{\partial\xi_j\partial\xi_1}-v^j\Gamma^k_{j1}\left(\frac{\partial P}{\partial\xi_k}\right)\right]=-g^{22}\Gamma^1_{22}\left[v^1\frac{\partial^2 P}{\partial\xi_1^{\,2}}-v^2\frac{\partial^2 P}{\partial\xi_2\partial\xi_1}-v^2\Gamma^2_{21}\left(\frac{\partial P}{\partial\xi_2}\right)\right]=\frac{1}{r}\left[v_r\frac{\partial^2 P}{\partial r^2}-\frac{v_\theta}{r}\frac{\partial^2 P}{\partial r\partial\theta}-\frac{v_\theta}{r^2}\left(\frac{\partial P}{\partial\theta}\right)\right]$$

The second term simplifies to,

$$g^{11}\frac{\partial}{\partial\xi_1}\left[v^j\frac{\partial^2 P}{\partial\xi_j\partial\xi_1}-v^j\Gamma^k_{j1}\left(\frac{\partial P}{\partial\xi_k}\right)\right]=g^{11}\frac{\partial}{\partial\xi_1}\left[v^1\frac{\partial^2 P}{\partial\xi_1^{\,2}}-v^2\frac{\partial^2 P}{\partial\xi_2\partial\xi_1}-v^2\Gamma^2_{21}\left(\frac{\partial P}{\partial\xi_2}\right)\right]$$

$$=\frac{\partial}{\partial r}\left\{v_r\frac{\partial^2 P}{\partial r^2}-\frac{v_\theta}{r}\frac{\partial^2 P}{\partial r\partial\theta}-\frac{v_\theta}{r^2}\left(\frac{\partial P}{\partial\theta}\right)\right\}$$

and the last term is,

$$g^{22}\frac{\partial}{\partial\xi_2}\left[v^j\frac{\partial^2 P}{\partial\xi_j\partial\xi_2}-v^j\Gamma^k_{j2}\left(\frac{\partial P}{\partial\xi_k}\right)\right]=g^{22}\frac{\partial}{\partial\xi_2}\left[v^1\frac{\partial^2 P}{\partial\xi_1\partial\xi_2}-v^2\frac{\partial^2 P}{\partial\xi_2^{\,2}}-v^1\Gamma^2_{12}\left(\frac{\partial P}{\partial\xi_2}\right)-v^2\Gamma^1_{22}\left(\frac{\partial P}{\partial\xi_1}\right)\right]$$

$$=\frac{1}{r^2}\frac{\partial}{\partial\theta}\left[v_r\frac{\partial^2 P}{\partial r\partial\theta}-\frac{v_\theta}{r}\frac{\partial^2 P}{\partial\theta^2}-\frac{v_r}{r}\left(\frac{\partial P}{\partial\theta}\right)-v_\theta\left(\frac{\partial P}{\partial r}\right)\right]$$

Combining the three terms,

$$\vec{\nabla}\cdot\left[\vec{\mathbf{v}}\cdot\vec{\nabla}\vec{\nabla}P\right]=\left(\frac{1}{r}-\frac{\partial}{\partial r}\right)\left[v_r\frac{\partial^2 P}{\partial r^2}-\frac{v_\theta}{r}\frac{\partial^2 P}{\partial r\partial\theta}-\frac{v_\theta}{r^2}\left(\frac{\partial P}{\partial\theta}\right)\right]-\frac{1}{r}\frac{\partial}{\partial\theta}\left[\frac{v_r}{r}\frac{\partial^2 P}{\partial r\partial\theta}-\frac{v_\theta}{r^2}\frac{\partial^2 P}{\partial\theta^2}-\frac{v_r}{r^2}\left(\frac{\partial P}{\partial\theta}\right)-\frac{v_\theta}{r}\left(\frac{\partial P}{\partial r}\right)\right]$$

Or

$$\vec{\nabla}\cdot\left[\vec{\mathbf{v}}\cdot\vec{\nabla}\vec{\nabla}P\right]=\frac{1}{r}\frac{\partial}{\partial r}\left\{r\left[v_r\frac{\partial^2 P}{\partial r^2}-\frac{v_\theta}{r}\frac{\partial^2 P}{\partial r\partial\theta}-\frac{v_\theta}{r^2}\left(\frac{\partial P}{\partial\theta}\right)\right]\right\}-\frac{1}{r}\frac{\partial}{\partial\theta}\left[\frac{v_r}{r}\frac{\partial^2 P}{\partial r\partial\theta}-\frac{v_\theta}{r^2}\frac{\partial^2 P}{\partial\theta^2}-\frac{v_r}{r^2}\left(\frac{\partial P}{\partial\theta}\right)-\frac{v_\theta}{r}\left(\frac{\partial P}{\partial r}\right)\right]$$

(B.12)

Hence, in the Poisson equation for non-equilibrium pressure (Equation. B.2) becomes,

$$-\nabla^2 P - Np\vec{\nabla}\cdot\left[\frac{D}{Dt}\vec{\nabla}P\right] = \left(-1 - Np\frac{\partial}{\partial t}\right)\nabla^2 P - \vec{\nabla}\cdot\left[\mathbf{v}\cdot\vec{\nabla}\vec{\nabla}P\right] =$$

$$\left(-1 - Np\frac{\partial}{\partial t}\right)\left[\frac{1}{r}\frac{\partial}{\partial r}\left(r\frac{\partial P}{\partial r}\right) - \frac{1}{r^2}\frac{\partial^2 P}{\partial\theta^2}\right] - \frac{Np}{r}\frac{\partial}{\partial r}\left\{r\left[v_r\frac{\partial^2 P}{\partial r^2} - \frac{v_\theta}{r}\frac{\partial^2 P}{\partial r\partial\theta} - \frac{v_\theta}{r^2}\left(\frac{\partial P}{\partial\theta}\right)\right]\right\}$$

$$- \frac{Np}{r}\frac{\partial}{\partial\theta}\left[\frac{v_r}{r}\frac{\partial^2 P}{\partial r\partial\theta} - \frac{v_\theta}{r^2}\frac{\partial^2 P}{\partial\theta^2} - \frac{v_r}{r^2}\left(\frac{\partial P}{\partial\theta}\right) - \frac{v_\theta}{r}\left(\frac{\partial P}{\partial r}\right)\right] \qquad \text{(B.13)}$$

Removing the steady-state solution and linearizing,

$$-\nabla^2 P - Np\vec{\nabla}\cdot\left[\frac{D}{Dt}\vec{\nabla}P\right] = Npv_r'\frac{d^3\bar{P}}{dr^3} - Np\left(\frac{v_r'}{r} - \frac{\partial v_r'}{\partial r}\right)\frac{d^2\bar{P}}{dr^2} - \left(-1 - Np\frac{\partial}{\partial t}\right)\left[\frac{1}{r}\frac{\partial}{\partial r}\left(r\frac{\partial p'}{\partial r}\right) - \frac{1}{r^2}\frac{\partial^2 p'}{\partial\theta^2}\right]$$

$$- \frac{Np}{r}\frac{\partial}{\partial r}\left\{r\left[\frac{V_\theta}{r}\frac{\partial^2 p'}{\partial r\partial\theta} - \frac{V_\theta}{r^2}\left(\frac{\partial p'}{\partial\theta}\right)\right]\right\} - \frac{Np}{r}\frac{\partial}{\partial\theta}\left[\frac{V_\theta}{r^2}\frac{\partial^2 p'}{\partial\theta^2} - \frac{V_\theta}{r}\left(\frac{\partial p'}{\partial r}\right) - \frac{v_\theta'}{r}\left(\frac{d\bar{P}}{dr}\right)\right]$$

Or

$$-\nabla^2 P - Np\vec{\nabla}\cdot\left[\frac{D}{Dt}\vec{\nabla}P\right] =$$

$$Np\frac{d^2\bar{P}}{dr^2}\frac{\partial v_r'}{\partial r} - Np\left(\frac{d^3\bar{P}}{dr^3} - \frac{1}{r}\frac{d^2\bar{P}}{dr^2}\right)v_r' - \left(-1 - Np\frac{\partial}{\partial t}\right)\left[\frac{1}{r}\frac{\partial}{\partial r}\left(r\frac{\partial p'}{\partial r}\right) - \frac{1}{r^2}\frac{\partial^2 p'}{\partial\theta^2}\right] -$$

$$Np\left(\frac{1}{r}\frac{dV_\theta}{dr} - \frac{V_\theta}{r^2}\right)\frac{\partial^2 p'}{\partial r\partial\theta} - Np\frac{V_\theta}{r}\frac{\partial^3 p'}{\partial r^2\partial\theta} - Np\frac{V_\theta}{r^3}\frac{\partial^3 p'}{\partial\theta^3} - Np\left(-\frac{1}{r^2}\frac{dV_\theta}{dr} - \frac{V_\theta}{r^3}\right)\frac{\partial p'}{\partial\theta} - \frac{Np}{r^2}\frac{d\bar{P}}{dr}\frac{\partial v_\theta'}{\partial\theta}$$

(B.14)

The complete pressure equation (B.2) becomes, after incorporating the relationships in equations (B.8) and (B.14),

$$\frac{2}{r}\frac{dV_\theta}{dr}\frac{\partial v_r'}{\partial\theta}+\frac{2V_\theta}{r}\frac{\partial v_\theta'}{\partial r}+\frac{2}{r}\frac{dV_\theta}{dr}v_\theta'=$$

$$Np\frac{d^2\bar{P}}{dr^2}\frac{\partial v_r'}{\partial r}+Np\left(\frac{d^3\bar{P}}{dr^3}+\frac{1}{r}\frac{d^2\bar{P}}{dr^2}\right)v_r'+\left(+1+Np\frac{\partial}{\partial t}\right)\left[\frac{1}{r}\frac{\partial}{\partial r}\left(r\frac{\partial p'}{\partial r}\right)+\frac{1}{r^2}\frac{\partial^2 p'}{\partial\theta^2}\right]+$$

$$Np\left(\frac{1}{r}\frac{dV_\theta}{dr}+\frac{V_\theta}{r^2}\right)\frac{\partial^2 p'}{\partial r\partial\theta}+Np\frac{V_\theta}{r}\frac{\partial^3 p'}{\partial r^2\partial\theta}+Np\frac{V_\theta}{r^3}\frac{\partial^3 p'}{\partial\theta^3}+Np\left(+\frac{1}{r^2}\frac{dV_\theta}{dr}+\frac{V_\theta}{r^3}\right)\frac{\partial p'}{\partial\theta}+Np\frac{d\bar{P}}{dr}\frac{\partial v_\theta'}{\partial\theta}$$

(B.15)

This is the *linearized pressure Poisson equation for pressure.*

Appendix C

MATLAB® CODES

```
% state variable model for 2D unsteady vortex flow with pressure
relaxation
clc;
clear;
small = 1e-6;
convergence=0.9;  % of max azimuthal velocity
%state variable parameters
Re=8000;
Np=2/Re;
n=0.5;
wR=0.4;
wI=1;dwI=0.1;
% variable definitions
r0=0.01; %initial radius
dr=1e-3; %radius step for RK4 solver
deltar=15.02; %radial domain size
rf = r0+deltar; % max radius
x=zeros(12,1);   %define state variable vector size
Y=ones(deltar/dr,13); %Output state variable
% Integration Loop
while (max(Y(:,7))>convergence || max(Y(:,3))>convergence)
    f=zeros(12,1);y=f;z=f;
    Y=zeros(deltar/dr,13); %re-initialize Output state variable
    x(1:2:7,1)=0;          %initial velocity perturbations gradient
    x(2:2:8,1)=1e-3;       %initial velocity perturbations amplitudes
    x(9:2:11,1)=0;         %initial perturbations pressure gradient
    x(10:2:12,1)=-1e-3;    %initial perturbations pressure amplitudes
    r = r0;
    j=1; %counter
    % Initialize output state variable vector
    Y(j,:)=[r x'];
    % Runge-Kutta integrator
    while ((r + small) < rf)
        f  = eqvxpr(x,r,wR,Re,n,wI,Np); y = x + f*dr/6; z = x + f*dr/2;
        r = r + dr/2;
        f  = eqvxpr(z,r,wR,Re,n,wI,Np); y = y + f*dr/3; z = x + f*dr/2;
        f  = eqvxpr(z,r,wR,Re,n,wI,Np); y = y + f*dr/3; z = x + f*dr;
        r = r + dr/2;
        f  = eqvxpr(z,r,wR,Re,n,wI,Np); x = y + f*dr/6;
        Y(j,:)=[r x']; %Stores The Outputs
        j=j+1;
    end
    wI=wI+dwI; % iterate at higher wI if solution doen't converge
end

%Max perturbations Amplitudes
[Y1 I1]=max(Y(:,3));[Y2 I2]=min(Y(:,3));
if Y1>abs(Y2),YY=Y1;II=I1; else YY=Y2;II=I2;end
disp('Max vr is:');disp(YY);disp('at r= ');disp(II*dr);
```

```
[Y1 I1]=max(Y(:,7));[Y2 I2]=min(Y(:,7));
if Y1>abs(Y2),YY=Y1;II=I1; else YY=Y2;II=I2;end
disp('Max v_theta is:');disp(YY);disp('at r= ');disp(II*dr);

[Y1 I1]=max(Y(:,10)); [Y2 I2]=min(Y(:,10));
if Y1>abs(Y2),YY=Y1;II=I1;else YY=Y2;II=I2;end
disp('Max dp/dr is:');disp(YY);disp('at r= ');disp(II*dr);

[Y1 I1]=max(Y(:,3).*Y(:,9)+Y(:,7).*Y(:,5));
[Y2 I2]=min(Y(:,3).*Y(:,9)+Y(:,7).*Y(:,5));
if Y1>abs(Y2),YY=Y1;II=I1;else YY=Y2;II=I2;end
disp('Max tau rtheta is:');disp(YY);disp('at r= ');disp(II*dr);

% Butworth filter
% radial velocity
[B,A]=butter(3,0.01);SVR=filter(B,A,abs(Y(:,3)));
figure (1);plot(Y(:,1),SVR,'k');hold on;
% azimuthal velocity
[B,A]=butter(3,0.01);SVR=filter(B,A,abs(Y(:,7)));
figure (2);plot(Y(:,1),SVR,'r');hold on;
% radial pressure gradient
[B,A]=butter(3,0.01);SVR=filter(B,A,abs(Y(:,10)));
figure (3);plot(Y(:,1),SVR,'b');hold on;
% Reynolds stresses
[B,A]=butter(3,0.01);SVR=filter(B,A,abs(Y(:,3).*Y(:,9)+Y(:,5).*Y(:,7)))
;
figure (4);plot(Y(:,1),SVR,'k');hold on;


function f = eqvxpr(x_v,r,wR,Re,n,wI,Np)
X=x_v;
% define equation coeficients
c1=2/(r*(r^2+1));
c2=4/(r^2+1)^2;
c3=4*(1-r^2)/(r*(r^2+1)^2);
c4=4*(1-3*r^2)/(r^2+1)^3;
c5=4*(9*r^4-14*r^2+1)/(r*(r^2+1)^4);
c6=(1+Np*wI)/((1+Np*wI)^2+Np^2*(wR+2*n/(r^2+1))^2);
c7=(Np*(wR+2*n/(r^2+1)))/((1+Np*wI)^2+Np^2*(wR+2*n/(r^2+1))^2);
c10=sqrt(c2);
c11=c1*sqrt(c2);
% Radial momentum equations
ddAr=-(1/r)*X(1)+((n^2+1)/r^2)*X(2)-Re*(wI+(2-n)*c10-Np*c4)*X(2)-...
    Re*wR*X(4)+(2*n/r^2)*X(6)-Re*Np*(wR+n*c10)*X(9)+...
    n*Np*Re*c1*X(10)+Re*(Np*wI+1)*X(11);
dAr=-X(2)/r-n*X(6)/r;
ddAi=-(1/r)*X(3)+((n^2+1)/r^2)*X(4)+Re*wR*X(2)-Re*(wI+(2-n)*c10-...
    Np*c4)*X(4)+(2*n/r^2)*X(8)-Re*(Np*wI+1)*X(9)-...
    Re*Np*(wR+n*c10)*X(11)+n*Np*Re*c1*X(12);
dAi=-X(4)/r-n*X(8)/r;
% Azimuthal Momentum equations
ddBr=-(1/r)*X(5)+((n^2+1)/r^2)*X(6)+Re*c2*X(2)-(2*n/r^2)*X(4)-...
    Re*(wI+Np*c11)*X(6)+Re*(wR+n*c10)*X(8)...
    -Re*Np*c10*X(9)+Re*Np*(n/r)*(wR+n*c10)*X(10)...
    -Re*(n/r)*(Np*wI+1)*X(12);
```

```
dBr=X(5);

ddBi=-(1/r)*X(7)+((n^2+1)/r^2)*X(8)+(2*n/r^2)*X(2)+Re*c2*X(4)+...
    Re*(wR+n*c10)*X(6)-Re*(wI+Np*c11)*X(8)...
    +Re*(n/r)*(Np*wI+1)*X(10)-Re*Np*c10*X(11)...
    +Re*Np*(n/r)*(wR+n*c10)*X(12);
dBi=X(7);
%Pressure equations
ddDr=-(1/r)*X(9)+((n^2+1)/r^2)*X(10)-Np*c7*c4*X(1)-...
    (n*c6*c3+Np*c7*c5)*X(2)-Np*c6*c4*X(3)-(Np*c6*c5+n*c7*c3)*X(4)...
    -2*c6*c10*X(5)+(-c6*(c1+2*c10)-n*Np*c7*c11)*X(6)-2*c7*c10*X(7)...
    +(-n*Np*c6*c11-c7*(c1+2*c10))*X(8)-0.5*n*Np*c7*c3*X(9)...
    -n*Np*c7*c2*X(10)-0.5*c3*Np*n*c6*X(11)-n*Np*c6*c2*X(12);
dDr=X(9);
ddDi=-(1/r)*X(11)+((n^2+1)/r^2)*X(12)+Np*c6*c4*X(1)-(n*c7*c3-...
    Np*c6*c5)*X(2)-Np*c7*c4*X(3)-(Np*c7*c5-n*c6*c3)*X(4)...
    -2*c7*c10*X(5)+(-c7*(c1+2*c10)+n*Np*c6*c11)*X(6)+2*c6*c10*X(7)...
    +(-n*Np*c7*c11+c6*(c1+2*c10))*X(8)+0.5*n*Np*c6*c3*X(9)...
    +n*Np*c6*c2*X(10)-0.5*c3*Np*n*c7*X(11)-n*Np*c7*c2*X(12);
dDi=X(11);

f = [ddAr dAr ddAi dAi ddBr dBr ddBi dBi ddDr dDr ddDi dDi].';
end
```

VITA

MAZIN MOHAMMED ELBAKRI ABUHARAZ

Old Dominion University

Norfolk, Virginia, 23529

EDUCATIONAL BACKGROUND

PhD. in Mechanical and Aerospace Engineering
February 2014

Old Dominion University, Norfolk, Virginia, USA;

M.S. in Electrical Power Engineering Jan 2009

University of Khartoum, Khartoum, Sudan;

B.S. in Mechanical Engineering May 2001

University of Khartoum, Khartoum, Sudan;

SELECTED PUBLICATIONS

Abuharaz, M. and R.L. Ash, "A new approach for modeling the unsteady behavior of trailing line axial vortices", presented at the 43rd AIAA Fluid Dynamics Conference and Exhibit, San Diego, CA, 24-27 June , 2013. AIAA Paper No. 2013-3188.

El-Awad, M.M. and Abuharaz M., "A Case for Introducing Thermal-Design Optimization using Excel Spreadsheet", accepted at 10th International Conference on Heat Transfer, Fluid Mechanics and Thermodynamics (HEFAT2014), Orlando, Florida, 14 - 16 July, 2014.